AIX-MARSEILLE UNIVERSITÉ

Ecole Doctorale Physique et Sciences de la Matière

CPPM

Centre de Physique des Particules des Marseille

Thèse présentée pour obtenir le grade universitaire de docteur

Physique des Particules et Astroparticules

Ilenia SALVADORI

Etude des oscillations de neutrinos atmosphériques avec le télescope à neutrinos ANTARES

Study of atmospheric neutrino oscillations with the ANTARES neutrino telescope

Soutenue le 10/10/2018 devant le jury composé de:

Caren HAGNER	Hamburg University	Rapporteur
Sergio NAVAS-CONCHA	University of Granada	Rapporteur
Cristinel DIACONU	CPPM	Examinateur
Thierry LASSERRE	CEA/IRFU Saclay	Examinateur
Veronique VAN-ELEWCYCK	Paris Diderot University	Examinateur
José BUSTO	CPPM	Examinateur
Jürgen BRUNNER	CPPM	Directeur de thèse

Numéro national de thèse/suffixe local: 2018AIXM0283/026ED352

Résumé en français

Les neutrinos sont probablement les particules les plus particulières connues à ce jours. De la première hypothèse sur leur existence, en 1930, jusqu'à aujourd'hui, ils ont incité les scientifiques à élaborer des techniques expérimentales novatrices et à développer des modèles théoriques pour expliquer et étudier leurs propriétés.

Les neutrinos sont produits dans une grande variété de processus, à la fois naturels et artificiels, couvrant une vaste gamme d'énergies et nécessitant donc un nombre impressionnant de dispositifs expérimentaux différents pour être étudiés. En raison de leur section efficace extrêmement faible, des installations expérimentales énormes sont nécessaires pour détecter les interactions des neutrinos. En revanche, la nature faiblement interactive de ces particules, qui permettent aux neutrinos de parcourir de grandes distances sans être déviés par quoi que ce soit, offre un énorme potentiel pour l'étude des sources galactiques et extra-galactiques dans lesquelles les neutrinos sont produits. Cette propriété est à la base de l'astronomie des neutrinos et, la combinaison de la détection des neutrinos de ces sources à celle des autres particules - rayons γ et X, ondes radio et gravitationnelles - a ouvert l'ère de l'astronomie multi-messager.

Les neutrinos sont également intéressants pour leurs propriétés intrinsèques. Aujourd'hui nous connaissons trois différents types de neutrinos, appelés *saveurs*: le neutrino électronique (ν_e), le neutrino muonique (ν_μ) et le neutrino tau (ν_τ). Il est bien établi que les neutrinos sont affectés par le phénomène des *oscillations*, ce qui signifie que les états propres quantiques dans lesquels un neutrino peut être détecté, les *états propres de saveur*, ne sont pas les mêmes que les états propres lors de la propagation des neutrinos, les *états propres de masse.* Les états propres de saveur et de masse sont liés par une matrice non diagonale, ce qui implique qu'un neutrino peut être détecté dans une saveur différente de celle qu'il avait au point de production. La mesure précise des paramètres qui régulent le mélange entre états de saveur et de masse a représenté l'un des principaux objectifs pour les physiciens des neutrinos depuis la découverte des oscillations des neutrinos.

Le phénomène des oscillations de neutrinos prouve directement que les neutrinos sont des particules massives, par rapport à ce qui avait été initialement supposé dans le Modèle Standard de la Physique des Particules. Même si les expériences d'oscillation des neutrinos ne sont pas sensibles à la valeur absolue des masses de neutrinos, la différence entre le carré des états propres de masse peut être déterminée.

La physique des neutrinos est l'un des sujets les plus actifs en physique des particules aujourd'hui, et beaucoup d'informations manquent encore pour compléter notre compréhension de ces particules. Jusqu'à présent, en fait, une seule des deux différences de masse indépendantes a été déterminé avec sa valeur et avec son signe, laissant deux ordonnancements possibles pour les états propres de masse de neutrinos. Cette ambiguité est connue sous le nom de *problème de hiérarchie des masses.* Une première indication de l'ordonnancement de masse préférée experimentalement a été récemment donnée, et plusieurs nouvelles experiences sont en construction afin de trouver une réponse définitive.

Une autre ambiguïté qui n'a pas encore été fixée concerne la nature intrinsèque des neutrinos. Deux scénarios sont en effet possibles: celui qui décrit les neutrinos comme la même particule que l'anti-neutrino (neutrinos de Majorana), et celui qui distingue les deux (neutrinos de Dirac). La désintégration double β sans neutrinos est un processus qui ne serait possible que si les neutrinos étaient des particules de Majorana. Jusqu'à présent, ce processus n'a jamais été observé, mais de nombreuses installations expérimentales ont été mises en place pour étudier la possibilité d'un tel phénomène et déterminer la nature des neutrinos.

De plus, plusieurs anomalies expérimentales observées semblent indiquer une image plus complexe en ce qui concerne le scénario standard à trois saveurs de neutrinos. Des modèles théoriques dans lesquels un ou plusieurs types supplémentaires de neutrinos, appelés *stériles*, existent, ont été étudiés. Ces neutrinos supplémentaires ne participeraient pas aux interactions avec la matiere ordinaire comme les neutrinos actifs, mais leur présence modifierait en tout cas les probabilités d'oscillation standard des autres saveurs, introduisant des distorsions qui peuvent être décrites par des paramètres de mélange supplémentaires. Plusieurs expériences tentent actuellement de contraindre l'espace des paramètres de ces nouveaux modèles, et de faire la lumière sur ce problème.

ANTARES est un télescope à neutrinos situé au fond de la Mer Méditerranée, à 40 km au large de Toulon (France). Il est composé de 12 lignes de détection, chacune équipée de 25 modules optiques (OMs) répartis en groupes de 3 (étages), à l'exception de la ligne 12 qui ne compte que 20 OMs. La technique de détection d'ANTARES repose sur le rayonnement Cherenkov émis par les particules chargées ultra-relativistes produits par les interactions des neutrinos. ANTARES a été achevé en 2008 et il a été optimisé pour la détection de neutrinos de très haute énergie, provenant de sources galactiques et extra-galactiques. Le seuil en énergie d'ANTARES, d'environ 20 GeV, permet également d'étudier le phénomène des oscillations de neutrinos, à travers la détection des neutrinos atmosphériques qui ont traversé la Terre avant d'interagir à proximité du volume du détecteur. En effet, pour un neutrino muonique atmosphérique verticalement ascendant, le premier minimum d'oscillation est atteint à une énergie d'environ 25 GeV, ce qui est encore détectable par ANTARES.

L'objectif principal de ce travail de thèse est de fournir une nouvelle mesure des paramètres d'oscillation des neutrinos atmosphériques, en utilisant dix années de données collectées par le télescope à neutrinos ANTARES. Une analyse antérieure avec les données ANTARES recueillies de 2007 à 2010 avait déjà été publiée. L'objectif de cette thèse est d'améliorer les résultats d'une telle analyse, en utilisant un échantillon de données beaucoup plus important ainsi qu'une nouvelle chaîne d'analyse. A cette fin, deux algorithmes de reconstruction d'événement ont été combinés afin d'améliorer les statistiques et differents critères de sélection d'événements spécifiques ont été testé contre la contamination du bruit de fond.

Alors que la première analyse des oscillations d'ANTARES ne tenait compte que d'un effet de normalisation systématique global, différentes sources de systématiques ont été étudiées et prises en compte dans cette nouvelle analyse. Diverses incertitudes liées aux flux ont été mises en œuvre, ainsi que des incertitudes liées aux sections efficaces. L'effet de la systématique liée au détecteur, telle qu'une variation de la valeur nominale de l'efficacite de détection de photons des OMs, a été étudié. De plus, le bruit de fond dû aux muons atmosphériques a été évalué au moyen d'une technique basée sur les données, tandis que les distributions d'énergie et les distributions angulaires ont été calculées à partir de simulations Monte Carlo (MC).

Afin de trouver l'ensemble des paramètres d'oscillation des neutrinos atmosphériques qui décrivent le mieux les données, une approche de *log-likelihood* a été suivie, réalisant une minimisation 2D sur les distributions d'énergie et angulaires.

L'analyse entière a d'abord été testée avec une étude de sensibilité basée sur MC, à savoir la construction d'un échantillon de pseudo-données en utilisant les événements MC. De cette manière, les différents ensembles de critères de sélection des événements ont été testés et celui qui a donné le meilleur résultat en termes de rejet de muons et de sensibilité aux paramètres d'oscillation a été choisi pour l'analyse finale.

Les résultats de cette analyse ont été comparés à ceux obtenus lors de l'analyse d'oscillations ANTARES précédente et à ceux publiés par d'autres collaborations. Une bonne amélioration par rapport au précédent résultat d'ANTARES est constatée, bien que la nouvelle analyse prenne en compte des incertitudes beaucoup plus systématiques. Sans surprise, les résultats d'ANTARES ne sont pas compétitifs par rapport à ceux fournis par des installations expérimentales plus adaptées à ce type de recherche. Cependant, ils sont toujours compatibles avec les expériences majeures dans ce domaine.

Une autre partie très importante de ce travail de thèse a été consacrée aux études sur les neutrinos stériles. En effet, pour les énergies de neutrinos comprises entre 20 et 100 GeV, la présence d'un neutrino stérile modifierait les probabilités d'oscillation des saveurs actives.

La gamme d'énergie intéressée par cette étude est la même que pour l'analyse des oscillations standard. Pour cette raison, le même ensemble de données et la même chaîne d'analyse ont été appliqués.

Le traitement des différentes sources systématiques a été le même que celui utilisé pour l'analyse des oscillations standard. Une étude spécifique supplémentaire a été réalisée afin d'étudier l'impact des paramètres standards d'oscillation des neutrinos atmosphériques en tant que systématique.

Même dans ce cas, l'analyse complète a été anticipée par une étude de sensibilité du MC visant à étudier le potentiel d'une telle recherche avec ANTARES.

Les résultats représentent la première analyse d'étude de neutrinos stériles d'ANTARES; ils sont cohérents avec les résultats publiés par d'autres collaborations et, dans certaines régions de l'espace paramétrique, ils permettent de fixer des limites encore plus strictes.

Une étude supplémentaire a été réalisée pour évaluer le potentiel d'ANTARES à contraindre l'espace des paramètres des neutrinos stériles en utilisant des événements plus énergétiques. En effet, pour les énergies des neutrinos de l'ordre de TeV, le nouveau parametre de masse introduit par l'addition d'un neutrino stérile est responsable d'une résonance induite par la matière qui entraîne un nouveau minimum des probabilités d'oscillation de survie des neutrinos muoniques. Si la masse du neutrino stérile était plus légère que celle des saveurs actives, cette résonance se produirait dans le secteur des neutrinos, sinon dans le secteur des anti-neutrinos.

Pour cette analyse, une étude de sensibilité MC a été réalisée. Comme les résultats indiquaient déjà qu'aucune contrainte supplémentaire ne pouvait être ajoutée par ANTARES par rapport à celles déjà fournies par d'autres collaborations, il a été décidé de ne pas poursuivre l'analyse.

Une analyse indépendante a été développée dans le cadre de ce travail de thèse, visant à étudier les efficacités de détection des photons des OMs d'ANTARES. Cela a été fait en exploitant les désintégrations ^{40}K présents dans l'eau de mer. Les produits de désintégration d'éléments radioactifs, tels que le ^{40}K, dissous dans l'eau de mer constituent la principale source de lumière de fond pour les télescopes à neutrinos profonds. Ce processus constitue également une technique de calibration importante. Si un noyau ^{40}K se désintègre près d'un étage, la lumière Cherenkov qui en résulte peut être enregistrée par deux OMs presque simultanément. De telles coïncidences sont utilisées pour calculer les efficacités relatives de détection des photons et pour l'étalonnage en temps entre les OM dans l'étage.

En utilisant les données collectées par le télescope à neutrinos ANTARES avec un algorithme de déclenchement ^{40}K dédié, les efficacités de détection des photons pour tous les OMs ont été calculés pour les données enregistrées entre mi-2008 et fin 2017. L'étude révèle la stabilité d'un détecteur basé sur des photomultiplicateurs (PMTs) dans l'environnement hostile des profondeurs marines, pour la plus longue période jamais enregistrée. Cela démontre que les expériences sous-marines futures peuvent rester opérationnelles pendant au moins une décennie sans dégradation majeure de l'efficacité. Une diminution moyenne de l'efficacité de l'OM de 20%, observée de 2008 à 2017, implique une perte de seulement 15% de l'efficacité de détection d'un signal astrophysique avec un spectre E^{-2}. L'effet du vieillissement du PMT est certainement présent. L'encrassement biologique pourrait également être en partie responsable de la perte d'efficacité. La meilleure façon de tester le développement de l'encrassement biologique est la récupération des OMs, prévue à la fin de l'opération physique d'ANTARES, vers 2020. Cette étude a été récemment publiée par le *European Physical Journal C* et ses résultats servent de base à la production MC la plus récente d'ANTARES.

Afin de mettre à jour la chaîne de production MC d'ANTARES, des efforts ont été déployés au cours de cette thèse pour tester différents modèles des propriétés optiques de l'eau et identifier celui qui décrit le mieux les propriétés de l'eau sur le site ANTARES.

Toutes les études présentées dans ce travail de thèse pourraient servir de point de départ à la prochaine génération de télescopes à neutrinos en mer Méditerranée, appelée KM3NeT. KM3NeT comprendra deux détecteurs principaux, ARCA en Sicile, consacré à la physique des astroparticules à haute énergie, et ORCA en France, axé sur les études des neutrinos atmosphériques ayant une énergie de quelques GeV. Ils utilisent tous deux une configuration similaire à celle d'ANTARES, mais avec 31 PMT au lieu de trois sur chaque étage.

ORCA sera notamment constitué, dans sa configuration finale, de 115 lignes de détection équipées de 18 étages de 31 PMT chacune. Il sera beaucoup plus dense par rapport à ANTARES, ce qui permettra de réduire le seuil en énergie à quelques GeV. Ce faible seuil en énergie fait d'ORCA un détecteur très adapté à l'étude des oscillations atmosphériques des neutrinos.

De plus, la technique employée ici pour la détermination de l'efficacité de détection des photons des OMs d'ANTARES en utilisant les désintégrations ^{40}K dans l'eau de mer est également utilisée pour KM3NeT.

Le document est organisé comme suit. Au chapitre 1, après une introduction sur les grandes étapes scientifiques qui ont amené, d'abord à émettre des hypothèses puis à prouver l'existence des neutrinos, les différentes sources de neutrinos sont introduites, ordonnées en fonction de l'énergie des neutrinos correspondante. Les différents types d'interactions des neutrinos avec la matière sont décrits, avec un accent particulier sur la gamme d'énergie intéressée par la présente analyse.

A ce stade, le phénomène des oscillations de neutrinos est revu. Après une première brève présentation historique, la théorie des oscillations des neutrinos, aussi bien dans le vide que dans la matière, est rappelée. Les différents types de dispositifs expérimentaux pouvant être sensibles aux oscillations des neutrinos sont décrits, ainsi que l'état actuel de ces expériences et notre compréhension des paramètres d'oscillation des neutrinos.

La théorie du modèle neutrino 3+1, qui prévoit l'existence d'un neutrino stérile, en plus des trois neutrinos actifs, est décrite. Les paramètres supplémentaires à prendre en compte lors de la manipulation du modèle étendu sont introduits. Les principaux canaux d'oscillation étudiés pour analyser tout l'espace des paramètres du modèle neutrino 3+1 sont décrits, ainsi que les anomalies expérimentales observées et pouvant être en principe expliquées dans le modèle étendu.

Une dernière section est réservée aux questions encore ouvertes en physique des neutrinos, qui n'ont pas fait partie de l'analyse présentée ultérieurement dans la thèse, mais qui méritent d'être mentionnées afin de souligner une fois de plus ce que ce domaine a à offrir. Le problème de la hiérarchie des neutrinos est introduit, ainsi que les principaux dispositifs expérimentaux actuellement en construction pour le résoudre. La détermination de la phase de violation de CP, le seul paramètre de mélange des neutrinos standards encore inconnu, est discutée et les techniques expérimentales exploitées pour la mesurer sont présentées. La nature Dirac / Majorana des neutrinos, ainsi que la mesure des masses absolues des neutrinos sont également introduites, ainsi que les moyens mis au point pour éclairer ces sujets.

Au Chapitre 2, le télescope à neutrinos ANTARES est introduit, son mécanisme de détection décrit et le système d'acquisition de données expliqué. Les différents objectifs physiques poursuivis par ANTARES sont décrits.

Le Chapitre 3 a été consacré à la détermination de l'efficacité des modules optiques ANTARES, à travers les désintégrations de ^{40}K dans l'eau de mer. Après avoir décrit les principales étapes qui permettent de calculer le taux de ^{40}K sur le site ANTARES, la procédure d'analyse pour le calcul des efficacités de détection des photons des OMs est décrit. L'échantillon de données employé et les résultats obtenus sont discutés. L'utilisation de désintégrations ^{40}K dans le cadre de l'étalonnage en temps complet du détecteur est également décrite.

Le Chapitre 4 décrit toute la procédure de simulation d'événements développée dans la collaboration ANTARES, à partir de la génération de l'événement, jusqu'à sa propagation à travers le volume du détecteur et à sa détection finale. Des efforts qui ont été faits pour tester différents modèles des propriétés optiques de l'eau sur le site d'ANTARES, afin d'utiliser des modèles les plus précis possibles pour la nouvelle production de Monte Carlo, qui a été développée dans la dernière année. Ces tests sont également présentés et discutés.

Les différentes procédures de reconstruction d'événements utilisées dans toutes les analyses présentées sont présentées au Chapitre 5, ainsi que les méthodes employées pour l'estimation de l'énergie des neutrinos. Les différents critères de sélection des événements testés, afin de garantir un échantillon final aussi pur que possible sont enfin discutés. Les différents critères de sélection d'événement sont comparés en termes de nombre attendu d'événements de signal par rapport au nombre prévu d'événements de fond, ainsi qu'en termes de résolution en énergie.

L'analyse principale, consacrée à la détermination des paramètres d'oscillation des neutrinos atmosphériques, est présentée au Chapitre 6. La procédure de minimisation suivie est décrite. Les différentes sources de systématiques prises en compte dans l'analyse sont présentées et leur traitement est discuté. Les résultats de l'étude de sensibilité MC pour tous les critères de sélection des événements testés sont présentés et discutés. L'analyse proprement dite a donc été effectuée à l'aide de l'ensemble des critères de sélection des événements qui se sont avérés plus performants. L'échantillon de données après une telle sélection est introduit et les résultats de l'analyse sont discutés.

Dans le Chapitre 7, le même ensemble de données est utilisé pour contraindre le modèle neutrino 3+1, qui prédit l'existence d'un neutrino stérile supplémentaire. Suivant le schéma du chapitre précédent, le traitement des erreurs systématiques est discuté, suivi des résultats de l'étude de sensibilité du MC. Les résultats finaux sont ensuite présentés et comparés à ceux d'autres collaborations. La dernière partie de ce chapitre est consacrée à une autre analyse, dont l'objectif est de fournir des limites supplémentaires sur le modèle neutrino 3+1 en examinant les événements à énergie plus élevée. Pour cette étude, seule une étude préliminaire de sensibilité a été réalisée et le potentiel de l'analyse est discuté et comparé à ceux d'autres collaborations.

Des conclusions sont ensuite données, y compris un résumé des résultats obtenus et quelques perspectives d'avenir pour KM3NeT, le télescope à neutrinos de deuxième génération en Mer Méditerranée.

Abstract

Neutrinos are probably the most peculiar particles known. From the first assumption about their existence, back in 1930, till today, they have challenged scientists in building innovative experimental techniques as well as in developing theoretical models in order to explain and study their properties.

The ANTARES neutrino telescope has been optimized to study high energy neutrinos coming from galactic and extra-galactic astrophysical objects. On the other hand, at neutrino energies of the order of a few tens of GeV, the detector configuration and the reconstruction algorithms allow to study the phenomenon of atmospheric muon neutrino disappearance due to neutrino oscillations, by looking at distortions in the energy and angular distributions of detected events. In a similar way, constraints on the 3+1 neutrino model, which foresees the existence of a sterile neutrino, can be inferred. Using data collected by the ANTARES neutrino telescope from 2007 to 2016, a new measurement of Δm^2_{32} and θ_{23} has been performed, and constraints on the 3+1 model have been derived.

Cherenkov light induced by radioactive decay products is one of the major sources of background light for deep-sea neutrino telescopes such as ANTARES. These decays are at the same time a powerful calibration source. Using data collected by the ANTARES neutrino telescope from mid 2008 to 2017, the time evolution of the photon detection efficiency of optical modules has been studied as well.

Résumé

Les neutrinos sont probablement les particules les plus particulières connues à ce jours. Dès la première hypothèse sur leur existence, en 1930, jusqu'à aujourd'hui, ils ont incité les scientifiques à élaborer des techniques expérimentales novatrices et à développer des modèles théoriques pour expliquer et étudier leurs propriétés.

Le télescope à neutrinos ANTARES a été optimisé pour étudier les neutrinos de haute énergie provenant d'objets astrophysiques galactiques et extra-galactiques. Par contre, aux énergies des neutrinos de l'ordre de quelques dizaines de GeV, la configuration du détecteur et les algorithmes de reconstruction permettent d'étudier le phénomène de disparition des neutrinos atmosphériques muoniques dû aux oscillations des neutrinos, en observant les distorsions de la distribution énergétique et angulaire des événements détectés. De manière similaire, des contraintes sur le modèle neutrino 3+1, qui prévoit l'existence d'un neutrino stérile, peuvent être inférées. En utilisant les données collectées par le télescope à neutrinos ANTARES entre 2007 et 2016, une nouvelle mesure de Δm^2_{32} et θ_{23} a été effectuée et des contraintes sur le modèle 3+1 ont été dérivées.

La lumière Cherenkov induite par les produits de désintégrations d'éléments radioactifs est l'une des principales sources de lumière de fond pour les télescopes à neutrinos profonds tels que ANTARES. Ces désintégrations sont en même temps une source d'étalonnage puissante. À partir des données collectées par le télescope à neutrinos ANTARES entre mi-2008 et 2017, l'évolution temporelle de l'efficacité de détection des photons des modules optiques a également été étudiée.

Contents

Chapter 1

Neutrinos: an amazing journey in Particle Physics

In this first Chapter, after a brief historical overview of the main steps which have brought to our current understanding of Neutrino Physics, the different sources of neutrinos are described. Neutrino interactions are then illustrated, with particular attention to the energy range relevant for this thesis. The theory of neutrino oscillations, both in vacuum and matter, is revised, together with the experimental status on the determination of the neutrino mixing parameters. The extended *sterile* neutrino model is then presented. A final section is dedicated to the remaining missing pieces on the study of neutrino properties.

1.1 Brief history of neutrinos

Neutrinos are probably the most peculiar particles known. They are electrically neutral fermions of spin $\frac{1}{2}$. Their existence was first hypothesized by W. Pauli in 1930 [1], in order to explain the continuous energy spectrum of electrons in β-decay and to fix the problem of the observed spin of some nuclei, like $^{14}_{7}\mathrm{N}$. Four years later, E. Fermi formulated the theory of weak interactions, based on Pauli's assumption, and he proposed to call this new particle "neutrino", which in Italian means "little neutral".

The problem was then how to detect the neutrino. The first idea came from B. Pontecorvo, who suggested to use radiochemical reactions in order to detect inverse

β-decays induced by neutrinos. F. Reines and C.L. Cowan, in 1956, were able to prove the existence of neutrinos [2]. They exploited the reaction:

$$\overline{\nu} + p \to e^+ + n$$

which has a kinematic threshold of 1.806 MeV, and used water as target material and a liquid scintillator and $CdCl_2$ as detectors. The positron can annihilate with an electron, resulting in two photons with opposite momenta; on the other hand, the neutron is captured by the Cd, producing another photon within 5 μs. By recording both the photons from the positron annihilation and the one from the delayed neutron capture, they were able to suppress the background and obtained the definite proof of the neutrino induced reaction. Reines was awarded of the Nobel Prize in 1995 for this experiment.

In 1962, a second type of neutrino, the muon neutrino (ν_μ), was discovered [3]. This experiment, which was the first one using high energy neutrinos produced in accelerators, proved the existence of a second lepton family, (μ, ν_μ), in addition to the first one, (e, ν_e), and it was worth the Nobel Prize in Physics, in 1988, to L.M. Lederman, M. Schwartz and J. Steinberger. The Brookhaven experiment consisted in a beam of π^+, obtained by shooting protons towards a Be target, which decay through a 21 m long decay channel. The dominant decay channel of the π^+ is:

$$\pi^+ \to \mu^+ + \nu_\mu \tag{1.1}$$

while the channel:

$$\pi^+ \to e^+ + \nu_e \tag{1.2}$$

is strongly suppressed due to spin arithmetic. If ν_e and ν_μ were identical, neutrinos from the dominant decay channel would produce muons and electrons in the same way, through the reaction:

$$\nu_{e,\mu} + N \to (e^-, \mu^-) + X \tag{1.3}$$

and one would expect to detect the same amount of muons and electrons. 29 muon and 6 electron events were detected, these last being compatible with the background hypothesis, proving in this way that ν_μ and ν_e are different particles. The result of the Brookhaven experiment also suggested that the total electron and muon lepton numbers, L_e e and L_μ, are conserved. Today we know that this is true only neglecting neutrino masses, and that the conservation law is violated in neutrino oscillations. This phenomenon will be discussed further in this Chapter (see Section 1.4).

In a series of experiments performed at the $e^+ - e^-$ collider at Stanford by M. Perl et al. in 1975-77 [4], a third lepton, $\tau^\pm$, was discovered. This result opened the question on the possible existence of a third family of leptons, namely a third type of neutrino. This particle was indeed observed in 2000 in an experiment performed by the DONUT Collaboration at Fermilab [5].

But how many families of leptons do exist then? This question was answered by experiments performed both at CERN and at Stanford, where the decay width of the Z^0 boson was studied. The *invisible* width in neutrinos, $\Gamma(Z^0 \to \nu\overline{\nu})$, is measured inderectly by studying the hadron production cross section around the Z resonance. The four LEP experiments at CERN scanned it around the Z^0 mass, in the energy range 88-94 GeV, and measured the corresponding cross section. The combined LEP results gave the result of [6]:

$$n_{\nu_f} = 2.984 \pm 0.008 \tag{1.4}$$

establishing that the number of different types of neutrinos was equal to three. It is worth noting that from these results one can not exclude, however, that there exist more massive neutral leptons which can not be produced in decays of the Z^0 boson (see Section 1.5).

1.2 Neutrino sources

Neutrinos are produced in a variety of processes, which spread over a huge energy range. For this reason, different kinds of detection techniques are required, and a single experiment cannot be sensitive to all neutrino sources at once. In this Section the main neutrino sources are explained, and their typical energy range is described.

1.2.1 Cosmic neutrino background

According to the Standard Big Bang cosmology, neutrinos decoupled from other particles and stopped interacting at the decoupling temperature, $T_{\nu,dec}$, of 2-3 MeV for ν_e and of 3.5 MeV for ν_μ and ν_τ [7]. The decoupling temperature is related to the time after the Big Bang, t, by:

$$t \sim (\frac{1MeV}{T_{\nu,dec}})^2 s \tag{1.5}$$

From Equation 1.5 one gets that neutrinos decoupled from the other particles only ~ 0.3 s after the Big Bang.

Due to the very low neutrino cross section (see next section for details), neutrinos coming from the cosmic background still exist and could bring important information of the very early phases of the Universe. However, their energy is extremely low ($10^{-4} - 10^{-6}$ eV), and thus they are very difficult to detect.

Three different techniques have been proposed in order to detect the cosmic neutrino background (CNB). Direct searches look for momentum transfer in coherent CNB elastic scattering with target nuclei or for neutrino capture by β-decaying nuclei. Indirect methods, instead, are the ones which study possible spectral distortions due to CNB interactions with ultra-high energy neutrinos, protons or other nuclei from various sources.

1.2.2 Solar neutrinos

Electron neutrinos are copiously produced in our Sun, by means of the nuclear reactions which take place in its core. In Figure 1.1, the produced solar neutrino flux as a function of the neutrino energy, for all the different reactions in the Sun, is shown.

The so called *pp* chain, in which two Hydrogen nuclei fuse together to form a Deuterium, produces 98% of the energy of the Sun. Therefore *pp*-neutrinos are the most abundantly produced neutrinos by our Star. Their energy, however, is quite low, with a continuous spectrum that ends at 420 keV, and for this reason they are very difficult to detect. In addition to the *pp* chain, there are several rarer reactions which also produce neutrinos. Among them, the β-decay of Boron-8 produces neutrinos with energies up to 15 MeV.

Solar neutrinos represent an important tool to test the solar model, and measuring the neutrino flux from the Sun has been one of the first steps toward the discovery of neutrino oscillations (see Section 1.4).

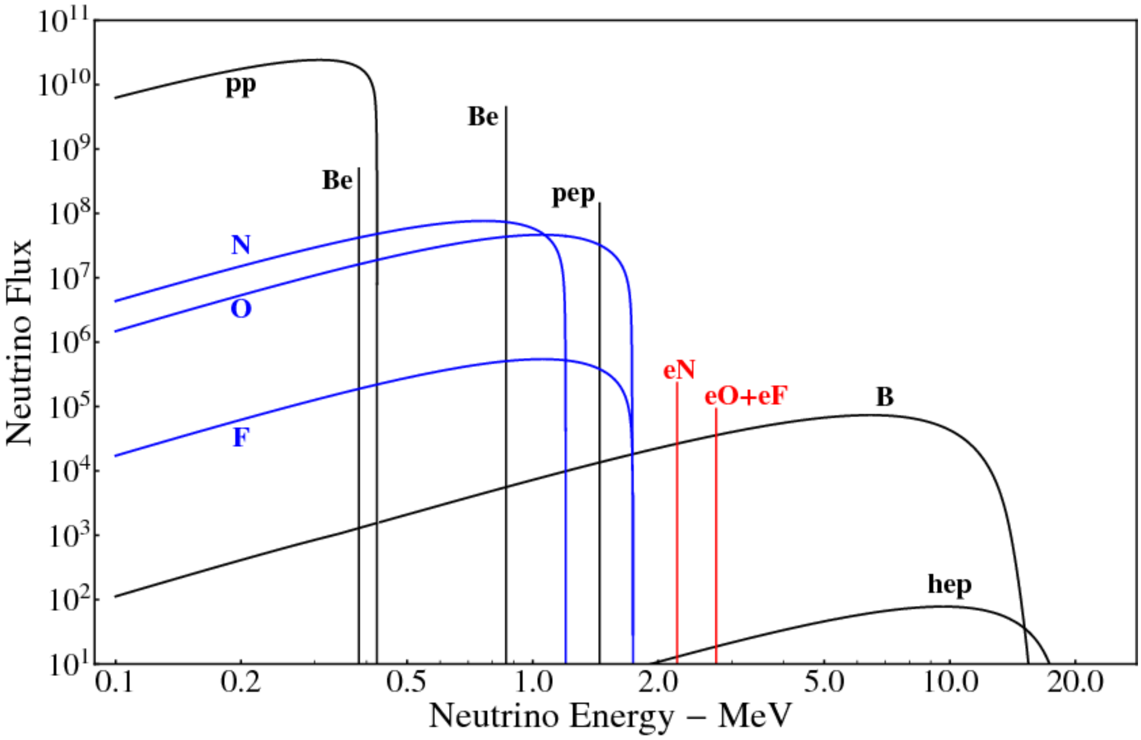

Figure 1.1: Solar neutrino spectrum, in $cm^{-2}s^{-1}$, for the different reactions which take place in the Sun [8].

1.2.3 Supernovae neutrinos

Supernovae are the most powerful cosmic sources of MeV neutrinos. These neutrinos play a very important role in the collapse and explosion of massive stars, since they carry energy directly from the innermost region of the explosion.

The first supernova for which a neutrino counter part was detected was SN1987A, a gravitational collapse event localized in the Large Magellanic Cloud outside our Galaxy. Two water Cherenkov detectors, Kamiokande II and IMB, detected 20 events in total. 5 more events have been seen by the Baksan scintillator, confirming the baseline model of gravitational collapse [9]. The Nobel Prize of 2002 was awarded to the Kamiokande experiment also for this detection.

1.2.4 Geo-neutrinos

Geo-neutrinos are electron anti-neutrinos, produced by β^--decay of radioactive elements in the Earth's interior [10]. The most energetic reactions of this type are listed in Equations 1.6- 1.8:

$$^{238}U \longrightarrow ^{206} Pb + 8\alpha + 8e^- + 6\overline{\nu}_e + 51.7 \text{ MeV} \tag{1.6}$$

$$^{232}Th \longrightarrow ^{208} Pb + 6\alpha + 4e^- + 4\overline{\nu}_e + 42.7 \text{ MeV} \tag{1.7}$$

$$^{40}K \longrightarrow ^{20} Ca + e^- + \overline{\nu}_e + 1.31 \text{ MeV} \tag{1.8}$$

The energy spectra of geo-neutrinos released in these reactions are shown in Figure 1.2.

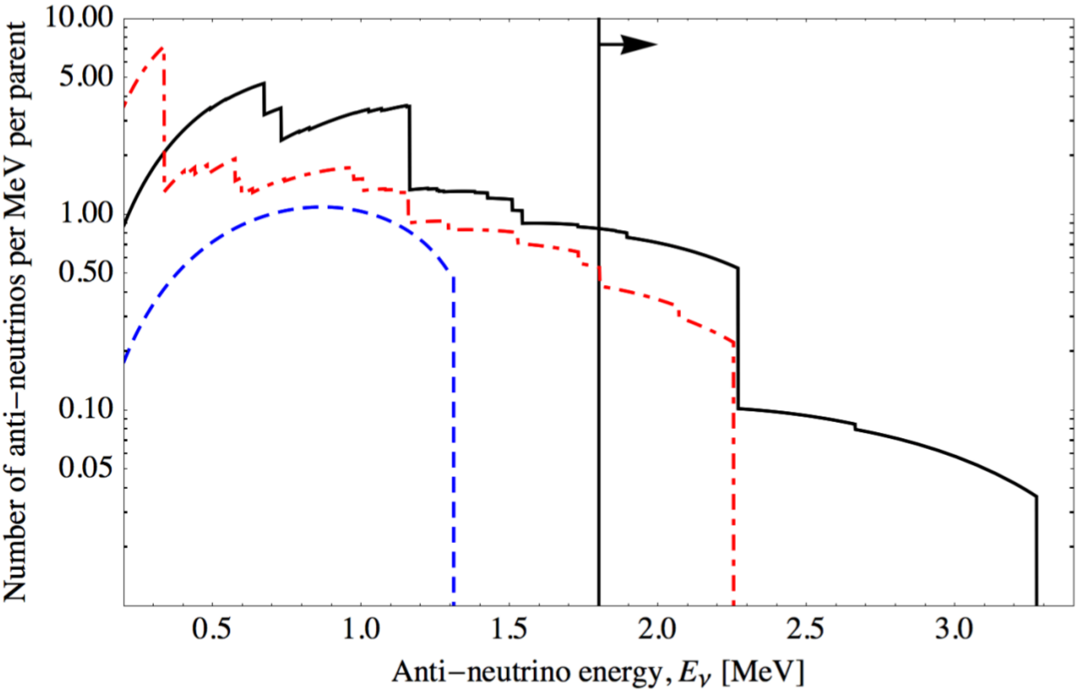

Figure 1.2: Energy spectra of geo-neutrinos released in the reactions of Equations 1.6, 1.7 and 1.8: ^{238}U chain in solid black line, ^{232}Th chain in dashed-dotted red line, and ^{40}K chain in dashed blue line. The vertical solid line shows the kinematic threshold (1.806 MeV) of the inverse β-decay interaction [10].

Geo-neutrinos can be detected through inverse β-decay, but, since the kinematic threshold for this reaction is at 1.806 MeV, we can immediately see from Figure 1.2 that anti-neutrinos produced by the ^{40}K chain cannot be detected, while neutrinos coming from the other two reaction chains have been measured by Borexino [11].

The importance of geo-neutrinos resides is the possibility to measure in an independent way the energy production in the Earth interior.

1.2.5 Atmospheric neutrinos

Electron and muon neutrinos are produced through the interaction of cosmic rays with the particles in the Earth atmosphere. Typically, in these interactions, many pions, and less abundantly kaons, are produced. These mesons decay to other particles, producing also neutrinos. The most abundant reaction chains are:

$$\pi^+ \longrightarrow \mu^+ + \nu_\mu, \quad \mu^+ \longrightarrow e^+ + \nu_e + \overline{\nu}_\mu \tag{1.9}$$

$$K^+ \longrightarrow \mu^+ + \nu_\mu, \quad \mu^+ \longrightarrow e^+ + \nu_e + \overline{\nu}_\mu \tag{1.10}$$

$$K^+ \longrightarrow \pi^0 + e^+ + \nu_e \tag{1.11}$$

The critical energy, namely the energy below which the particle most likely decays before reaching the Earth, is of $\sim$ 115 GeV for pions, $\sim$ 850 GeV for kaons, and $\sim$ 1 GeV for muons [12]. The total atmospheric neutrino flux, as computed by Honda et al. [13] for the Super-Kamiokande (SK) site, in the energy range $E_\nu \in [10^{-1} - 10^4]$ GeV, is shown in Figure 1.3; in Figure 1.4, the ratio between the muon and eletron neutrino fluxes, $\Phi(\nu_\mu + \overline{\nu}_\mu)/\Phi(\nu_e + \overline{\nu}_e)$, as a function of the neutrino energy, as well as the ratio between neutrino and anti-neutrino fluxes, $\Phi(\nu)/\Phi(\overline{\nu})$, are also shown. In the analyses presented in this thesis the Honda flux computed for the Fréjus site is used, which is identical to the one here presented for SK in the energy range $E_\nu > 20$ GeV.

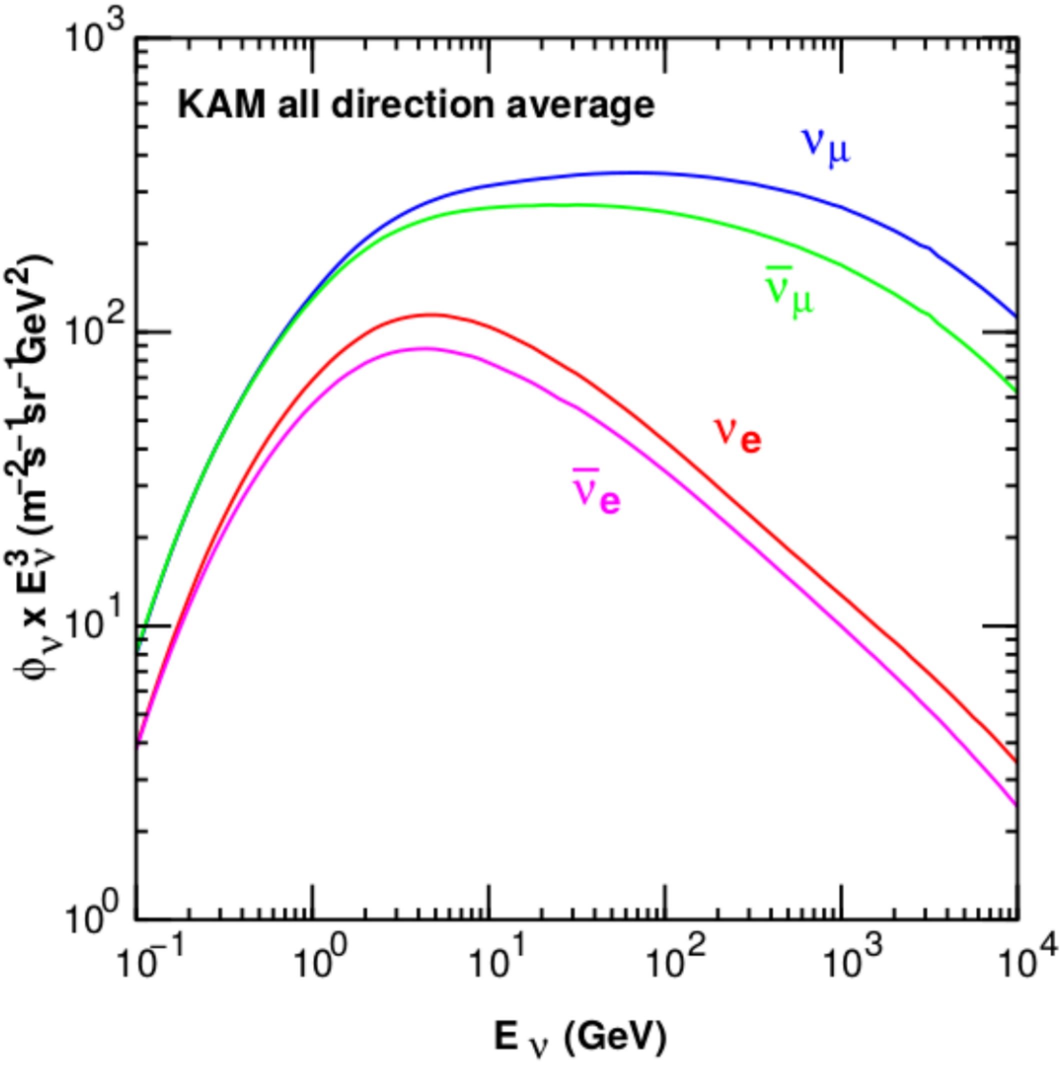

Figure 1.3: All direction averaged atmospheric neutrino flux for the SK site, averaged over one year. The neutrino flux has been multiplied by E^3 in order to better display the different features [13].

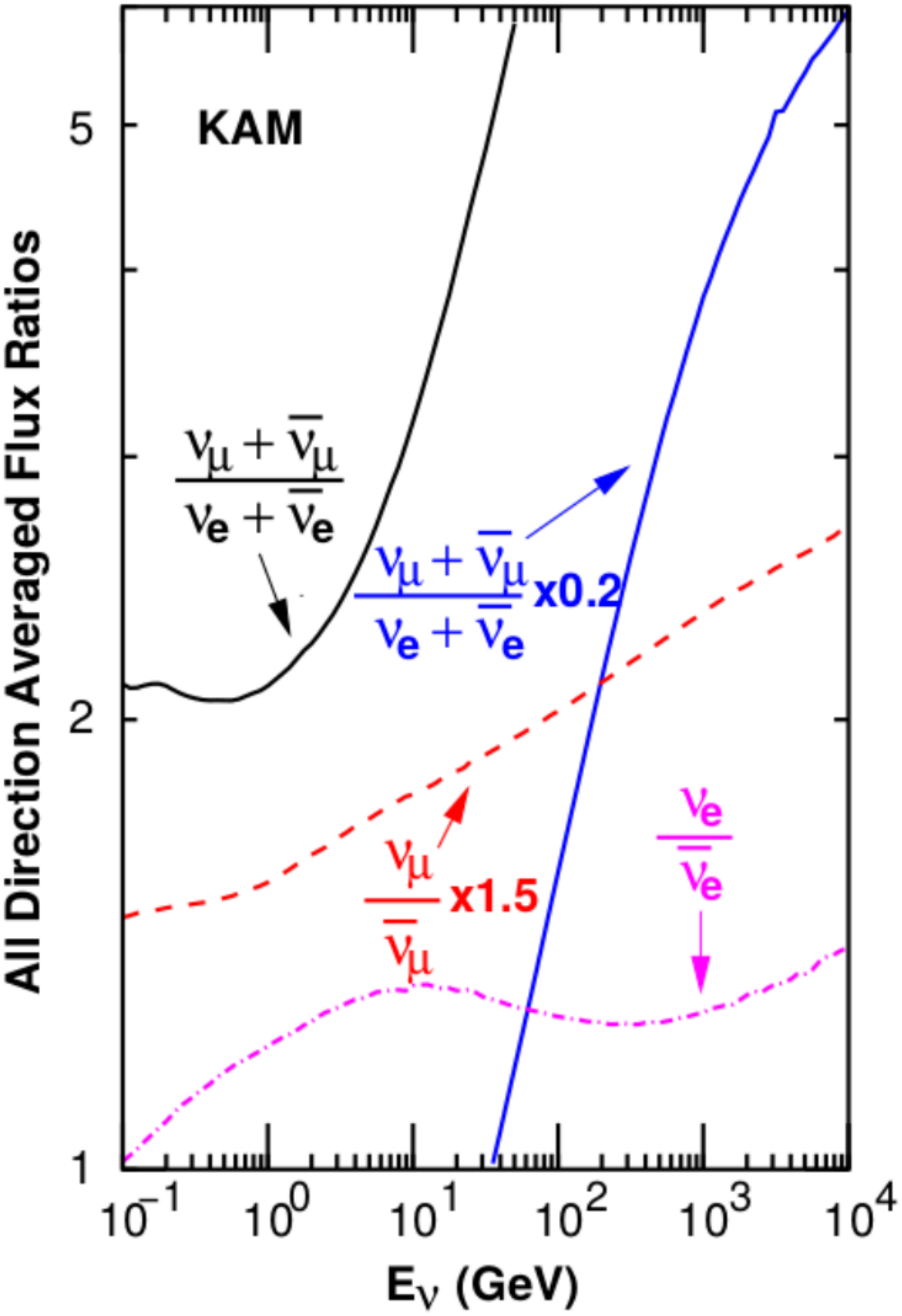

Figure 1.4: Neutrino flavour-ratio calculated with the all-direction and one-year averaged atmospheric neutrino flux at the SK site [13].

As we will see in the next subsection, the primary cosmic-ray flux decreases rapidly with the energy. Therefore, also the calculated neutrino flux steeply decreases with the increasing energy, as can be inferred by Figure 1.3.

The main dependence of the neutrino fluxes on the location on the Earth is caused by the Earth's magnetic field, which is also responsible for zenith and azimuth angle variation at each position. This effect, however, affects events at energies which are irrelevant for the studies presented further in this thesis. Another effect contributes to create a zenith asymmetry of the neutrino flux and it is due to the fact that higher energy muons hit the Earth's surface and stop before decay; for vertical muons this happens at energies above 3 GeV, for which the path length is of around 20 km; while, for horizontal muons, path lengths up to 500 km are possible, resulting in a larger composition of higher energy neutrinos in the horizontal fluxes [14].

The major sources of error on the estimation of the atmospheric neutrino fluxes come from uncertainties in hadron production and in the primary flux. In [14] these uncertainties are taken into account and error on the expected absolute atmospheric neutrino fluxes, as well as on the fluxes ratios are derived. A parameterization of such errors has been used in the analyses performed within this thesis (see Chapter 6 for details).

1.2.6 Cosmic neutrinos

Cosmic rays were first discovered in 1912, when the Austrian physicist V. Hess made a historic balloon flight. He ascended to 5300 m, and, measuring the rate of ionization in the atmosphere, he found a value three times larger than the one at sea level. His results proved that penetrating radiation was entering the atmosphere from above.

Today we know that these high-energy particles arriving from outer space are mainly (89%) protons, but they also include nuclei of Helium (10%) and heavier nuclei (1%). Their energies spread over 10 orders of magnitude and reach values of the order of 10^{20} eV. The flux decreases steeply, following a broken power law of the energy:

$$\frac{dN(E)}{dE} \propto E^{-\gamma} \tag{1.12}$$

where the spectral index γ varies between 2.7 and 3.0 (see Figure 1.5). The steepening that occurs between 10^{15} and 10^{16} eV is known as the *knee* of the spectrum. The feature around $10^{18.5}$ eV is called the *ankle* of the spectrum.

The mechanism behind particle accelerations in cosmic rays sources was originally investigated by Fermi, in 1949. His idea was that a charged particle traveling through a shock wave, such as the ones in jets and at the hotspots of radio sources, can be reflected back at increased velocity. If a similar process occurs also in the opposite direction, the particle will keep gaining energy trough a series of multiple reflections. This process, when applied to multiple particles, results in an energy spectrum which follows exactly the cosmic rays power law, described in Equation 1.12.

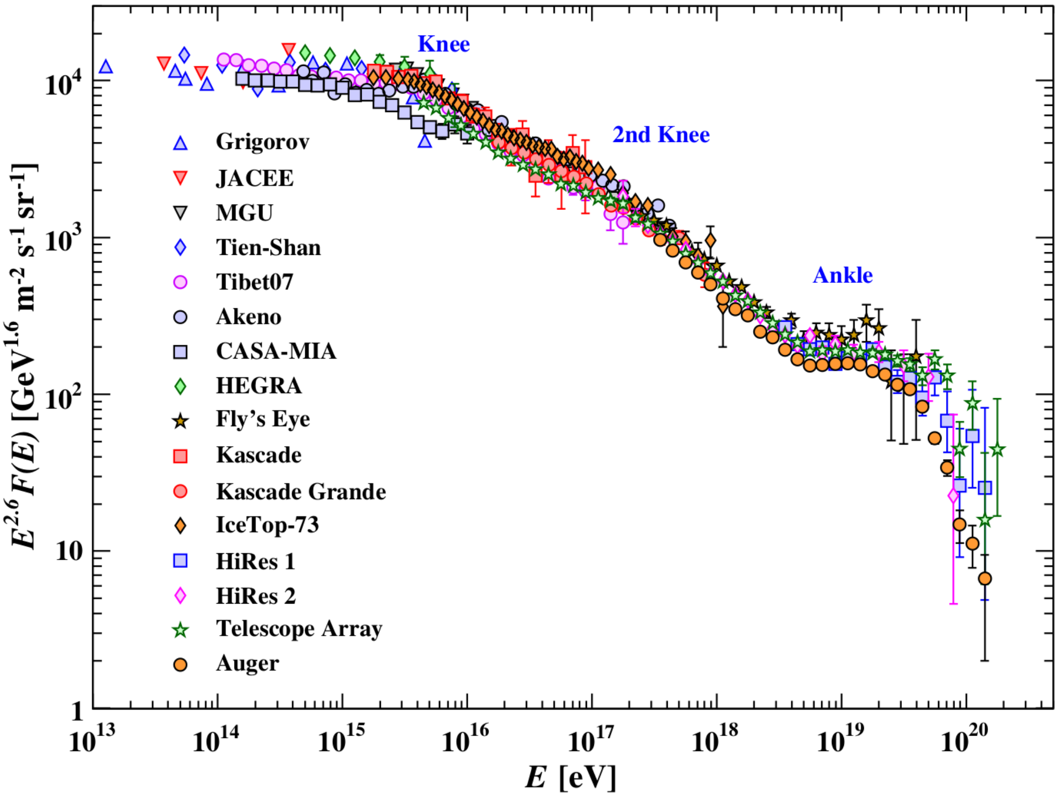

Figure 1.5: The all-particle spectrum as a function of E (energy-per-nucleus) from air shower measurements. The differential energy spectrum has been multiplied by $E^{2.6}$ in order to display the features of the steep spectrum that are otherwise difficult to discern [15].

Information on the original direction is lost, since all the charged cosmic particles are deflected by interstellar and intergalactic magnetic fields. On the other hand, also photons and neutrinos have to be produced in the cosmic ray sources during secondary reactions, and they can be used for directionality studies, as well as to understand the acceleration mechanism of these objects.

Even if the origin of the more energetic cosmic rays is still unknown, several sources have been identified which are thought to be responsible for cosmic rays emission. The first atmospheric Cherenkov telescope was WHIPPLE, a 10 m γ-ray telescope located at the Fred Lawrence Whipple Observatory in Southern Arizona. This telescope was in operation from 1968 to 2013, and detected the first TeV γ-ray source, the Crab Nebula, in 1989 [16]. WHIPPLE was followed by VERITAS (Very Energetic Radiation Imaging Telescope Array System) [17], which has been in operation since February 2005. The H.E.S.S. (High Energy Stereoscopic System) experiment consists of a system of imaging atmospheric Cherenkov telescopes that investigates cosmic gamma rays in the energy range from tens of GeV to tens of TeV. Up to now the H.E.S.S. Collaboration discovered 83 sources [18]. The MAGIC telescope is located on the Canarian island of La Palma, at 2200 m above sea level. It has allowed the discovery of very-high-energy gamma rays from 3C279, the farthest blazar detected in this energy range, as well as the first observation of the very-high-energy pulsed emission from the Crab pulsar [19]. Several other X-rays sources have been tabulated thanks to these experimental setups, which allow to detect photon with energy above 1 TeV.

Cosmic rays can be studied not only by telescope on the ground, but also trough satellite in space. It's the case of the NASA Fermi Gamma-ray Space Telescope [20], launched on June 2008 and sensitive to photons energies from 8 keV to 300 GeV.

As previously said, also neutrinos are expected to be produced in cosmic rays sources. In 2013, the IceCube Collaboration reported the first observation of two PeV cosmic neutrinos [21], opening a new era in neutrino astronomy. Furthermore, on July 2018, IceCube announced the first observation of a cosmic neutrino in spatial coincidence to the known blazar TXS 0506+056 which was known to be in a flare state, suggesting that this kind of astrophysical objects may be a source of high-energy neutrinos [22].

1.2.7 Reactor and accelerator neutrinos

Neutrinos can be produced also artificially, both through nuclear reactors and particle accelerators.

Nuclear reactors are powerful sources of electron anti-neutrinos. The main process taking place in a nuclear reactor is the fission of elements such as ^{235}U, ^{238}U, ^{239}Pu and ^{241}Pu, which produces unstable neutron-rich nuclei, which in turn decay trough β-decay, producing approximately six electron anti-neutrinos per fission. The energy of these neutrinos are of the order of the MeV (see Figure 1.6).

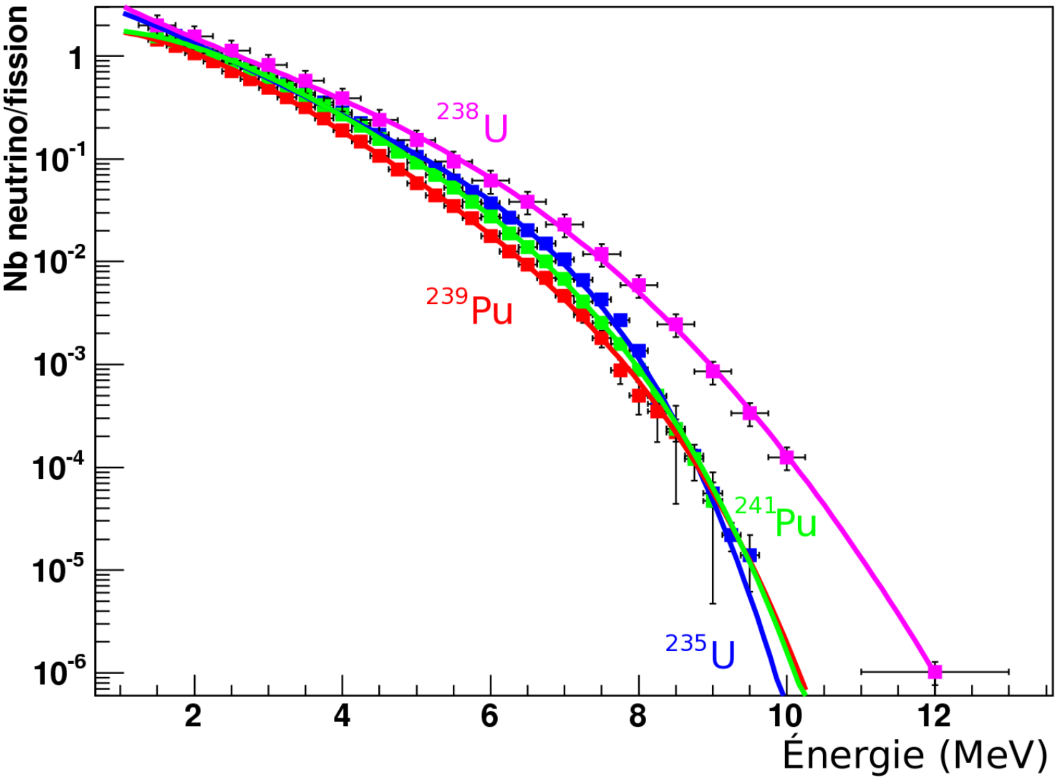

Figure 1.6: $\overline{\nu}_e$ spectra of the four dominant fissioning isotopes [23].

The detection principle is still identical to the one first exploited by Reines (see Section 1.1).

In a typical accelerator experiment (see Figure 1.7), a proton beam is launched towards a target, in such a way to produce secondary particles, mainly pions, which in turn decay producing neutrinos. All particles in the beam, except for the neutrinos which continue on to the experiment, are removed through a dedicated shielding, or "beam stop".

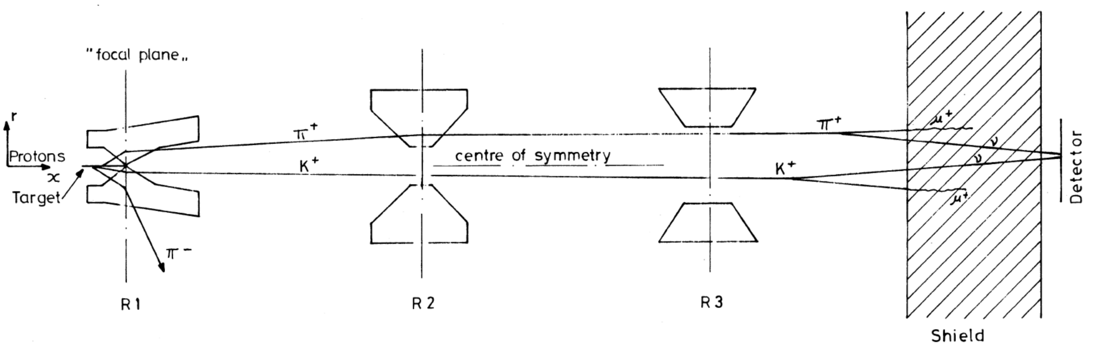

Figure 1.7: Schematic representation of an accelerator neutrino experiment [24].

A "two detectors configuration" is often employed: the *near* detector measures directly the energy spectrum of neutrinos from the beam, while the *far* detector measures the energy spectrum after neutrinos have propagated. Deviations between the two energy spectra may be used to infer the presence of neutrino oscillations.

1.3 Neutrino interactions

The reason why neutrinos are so difficult to detect is that their interaction cross section is really small (see Figure 1.8). This is due to the fact that the cross section, σ, is proportional to the square of the transition matrix element, M_{fi}^2, which in turn is proportional to the inverse of the square of the carrier boson mass:

$$\sigma \propto M_{fi}^2 \propto \frac{g^4}{(M_{Z,W}^2 - q^2)^2} \cdot s \tag{1.13}$$

where g is the weak charge (of the same order of the electric charge), $M_{Z,W}$ the mass of the exchanged boson ($M_Z = 91.1876 \pm 0.0021\,\mathrm{GeV/c^2}$, $M_W = 80.38 \pm\, 0.015\,\mathrm{GeV/c^2}$), q the transferred momentum, and s is the center of mass energy. In the energy range of interest, $M_{Z,W}^2 \gg q^2$, and, since $s \sim 2M_N E_\nu$ in the lab frame, where M_N is the mass of the target and E_ν the neutrino energy, one gets that $\sigma \propto E_\nu$.

In Figure 1.8 the neutrino and anti-neutrino interaction cross sections are shown as a function of the neutrino energy.

Depending on the exchanged boson, weak interactions are divided in *neutral current* (NC) interactions, when the neutral Z^0 mediates them, and *charged current* (CC) interactions, when there is an exchange of $W^{\pm}$.

Looking at Figure 1.8, one can see that, for neutrino energies below 2 GeV, the major contribution to the cross section comes from quasi-elastic processes (QE), in which the neutrino scatters off an entire nucleon. In a CC neutrino QE interaction, the target neutron is converted to a proton, while, in the case of an anti-neutrino scattering, the target proton is converted into a neutron [25]. At higher energies, neutrinos can bring the struck nucleon to an excited state, resulting in a baryon resonance (RES). In the energy range detectable by ANTARES (> 20 GeV), the main contribution to the total cross section is given by deep inelastic scattering (DIS), in which the neutrino scatters off a quark in the nucleon through the exchange of a virtual W or Z boson and produces a lepton plus a hadronic system in the final state.

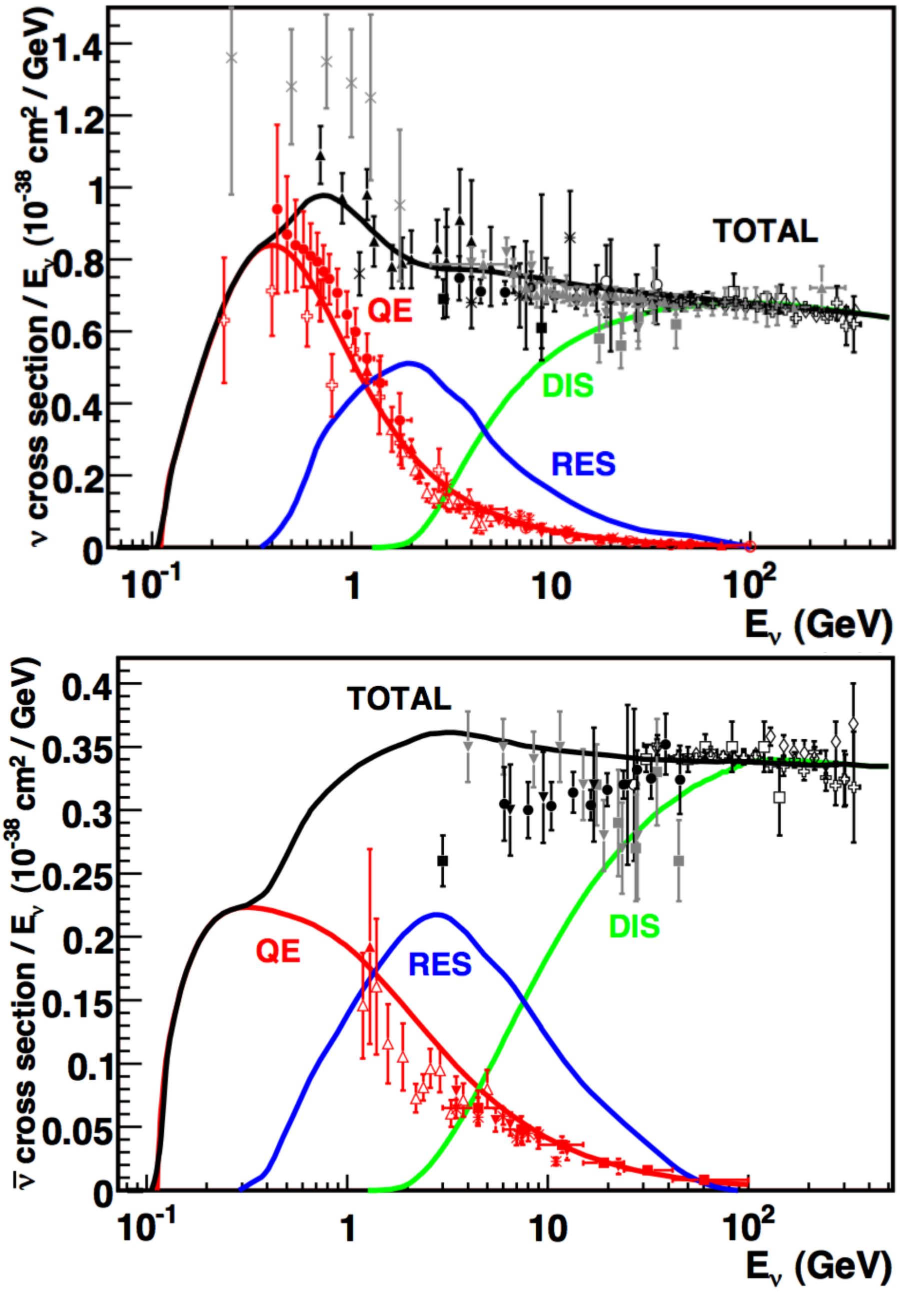

Figure 1.8: Neutrino (upper panel) and anti-neutrino (lower panel) cross sections, as a function of the neutrino energy. The total cross section as well as the different processes which contribute to it are shown (see text for details) [26].

In Figure 1.9 the Feynman diagrams for all the neutrino-nucleon DIS channels are illustrated.

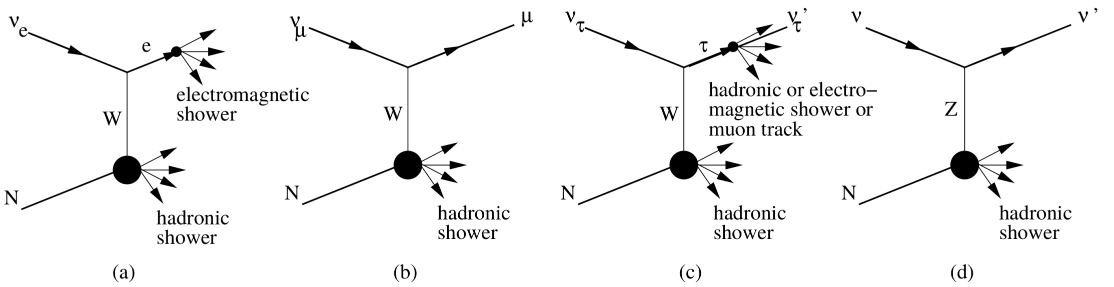

Figure 1.9: Neutrino-nucleon deep inelastic interaction channels. Charged current interactions of all three neutrino flavours (a-c) and neutral current interactions (d) identical for all neutrino flavours [27].

In CC processes, after neutrino interaction, the corresponding charged lepton (e, μ, τ) is produced. Electrons have a very short mean free path, then they produce secondary electromagnetic showers; muons, on the other hand, can travel freely from a few meters around 1 GeV up to several kilometers above 10 TeV, resulting in a clear track signal in the detector; taus, instead, rapidly decay producing muons, hadronic or electro-magnetic showers. NC processes, which are equal for all the neutrino flavours, produce a neutrino in the final state, plus a hadronic shower.

A neutrino interaction cross section model is needed in order to perform a neutrino oscillation analysis. For the analyses presented in this thesis work, neutrino cross sections have been computed through the GENHEN software [28] (see Chapter 4 for details), which simulates the DIS channel using LEPTO [29], and the other two main processes relying on the Rein-Sehgal (RS) model [30].

Uncertainties on the neutrino cross section models have to be evaluated and taken into account when performing an oscillation analysis, since they can result in variation on the total number of expected events, as well as in energy distribution shifts. The detailed treatment of such uncertainties will be described in Chapter 6.

1.4 Neutrino oscillations

The determination of the atmospheric neutrino oscillation parameters with the ANTARES neutrino telescope is the main goal of this thesis. Therefore in this

Section the theory of neutrino oscillations will be recalled, after a brief historical overview of the subject and together with the status of the experimental results.

1.4.1 A bit of history

The first idea of neutrino oscillations was advanced by B. Pontecorvo in 1957 [1]. He proposed, in analogy to the oscillations of the system $K^0 \leftrightarrows \overline{K}^0$ in the hadronic sector, which had been experimentally confirmed in the same years, the possibility of neutrino-anti-neutrino oscillations, since at that time only one neutrino flavour was known. After the discovery of the muon neutrino, in 1962, Pontecorvo started thinking also to possible $\nu_\mu \rightleftarrows \nu_e$ oscillations.

The first experimental evidence for neutrino oscillations came in the same period, by R. Davis, who was awarded of the Nobel Prize in 2002. His experiment was devoted to measure the neutrino flux form the Sun. The idea at the basis was to use the reaction

$$\nu_e +^{37}\mathrm{Cl} \rightarrow e^- +^{37}\mathrm{Ar} \tag{1.14}$$

to indirectly detect solar ν_e. The observed solar neutrino flux was around three times smaller than expected [31]. This result is known in the literature as the *Solar Neutrino Problem.* Some physicists explained this measurement with possible errors in the Solar model or in the experiment itself, but, on the other hand, this result triggered the development of new detectors, in order to understand better this phenomenon. The final proof of the existence of neutrino oscillations arrived in the Nineties, thanks to two independent experiments: Super-Kamiokande (SK) [32] and the Sudbury Neutrino Observatory (SNO) [33].

SK is a large water Cherenkov detector, consisting of a stainless-steel tank filled with 50000 tons of ultra pure water. About 13000 photo-multipliers are installed on the tank wall. The detector is located at 1000 meter underground in the Kamioka-mine, in Japan, and it started its data taking in 1996. Its main goal was the search for nucleon decay. Neutrinos were expected to arrive symmetrically from the two hemispheres, but scientists observed a deficit in the neutrinos coming from below and they hypothesized that the neutrinos traveling all the way through the Earth had had more time to oscillate [34].

SNO was built inside the INCO's Creighton mine, in Canada. The detector was a heavy-water Cherenkov detector designed to detect neutrinos produced by fusion reactions in the Sun. The main difference with respect to the previous solar neutrino experiment by Davis, was the capability to measure not only the flux of electron neutrinos, but the total flux of neutrinos of all flavours, using the neutral-current (NC) reaction:

$$d + \nu \rightarrow p + n + \nu \tag{1.15}$$

which allowed to determine the probability of flavour oscillations to occur. The SNO Collaboration, indeed, obtained the same results as Davis: only a third of the expected electron neutrinos from the Sun was detected. But the count of all three types of neutrinos together matched their expectations, and they could conclude that electron neutrinos must have changed into muon and tau neutrinos as they traveled [35].

Professors Takaaki Kajita and Arthur B. McDonald, leaders of the SK and SNO Collaborations respectively, were awarded of the Nobel Prize for Physics in 2015 for the discovery of neutrino oscillations.

1.4.2 Neutrino oscillations in vacuum

Neutrino oscillations can be explained in the quantum mechanical framework. They imply that neutrinos are massive particles and that, the so called *flavour* eigenstates, ν_e, ν_μ and ν_τ, are not the same as the so called *mass* eigenstates, ν_1, ν_2 and ν_3 with mass m_1, m_2 and m_3, respectively. Here we have used the convention such that ν_1, ν_2 and ν_3 are in decreasing admixture of the ν_e component. The two bases are related by a unitary matrix U:

$$|\nu_\alpha >= \sum_i U^*_{\alpha i} |\nu_i > \tag{1.16}$$

where the index α runs over the flavour eigenstates, while the index i runs over the mass eigenstates. The transformation matrix U is called Pontecorvo-Maki-Nakagawa-Sakata (PMNS), and can be parameterized by mean of three mixing angles, θ_{ij}, chosen to be confined as $0 \leq \theta_{ij} < \pi/2$, and a CP-violating phase, δ:

$$\begin{pmatrix} 1 & 0 & 0 \\ 0 & c_{23} & s_{23} \\ 0 & -s_{23} & c_{23} \end{pmatrix} \begin{pmatrix} c_{13} & 0 & s_{13}\exp^{-i\delta} \\ 0 & 1 & 0 \\ -s_{13}\exp^{i\delta} & 0 & c_{13} \end{pmatrix} \begin{pmatrix} c_{12} & s_{12} & 0 \\ -s_{12} & c_{12} & 0 \\ 0 & 0 & 1 \end{pmatrix} \tag{1.17}$$

where $s_{ij} = \sin\theta_{ij}$ and $c_{ij} = \cos\theta_{ij}$. The first matrix is usually called the *atmospheric* one, since the mixing angle θ_{23} is accessible by atmospheric neutrino experiments; the second matrix depends on parameters which are commonly measured in reactor neutrino experiments, while the last matrix is the *solar* one, since its parameters are the ones solar neutrino experiments are most sensitive to. The different kind of experiments and their determination of the neutrino oscillation parameters are discussed in the next Subsection.

If neutrinos were Majorana particles, two additional phases should be considered, but, since they do not affect the neutrino oscillation probabilities, they will be neglected through all the discussion.

The time evolution equation can be written as:

$$|\nu_i(t) >= \exp^{-iH_0t}|\nu_i(t=0) >= \exp^{-iE_it}|\nu_i(t=0) > \tag{1.18}$$

Assuming the three mass eigenstates have different masses, they will also have different energies, and they will propagate as waves of different frequencies. In this sense we can interpret the neutrino oscillations as an interference phenomenon. The time evolution equation for a flavour eigenstate will be, thus:

$$|\nu_\alpha(t) >= \Sigma_i \exp^{-iE_it} U^*_{\alpha i}|\nu_i >= \Sigma_i \exp^{-iE_it} U^*_{\alpha i}U_{\beta i}|\nu_\beta > \tag{1.19}$$

From Equation 1.19, one can directly calculate the oscillation probability between two different neutrino flavours, α and β:

$$P_{\alpha\to\beta} = | < \nu_\beta|\nu_\alpha(t) > |^2 = \Sigma_{i,j} \exp^{-i(E_i-E_j)t} U^*_{\alpha i}U_{\alpha j}U_{\beta i}U^*_{\beta j} \tag{1.20}$$

For relativistic neutrinos the following approximation holds:

$$E_i = \sqrt{p^2 + m_i^2} \sim E + \frac{m_i^2}{2E} \tag{1.21}$$

where we have used the convention $c = \hbar = 1$, and since in an actual experiment what is measured is the distance traveled by the neutrino and not the time, one gets:

$$P_{\alpha\to\beta} = \Sigma_{i,j} U^*_{\alpha i} U_{\alpha j} U_{\beta i} U^*_{\beta j} \exp(-i\frac{\Delta m^2_{ij}}{2E}L) \tag{1.22}$$

In a two flavours approximation, and assuming $\alpha \neq \beta$, Equation 1.22 would become:

$$P_{\alpha\to\beta} = \sin^2(2\theta)\sin^2(\frac{\Delta m^2_{ij}}{4E}L) \tag{1.23}$$

Let us now have a look in more detail at the different ingredients of this expression:

- The mixing angle θ tells us how flavour and mass eigenstates differ; if $\theta = 0$ then no mixing occurs, and no oscillation is possible; while, if $\theta = \frac{\pi}{4}$ the mixing between the two flavours is maximum.
- The difference between the square of the masses, Δm^2_{ij}, tells us that, for oscillations to occur, at least one of the mass states has to be different from zero. This implies neutrinos have to be massive particles. Moreover, different mass states must have different mass values, otherwise $\Delta m^2_{ij} = 0$ and no oscillation could happen.
- The parameter $\frac{L}{E}$ is the ratio between the distance the neutrino has traveled between the source and the detection point, and its energy. In some experiments, as the accelerator neutrino experiments, these parameters can be chosen in such a way to maximize the oscillation probability, provided one knows the most probable value for Δm^2_{ij}. In some other experiments, such as the ones which look at atmospheric neutrinos as ANTARES, both the neutrino energy and the traveled distance are chosen by Nature and vary in a wide range.

1.4.3 Neutrino oscillations in matter

When neutrinos are traveling through matter, their oscillation probability can be modified with respect to the vacuum case, due to coherent forward scattering from the particles in the medium. This effect is known as the Mikhaev-Smirnov-Wolfenstein (MSW) effect, from the names of the three scientists who first studied it [36]. Electron neutrinos and anti-neutrinos can undergo coherent forward scattering with electrons in matter both through neutral current and charged current interactions, while for the other neutrino flavours this process occurs only via neutral current. This different behavior of neutrinos in matter leads to the addition of a matter potential, V, in the Hamiltonian. In the 2 flavours approximation, one can write:

$$H_M = \frac{\Delta m^2}{4E} \begin{pmatrix} -\cos(2\theta) & \sin(2\theta) \\ \sin(2\theta) & \cos(2\theta) \end{pmatrix} + \begin{pmatrix} V & 0 \\ 0 & 0 \end{pmatrix} \tag{1.24}$$

The additional potential, V, depends on the electron density of the matter neutrinos are passing through, N_e, and on the Fermi constant, G_F:

$$V = \pm\sqrt{2} G_F N_e \tag{1.25}$$

and the ± sign refers to neutrinos and anti-neutrinos, respectively. With some matrix algebra, one can rewrite the Hamiltonian in a more compact form:

$$H_M^* = \frac{\Delta m^2}{4E} \begin{pmatrix} -\cos(2\theta) + A & \sin(2\theta) \\ \sin(2\theta) & \cos(2\theta) - A \end{pmatrix} \tag{1.26}$$

with $A = \pm\frac{2\sqrt{2} G_F N_e E}{\Delta m^2}$. In case of constant matter, the oscillation probability can be written in an analogous form of that in vacuum:

$$P_{\alpha\to\beta} = \sin^2(2\theta_M)\sin^2(\frac{\Delta m_M^2}{4E} L) \tag{1.27}$$

where:

$$\sin(2\theta_M) = \frac{\sin(2\theta)}{\sqrt{(\cos(2\theta) - A)^2 + \sin^2(2\theta)}} \tag{1.28}$$

$$\Delta m_M^2 = \Delta m^2 \sqrt{(\cos(2\theta) - A)^2 + \sin^2(2\theta)} \tag{1.29}$$

There are some interesting points one can infer from these expressions:

- When $A \ll 1$ the vacuum oscillation probability is recovered.
- A resonance condition is reached when $A = \cos(2\theta)$. When this condition

is encountered, the oscillation probability is maximally enhanced, for all non zero values of the vacuum mixing angle.

- Due to the fact that the matter induced potential differs in a sign between neutrinos and anti-neutrinos, the corresponding oscillation probabilities are different.

- Since the resonance condition occurs if $A > 0$, and this depends on the sign of Δm^2, matter effects can also be used to determine the neutrino mass hierarchy, which is still unknown (see Section 1.6 for details).

1.4.4 Status of experimental results in neutrino oscillations

In this Subsection some of the various experiments which led to our current understanding of the neutrino oscillation phenomenon are briefly described. As mentioned above, a single experiment can not be sensitive to the whole set of mixing parameters at once, but, dependently on the baseline and on the energy of the neutrinos under study, different regions of the parameter space can be investigated. Usually, the neutrino oscillation experiments are divided in two main categories:

- *Appearance* experiments, in which one has an initial flux of neutrinos of a certain flavour, and looks for neutrinos of a different flavour at the detection point;

- *Disappearance* experiments, in which starting from neutrinos of a certain flavour at the source, one looks at how many of them are detected in the same flavour at the detection point.

Solar and reactor neutrino experiments

Solar and reactor neutrino experiments are most sensitive to θ_{12}, Δm^2_{12} and θ_{13}. From the pioneering work of Davis, whose results opened the *Solar Neutrino Problem*, to the SNO experiment, which definitely confirmed that solar neutrinos are oscillating when traveling to the Earth (see Subsection 1.4.1), a lot of other experiments have been performed and others are currently taking data, in order to determine with more and more precision the solar neutrino oscillation parameters. One of the detection mechanisms exploited by these experiments is the use of radio chemical elements, through which the products of neutrino interactions can be captured and identified.

Three Gallium experiments started taking data in the ′90 s [37]: SAGE in Russia; GALLEX and its upgraded version GNO, in Italy. The employed reaction is:

$$\nu_e +^{71} Ga \rightarrow^{71} Ge + e^- \tag{1.30}$$

whose energy threshold of 0.233 MeV allows to detect neutrinos from the solar *pp* chain.

Borexino [38] is currently in operation at the Laboratori Nazionali del Gran Sasso, Italy. It has detected the mono energetic (862 keV) ^{7}Be electron capture neutrinos, via neutrino-electron scattering in an ultra-pure liquid scintillator.

The Kamiokande experiment, first designed to look for proton decay in 1983, was then converted into a solar neutrino experiment in 1985, to investigate on the *Solar Neutrino Problem.* It was the predecessor of Super-Kamiokande, and, it exploited the Cherenkov radiation produced by the relativistic products of neutrino interactions in the detector medium. The detection principle of a Cherenkov detector will be discussed in more details in the next Chapter.

The KamLAND experiment, located at the site of the earlier Kamiokande in the Kamioka mine (Japan) and surrounded by more than 50 nuclear power plants within a few hundreds of km, consists of 1 kton of ultra-pure liquid scintillator hosted in a transparent nylon balloon of 13 m diameter and suspended in a non-scintillating oil buffer. Around 1900 photomultiplier tubes (PMTs) surround the balloon. KamLAND has published data from 2.8 KTy of exposure [39]. Assuming no $\overline{\nu}_e$ disappearance, 2179 ± 89 events were expected; while 1609 events have been observed. The allowed region in the parameter space of Δm^2_{21} and $\tan^2\theta_{12}$ obtained by the KamLAND Collaboration, as well as the combined results with the solar neutrino experiments, is shown in Figure 1.10.

Combining data from SNO, SK and KAMLAND, made also possible to prove the matter effect in the Sun, induced by the MSW mechanism (see 1.4.3) [40]. A deficit of ν_e, as the one observed, was not compatible with a simple 2-flavour vacuum oscillation scenario, while it was in agreement with the fact that solar neutrinos, in passing from the Sun core to its surface undergo to a matter-induced resonance effect, which further reduces their survival probability.

The sign of Δm^2_{21} was found to be positive by these experiments, letting only the sign of Δm^2_{31} to be determined yet.

The determination of the mixing angle θ_{13} is quite recent and has been performed by reactor experiments, which can provide an unambiguous determination of this parameter. Three experiments have been built with this purpose: Daya Bay [41], Double Chooz [42], and RENO [43]. Among them, the Daya Bay is the most sensitive to the mixing angle θ_{13} and the one which first provided a precise measurement of it in 2012. At the Daya Bay nuclear power plant, with 6 reactors, eight anti-neutrino detectors, each one equipped with 20 ton target mass, are installed. On 8 March 2012, the Daya Bay Collaboration announced the discovery of a new disappearance of reactor anti-neutrinos at 5.2 standard deviations. The most recent analysis [44], in which systematic uncertainties as well as background estimation were improved, reported $\sin^2(2\theta_{13}) = 0.084 \pm 0.005$ and $|\Delta m^2_{ee}| = 2.44^{+0.10}_{-0.11} \times 10^{-3}\,\mathrm{eV}^2$, where $|\Delta m^2_{ee}|$ is defined such that $\Delta m^2_{ee} = \cos^2\theta_{12}\Delta m^2_{31} + \sin^2\theta_{12}\Delta m^2_{32}$ [45].

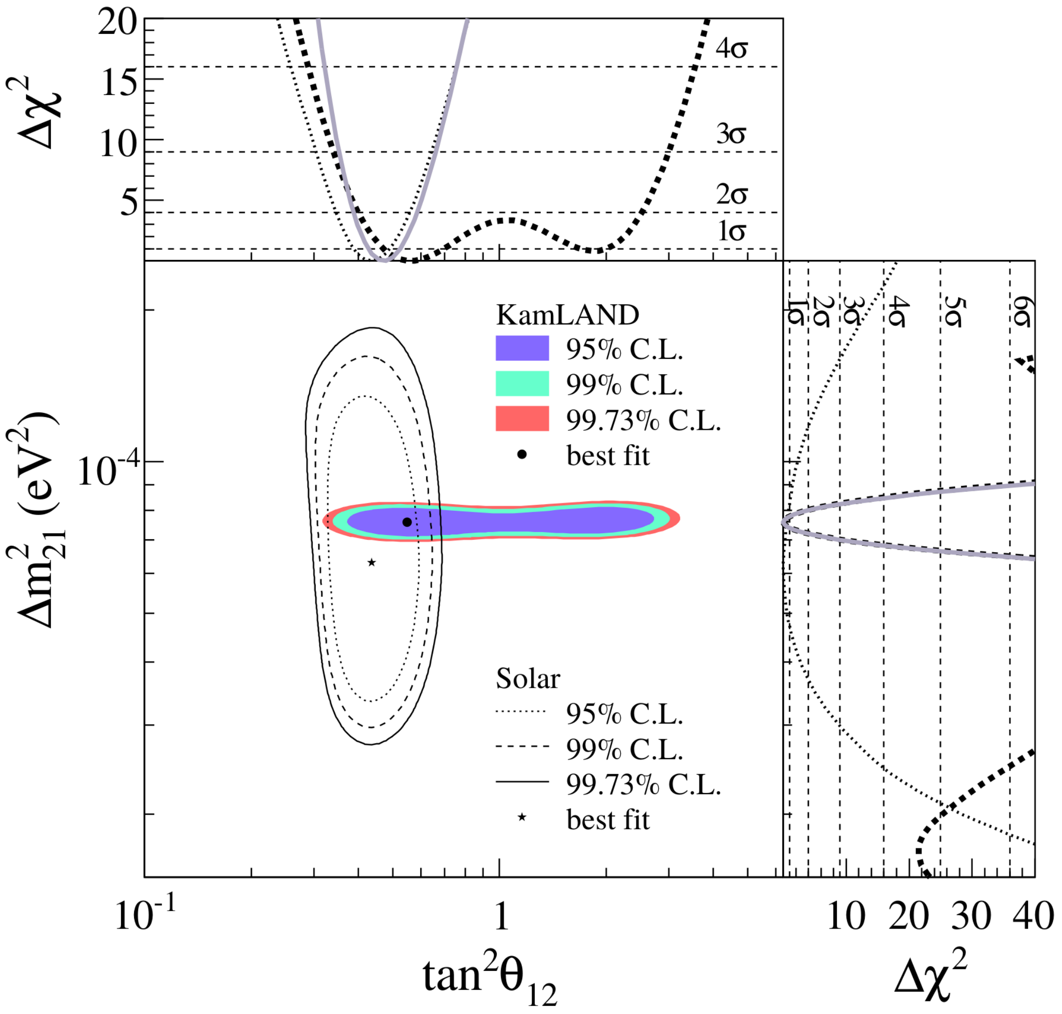

Figure 1.10: Allowed region for neutrino oscillation parameters from KamLAND and solar neutrino experiments. The side-panels show the $\Delta\chi^2$-profiles for KamLAND (dashed) and solar experiments (dotted) individually, as well as the combination of the two (solid) [39].

Atmospheric neutrino experiments

Atmospheric neutrino experiments can determine the value of the mixing angle θ_{23} and the mass splitting Δm^2_{32}. The main channel they investigate is the survival probability of muon neutrinos and anti-neutrinos. Atmospheric neutrinos coming from above travel a distance of around 10 km; on the other hand, atmospheric neutrinos which have passed through the Earth traveled for thousands of kilometers, therefore undergoing oscillations. Moreover, the presence of matter could enhance the oscillation probability as well.

As seen in Subsection 1.4.1, the Super-Kamiokande experiment was the first to report a clear evidence of the oscillations in the atmospheric sector. The detector has now collected more than 11 years of data, improving more and more the precision on the atmospheric oscillation neutrino parameters [46]. A recent analysis, which includes a three-flavour scenario and matter effects led to the results shown in Figure 1.11.

Deep-water (ice) Cherenkov detectors have also been employed to study atmospheric neutrino oscillations, even though their primary goal is focused toward higher energy neutrinos.

The ANTARES neutrino telescope will be introduced in more detail in the next Chapter. A previous analysis aimed to put constraints on the atmospheric oscillation parameters with ANTARES had been conducted [47], using 863 days of detector lifetime, from 2007 to 2010. One of the main goal of this thesis is to improve the sensitivity already reached by it, exploiting the whole ANTARES data set and refining the analysis procedure, and it will be described in details in Chapter 6.

IceCube is an ice Cherenkov detector situated at South Pole. It is an array of 86 strings with 60 optical modules each. The strings are arranged in a hexagonal grid with typical inter-string separation of 125 m. A denser instrumented region, called DeepCore, is placed in the center of the array and it is constituted by 8 strings separated by 50 m horizontally. This inner part allows to lower the energy threshold of detectable neutrinos, making DeepCore a more suitable detector for the study of oscillations. In 2017 the IceCube Collaboration published an analysis using three years of data [48], improving their current precision on the determination of Δm^2_{32} and θ_{23} (see Figure 1.11).

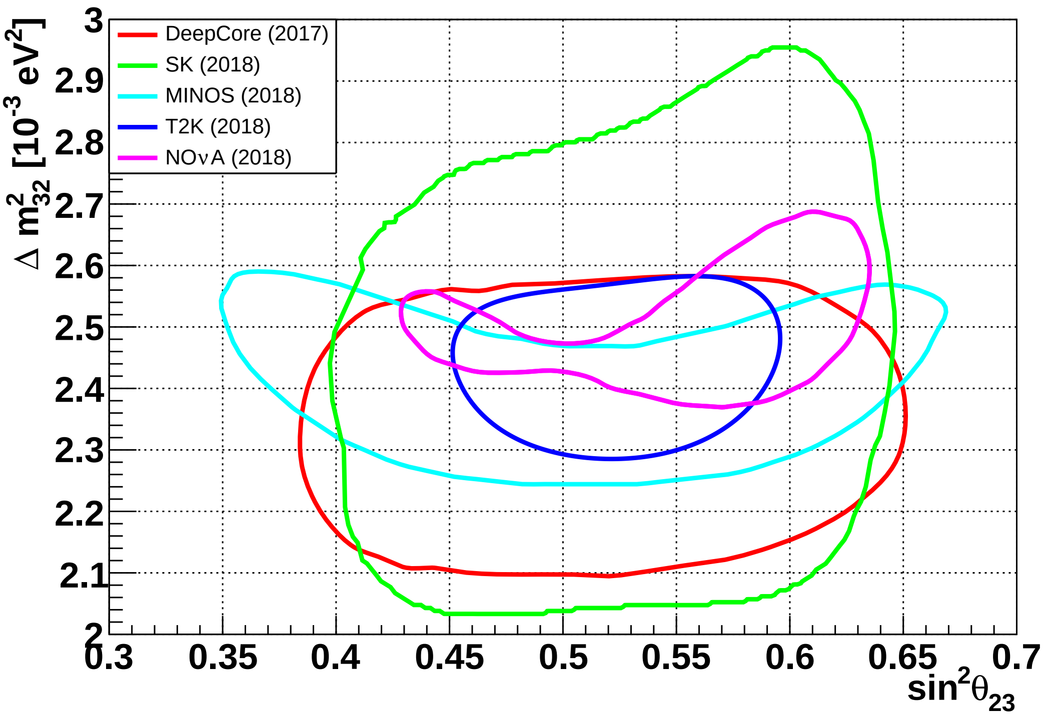

Figure 1.11: The 90% CL allowed region for $\sin^2\theta_{23}$ and Δm^2_{32} from IceCube-DeepCore [48] (red), SK [46] (green), NOνA [49] (purple), T2K [50] (blue) and MINOS [51] (light blue).

IceCube is planning an additional low energy extension, called PINGU (Precision IceCube Next Generation Upgrade), to be deployed inside the existing instrumented volume. If funded, the new detector could be installed within the next decade [52].

The next generation of deep-water Cherenkov detectors is called KM3NeT [53]. It consists of a multiple-site detectors: one dedicated to the study of cosmic neutrinos, ARCA, in Italy; and one smaller but denser, for GeV neutrinos studies, ORCA, in France. The first detection line of ORCA has been deployed in September 2017, and the complete setup is expected to be ready after four years of construction.

Accelerator neutrino experiments

Particle accelerator neutrino experiments allow to constrain the parameters Δm^2_{32} and the mixing angles θ_{23} and θ_{13}, even though this last measurement depends on the unknown value of δ_{CP}.

T2K (Tokai to Kamioka) [54] is a long-baseline neutrino experiment in Japan, focused on the search for oscillations from muon neutrinos to electron neutrinos. The T2K experiment sends an intense beam of muon neutrinos from Tokai to Kamioka, at a distance of 295 km. The neutrino energy is peaked at around 600 MeV, which is the value at which the maximum oscillation probability is expected for that baseline. In 2011, the T2K Collaboration announced the first evidence of oscillations from muon neutrinos to electron neutrinos, which had never been observed before. The most updated results by T2K [50] are shown in Figure 1.11.

NOνA is another long-baseline neutrino oscillation experiment, situated at the Fermi National Accelerator Laboratory. The distance traveled by neutrinos before detection is around 810 km and a couple of near and far detector is employed. Recently, the NOνA Collaboration presented their latest results in terms of oscillations [49] (see Figure 1.11).

Global fit

In this Subsection the results obtained by one of the most recent global fit of neutrino oscillation parameters are presented. These results have been used to fix the values of the oscillation parameters when constructing a pseudo-data sample for the MC sensitivity study which has been performed for the main analyses presented in this thesis (for details see Chapter 6 and 7).

There are several groups working on combining the most updated results from the various experiments and providing a global picture of the neutrino oscillation parameters. For details on the different results, see [55, 56, 57]. We will follow the results presented in [55]. Here the followed procedure is briefly summarized.

Data from solar experiments and from KamLAND are first combined with those from long-baseline accelerator experiments. The results are then merged with data from reactor neutrino experiments, which strongly constrain θ_{13}. Finally, atmospheric neutrino results are added. At all the different steps, the results are obtained through a χ^2 minimization, where the minimizing function depends on the oscillation parameters and on a set of nuisance systematic parameters. In Table 1.1 the results of the global fit are shown.

Parameter	**Best Fit**	**3 σ**
Δm^2_{21} [10^{-5} eV^2]	7.37	6.93-7.97
$\lvert\Delta m^2\rvert$ [10^{-3} eV^2]	2.50 (2.46)	2.37-2.63 (2.33-2.60)
$\sin^2\theta_{12}$	0.297	0.250-0.354
$\sin^2\theta_{23}$	0.437 (0.569)	0.379-0.616 (0.383-0.637)
$\sin^2\theta_{13}$	0.0214 (0.0218)	0.0185-0.0246 (0.0186-0.0248)

Table 1.1: The best-fit values and 3 σ allowed ranges of the 3-neutrino oscillation parameters as computed by [55]. The values (values in brackets) correspond to $m_1 < m_2 < m_3$ ($m_3 < m_1 < m_2$); the definition of Δm^2 is: $\Delta m^2 = m_3^2 - (m_2^2 + m_1^2)/2$.

1.5 Sterile neutrino

In the previous Section we have seen how neutrino oscillations have been established by a variety of experiments. However, some of the obtained results present a deficit or an excess of events, which can not be explained within the three flavours scenario. On the contrary, they suggest the presence of an additional neutrino, which does not take part to the weak interaction, but whose presence can modify the oscillation paths of the *standard* neutrinos. This additional flavour is called *sterile* neutrino, in order to emphasize the fact that it does not interact as the others. In this Section the formalism of the 3+1 model is briefly discussed; then, the experimental *anomalies* which have been observed and which can be explained within a 3+1 flavours scenario are revised, together with the main setups which have been built in order to throw light on this subject.

1.5.1 The 3+1 model

Since the discovery of neutrino oscillations, which definitely proved that neutrinos are massive particles, there have been several theoretical attempts to explain why the neutrino mass scale is so much lower than the one for quarks and charged leptons. Among the various models, the *seesaw* mechanism, for instance, predicts the existence of one *sterile* neutrino for each *active* flavour, which is supposed to be much heavier, and has yet to be observed.

The simplest extension to the standard oscillation scenario is the 3+1 model, which foresees the existence of one additional *sterile* neutrino. In this model, the mixing matrix introduced in 1.4.2 would be written as:

$$\begin{pmatrix} U_{e1} & U_{e2} & U_{e3} & U_{e4} \\ U_{\mu 1} & U_{\mu 2} & U_{\mu 3} & U_{\mu 4} \\ U_{\tau 1} & U_{\tau 2} & U_{\tau 3} & U_{\tau 4} \\ U_{s1} & U_{s2} & U_{s3} & U_{s4} \end{pmatrix} \tag{1.31}$$

where we have denoted with s the additional *sterile* flavour.

From the point of view of the parameters which describe the mixing between the mass and flavour eigenstates, adding a *sterile* neutrino means introducing six additional real terms: a new mass splitting, Δm^2_{41}, three new mixing angles, θ_{14}, θ_{24} and θ_{34}, and two new phases, δ_{14} and δ_{24}.

The experimental anomalies illustrated in the next subsections are explained within a neutrino oscillation scenario with a $\Delta m^2_{41} \gtrsim 0.1\,\mathrm{eV}^2$.

As we have already discussed for the standard oscillation case, different experiments are sensitive to different oscillation channels, which in turn means that different oscillation parameters can be studied and constrained by different setups. In the following subsections a brief overview on the main experimental results and the current status of our knowledge on the *sterile* neutrino mixing parameters is given for the main oscillation channels under investigation.

1.5.2 ν_e and $\bar{\nu}_e$ disappearance

Solar and reactor neutrino experiments are sensitive to the electronic channel, which can help in constraining $|U_{e4}|^2 = \sin^2\theta_{14}$ and thereby controlled by the mixing angle θ_{14}.

Several experimental anomalies were observed in this oscillation channel by various experiments. GALLEX and SAGE, two solar neutrino experiments, reported a measured number of events with calibration source which is 2.8σ smaller than expectations [58], and which could be explained in a 3+1 scenario. Furthermore, updated calculations of $\overline{\nu}_e$ rate from nuclear rectors have been recently provided [59], implying that the previous rates measured by all rector neutrino experiments within 100 m from the core are around 6% too low. This result is known as the *reactor anti-neutrino anomaly*, and triggered several further investigations by different collaborations, aimed to both revise the expected flux calculation and search for possible sterile neutrinos. The Daya-Bay Collaboration recently observed a correlation between reactor core fuel evolution and changes in the reactor anti-neutrino flux and energy spectrum [60], which could explain the observed event deficit and indicates as main source of the *reactor anti-neutrino anomaly* an incorrect prediction of the ^{235}U flux. Another recent analysis showed that the Daya-Bay data are well-fitted with composite hypotheses including variations of the ^{235}U or ^{239}Pu fluxes in addition to active-sterile neutrino oscillations [61].

Moreover, in 2014, the RENO Collaboration reported the observation of an event excess around 5 MeV [62], which was then seen also by DayaBay [63] and Double-Chooz [64]. This anomaly cannot be explained with the addition of another neutrino, but it is thought to be related to the measurement of the neutrino flux, showing once again the crucial role that the flux model has in this kind of experiments.

The global 3+1 fit [65] showing the current limits provided by solar and reactor neutrino experiments, as well as the preferred regions of the above-mentioned anomalies, is presented in Figure 1.12.

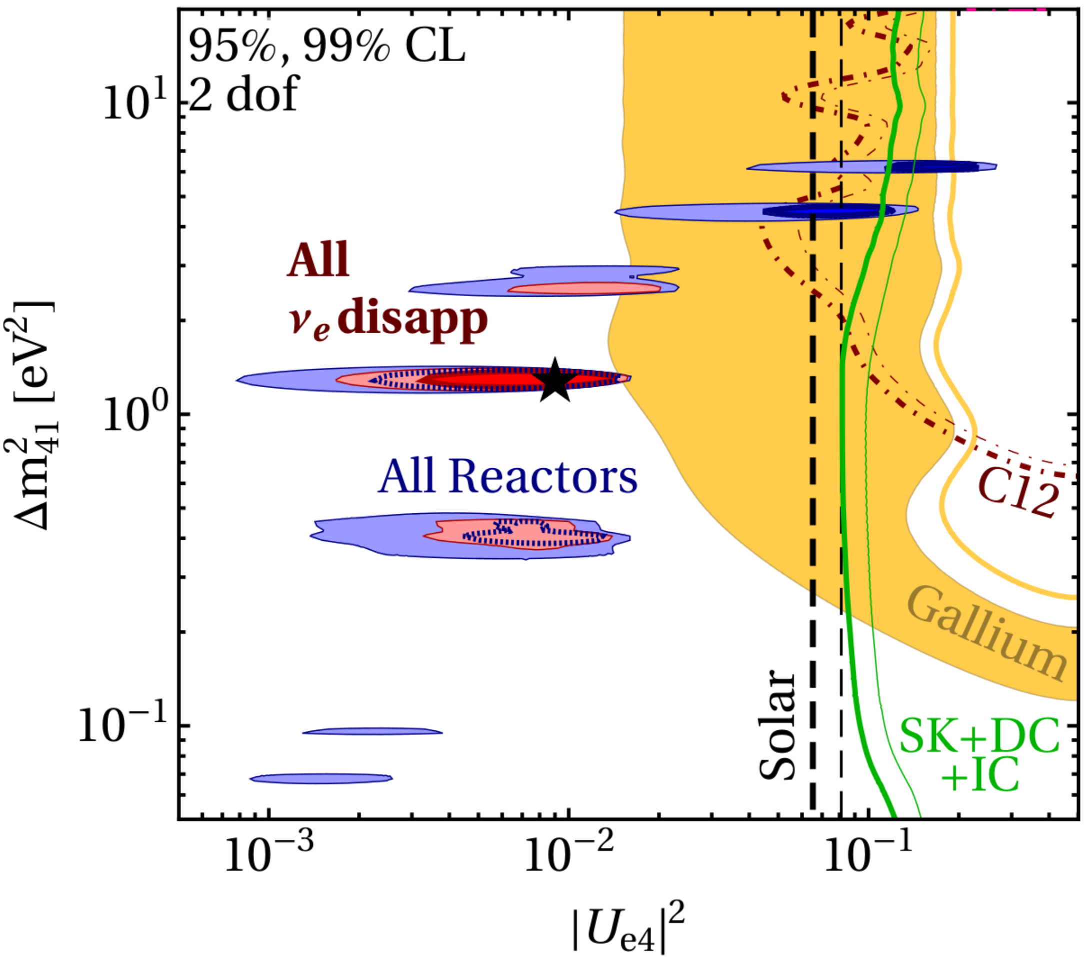

Figure 1.12: Constraints on $\nu_e/\bar{\nu}_e$ disappearance in the 3+1 scenario. The preferred parameter regions at 95% and 99% CL are shown, projected onto the plane spanned by the mixing matrix element $|U_{e4}|^2$ and the mass squared difference Δm^2_{41}. The parameter space inside the shaded areas and to the left of the exclusion curves is allowed. For details on the included data and the followed procedure, see [65].

1.5.3 ν_μ and $\bar{\nu}_\mu$ disappearance

Atmospheric neutrino experiments are more sensitive to the $\nu_\mu/\bar{\nu}_\mu$ disappearance channel. In a 3+1 scenario, the survival probability of muon neutrinos and antineutrinos is regulated by the two mixing angles θ_{24} and θ_{34}, via the matrix elements $|U_{\mu 4}|^2 = \sin^2\theta_{24}$ and $|U_{\tau 4}|^2 = \sin^2\theta_{34}\cos^2\theta_{24}$.

Two different regimes have been studied so far: the first method exploits the energy range close to the first standard oscillation minimum. In Figure 1.13, the survival probability for a vertically up-going atmospheric ν_μ is shown as a function of its energy, for different values of the mixing angles θ_{24} and θ_{34}.

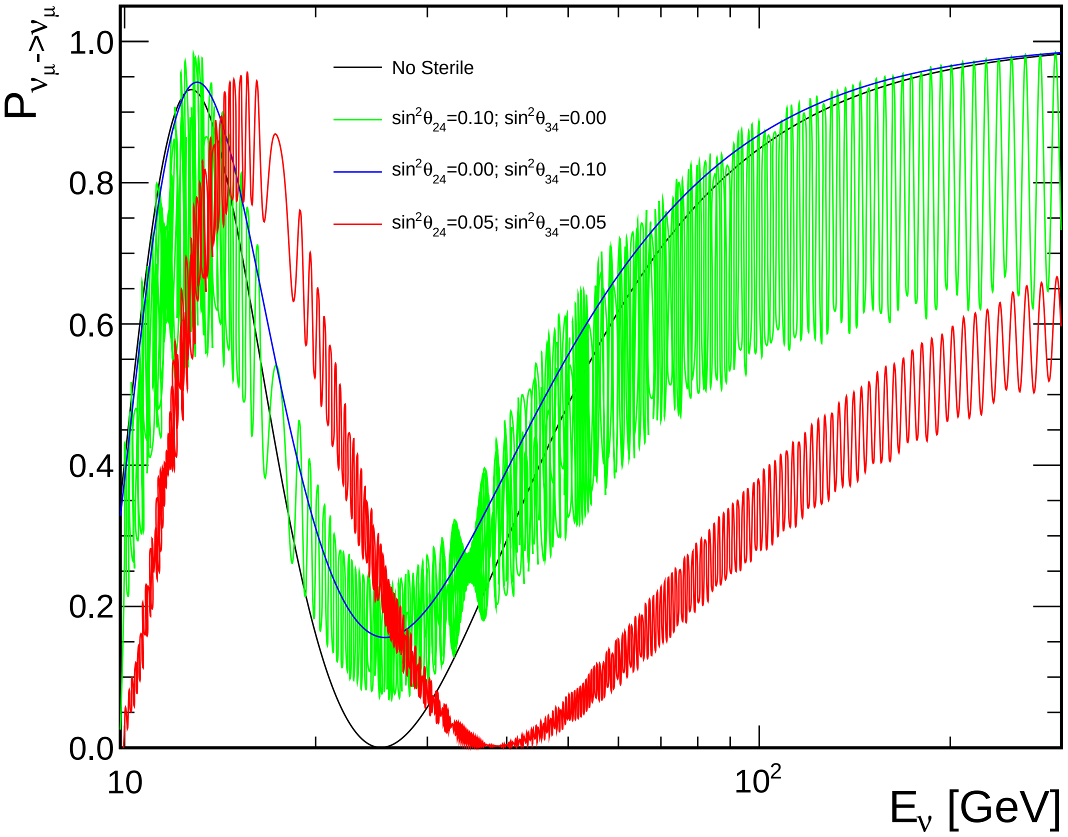

Figure 1.13: Survival probability for a vertically up-going ν_μ as a function of its energy, for different values of the mixing angles θ_{24} and θ_{34}.

As can be seen from the figure, the effect of these two parameters is that of shifting the oscillation minimum and changing its depth, despite inserting very fast un-observable oscillations. By studying this oscillation channel is also possible to constrain θ_{34}, which is in principle one of the most difficult mixing parameter to limit, due to the lack of ν_τ beams.

The IceCube Collaboration reported an analysis focused on events with energy around 20 GeV. The corresponding upper limits they obtained, at 99% CL, are shown in Figure 1.14. Also the Super-Kamiokande Collaboration reported exclusion limits for the two mixing angles, and the results at 99% CL are shown as well in Figure 1.14.

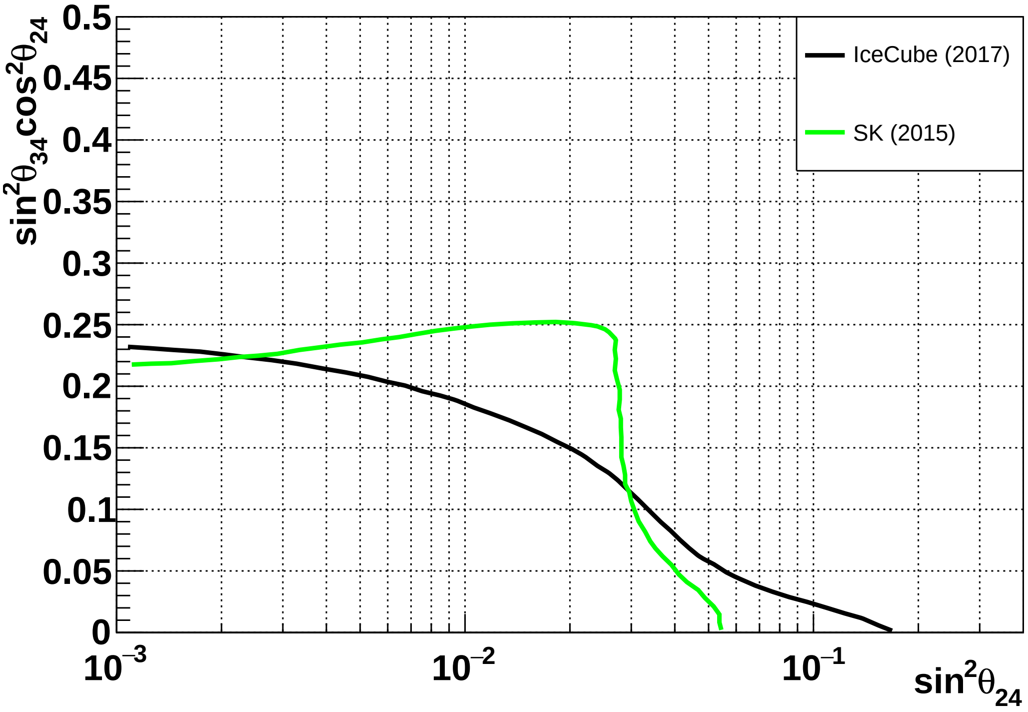

Figure 1.14: IceCube (black) and Super-Kamiokande (green) limits on $|U_{\mu 4}|^2 = \sin^2\theta_{24}$ and $|U_{\tau 4}|^2 = \sin^2\theta_{34}\cos^2\theta_{24}$ at 99% CL. For details, see [66] and [67], respectively.

The second method uses higher neutrino energies and is also sensitive to Δm^2_{41}. This can be seen in Figure 1.15, where the survival probability of a vertically up-going atmospheric $\bar{\nu}_\mu$ is illustrated, as a function of its energy.

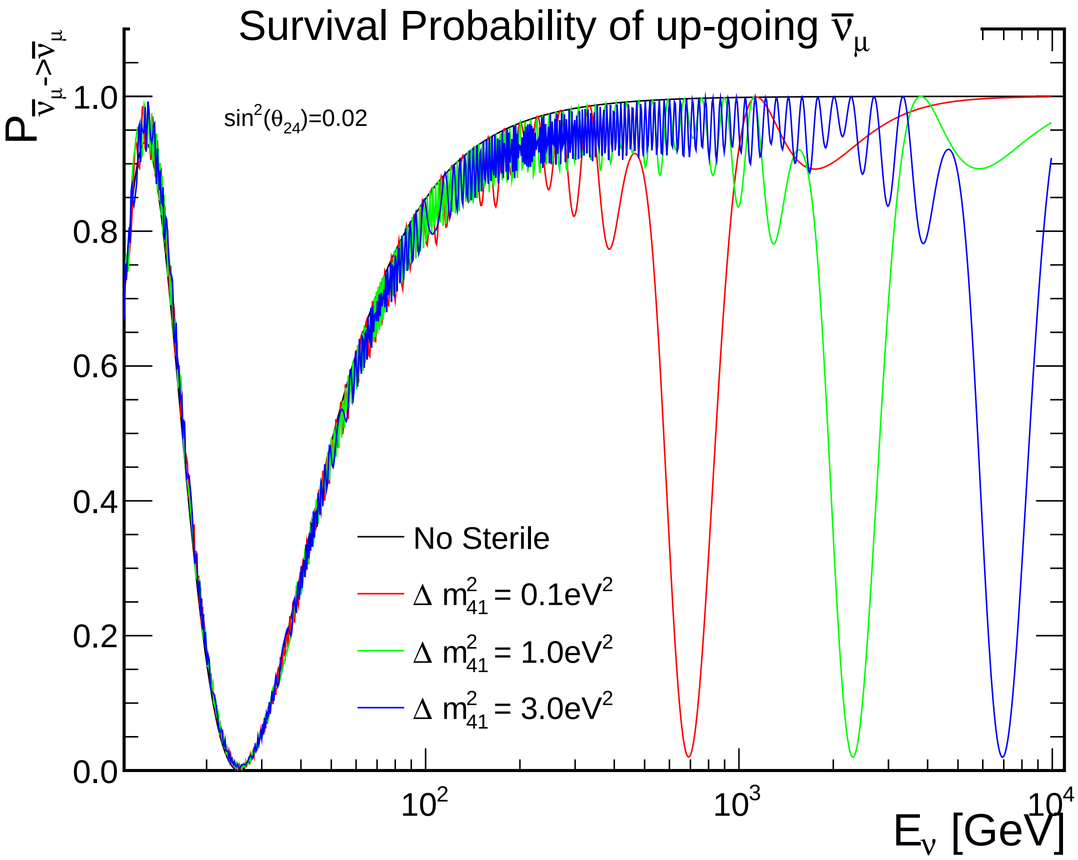

Figure 1.15: Survival probability for a vertically up-going $\overline{\nu}_\mu$ assuming different values of Δm^2_{41}.

As the value of Δm^2_{41} increases a new oscillation minimum appears for higher neutrino energies. Despite the smallness of θ_{24}, $P_{\overline{\nu}_\mu \to \overline{\nu}_\mu}$ decreases almost to zero due to a matter resonance effect at Δm^2_{41} in the Earth mantle. Fast oscillations are, instead, introduced by the non zero value of θ_{24}.

The IceCube Collaboration reported limits on these two parameters, by studying events in the TeV energy range. Results are shown in Figure 1.16, together with the ones by MINOS [68], which looked at the same oscillation channel trough an accelerator-based experiment.

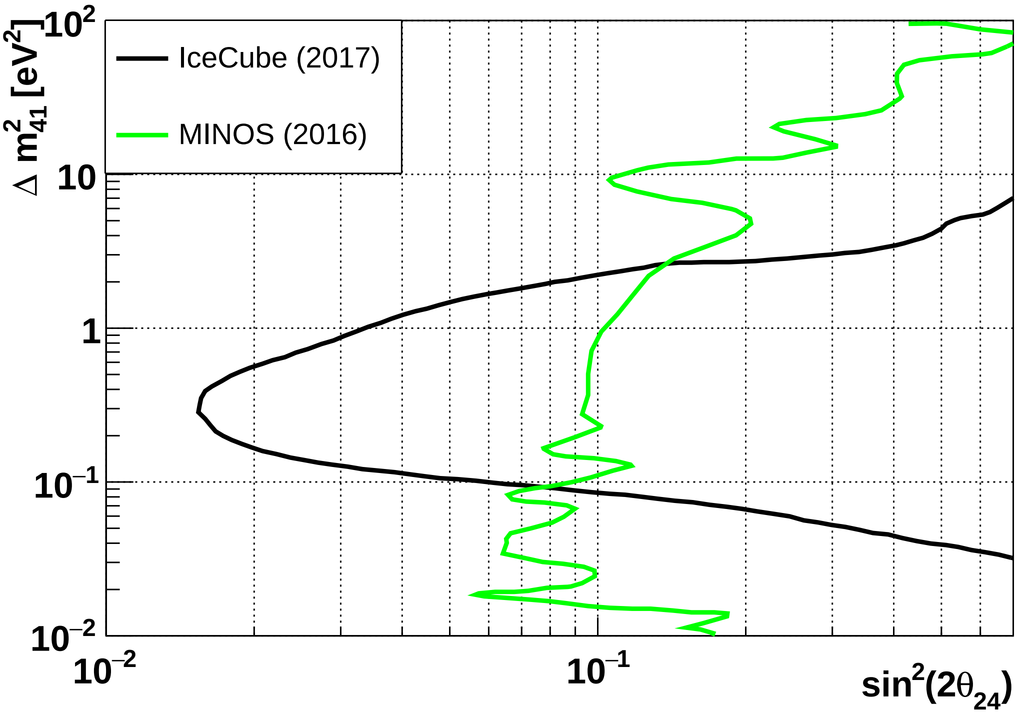

Figure 1.16: IceCube (black) and MINOS (green) 90% CL limits on $\sin^2(2\theta_{24})$ and Δm^2_{41}. For details, see [69] and [68], respectively.

In Chapter 7, an analysis aimed to constrain the values of θ_{24} and θ_{34} with ANTARES data will be presented. The potential for ANTARES to constrain the parameter space of Δm^2_{41} and θ_{24} using more energetic events will be discussed as well.

1.5.4 ν_e and $\bar{\nu}_e$ appearance

Accelerator neutrino experiments could also exploit the $\nu_e/\overline{\nu}_e$ appearance starting from a beam of $\nu_\mu/\overline{\nu}_\mu$. The Liquid Scintillator Neutrino Detector (LSND), an accelerator neutrino experiment which ran at Los Alamos LAMPF accelerator National Laboratory from 1993 and 1998, reported an excess of $\overline{\nu}_e$ from a $\overline{\nu}_\mu$ beam [70], which could be explained in the 3+1 scenario. Confirmations as well as retractions for such observations were found by different collaborations. A recent result, presented at *Neutrino 2018*, from the MiniBooNE Collaboration [71] showed a 4.8σ evidence for sterile neutrino. The observed events excess are consistent with neutrino oscillations with $\Delta m^2_{41} > 0.1\,\mathrm{eV}^2$.

In Figure 1.17 the most recent allowed regions by the MiniBooNE analysis are shown, together with the ones from LSND and other collaborations. The mixing angle shown in the figure, $\theta_{\mu e}$, is defined as:

$$\sin^2(2\theta_{\mu e}) \equiv 4|U_{e4}|^2|U_{\mu 4}|^2 \tag{1.32}$$

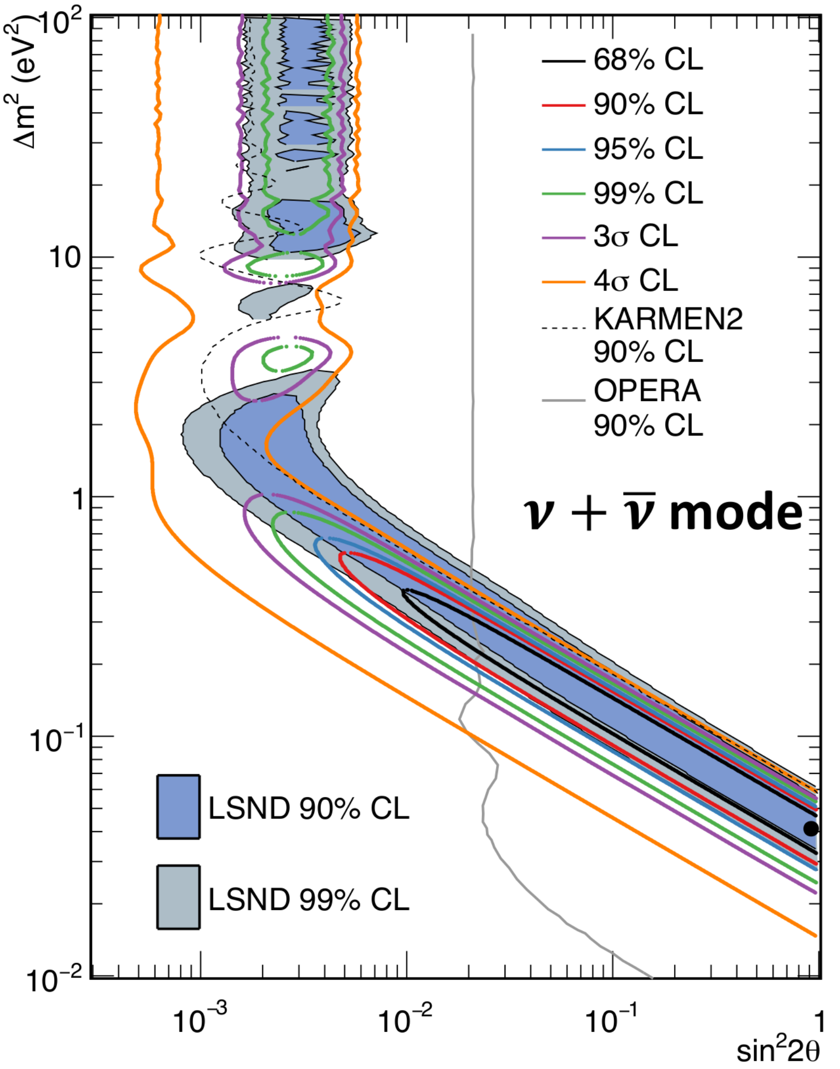

Figure 1.17: MiniBooNE allowed regions in the parameter space of $\sin^2(2\theta_{\mu e})$ and Δm^2_{41}, together with the results by other collaborations [71].

Both $|U_{e4}|^2$ and $|U_{\mu 4}|^2$ are required to have non-zero values to explain the anomalies. This produces considerable tensions to the limits in the ν_e and ν_μ disappearance channels.

1.6 Open questions

In this Section the main remaining open questions in Neutrino Physics will be discussed, starting from the neutrino mass ordering issue, passing through the determination of the CP-violating phase, the Majorana or Dirac nature of neutrinos, to the absolute neutrino mass scale. The experimental setups which are trying or are planning to answer these questions will be briefly described as well.

1.6.1 Neutrino mass ordering

As seen in 1.4.4 solar oscillation neutrino experiments have not only constrained the absolute value of the mass splitting Δm^2_{21}, but also determined its sign. On the other hand, the sign of the remaining independent Δm^2_{32} has still to be measured. This ambiguity is known as the *neutrino mass hierarchy* (NMH) problem. The two possible scenarios are illustrated in Figure 1.18: in the *normal* mass ordering the mass eigenstate with the minor component of electron neutrino, ν_3, is the heaviest, while, in the *inverted* mass ordering it is the lightest.

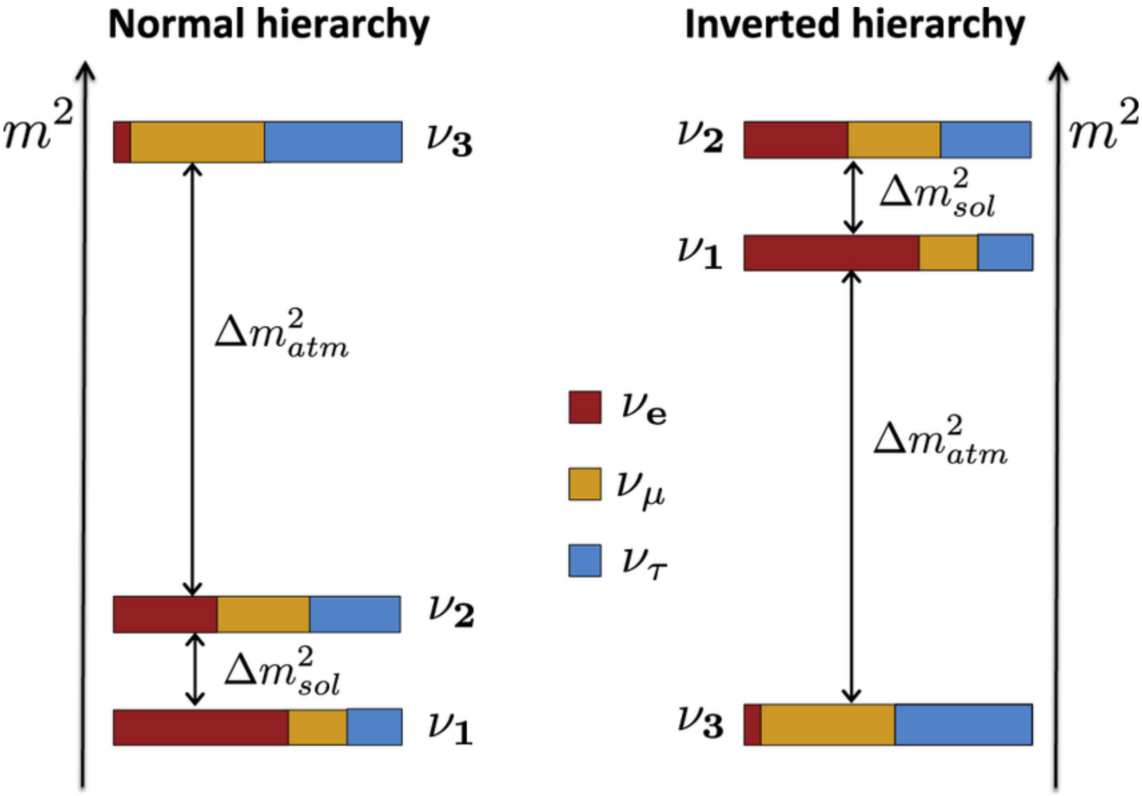

Figure 1.18: Scheme of the two distinct neutrino mass hierarchies. The colour code indicates the fraction of each flavour (e, μ, τ) present in each of the mass eigenstates (ν_1, ν_2, ν_3) [53].

From a theoretical point of view, the determination of the NMH would constrain the models that seek to explain the origin of mass in the leptonic sector as well as the differences within the mass spectrum of all elementary particles [72]. Moreover, from the experimental prospective, the NMH could affect the performances of the future experiments looking for the determination of the CP-violating phase, the neutrino absolute masses and their Dirac or Majorana nature (see further Subsections for details). Furthermore, the value of the other mixing parameters also depends on the NMH (see Table 1.1).

The main experimental technique to determine the neutrino mass hierarchy is to exploit the matter effects on long enough baselines. This can be done both through accelerator-based experiments and atmospheric neutrino experiments. The former, such as NOνA [73], T2K [74] and DUNE [75], focus mainly on the ν_e appearance channel; the latter, such as PINGU [52] and ORCA [53], exploit in addition also the

ν_μ survival channel.

For atmospheric neutrinos, which are studied by PINGU and ORCA, the resonance condition due to matter effects will appear for energies around 3 GeV for those passing trough the Earth core, while in the mantle the resonance is reached at energies of 6-7 GeV. Even though to first order, the effect for neutrinos in the NH scheme is the same as for anti-neutrinos in the IH scheme, thanks to the difference (around a factor 2) in the neutrino and anti-neutrino cross section in the energy range of interest, a net asymmetry in the combined event rates between NH and IH for a given flavour can be observed.

Recent global fits show a preference towards the *normal* mass hierarchy [76]. However, additional data are required in order to obtain a higher significance. In Figure 1.19 the expected median sensitivity in discarding the wrong mass ordering, after three years of data taking, with the KM3NeT/ORCA detector is shown as a function of the true value of θ_{23}.

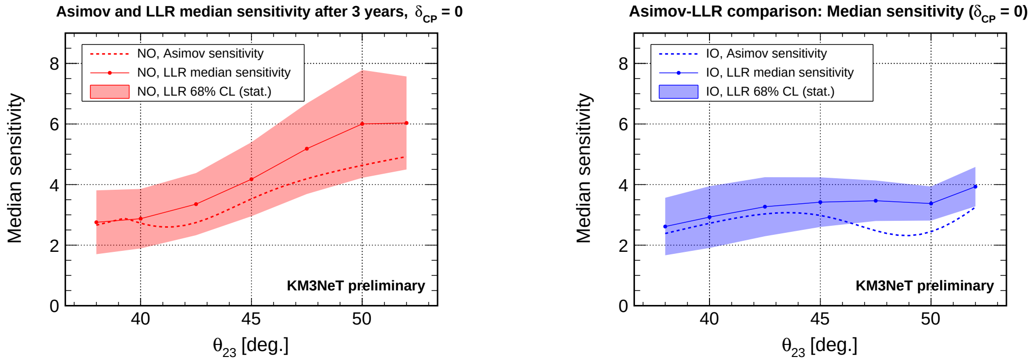

Figure 1.19: Expected median sensitivity of the KM3NeT/ORCA detector after 3 years of data taking in discarding the wrong mass ordering, as a function of the true value of θ_{23}. Two different methods have been tested, namely an Asimov test approach and a log-likelihood ratio (LLR) [77].

1.6.2 CP-violating phase

Among all the standard neutrino mixing parameters, the CP-violating phase, δ_{CP}, is the only one still unknown. The CP transformation converts a left-handed neutrino into a right-handed anti-neutrino, acting as a particle-antiparticle transformation. This means that CP-violation could help explaining the asymmetry between matter and antimatter in the Universe. Conservation of CP would mean that the oscillation probability for neutrino and anti-neutrino has to be the same:

$$P_{\nu_\alpha->\nu_\beta} = P_{\bar{\nu}_\alpha->\bar{\nu}_\beta} \tag{1.33}$$

A violation of CP would cause a non-zero asymmetry in the appearance oscillation probabilities of neutrinos and anti-neutrinos, which can be defined as:

$$A_{CP} = P_{\nu_\alpha->\nu_\beta} - P_{\bar{\nu}_\alpha->\bar{\nu}_\beta}, \qquad \alpha \neq \beta = e, \mu, \tau \tag{1.34}$$

In the standard 3-flavour picture, assuming vacuum oscillations, one gets [78]:

$$A_{CP}^{(e,\mu)} = A_{CP}^{(\mu,\tau)} = A_{CP}^{(\tau,e)} = J_{CP} F_{vac}^{osc} \tag{1.35}$$

with:

$$J_{CP} = \frac{1}{8} \sin(2\theta_{12}) \sin(2\theta_{23}) \sin(2\theta_{13}) \cos\theta_{13} \sin\delta_{CP} \tag{1.36}$$

$$F_{vac}^{osc} = \sin(\frac{\Delta m_{21}^2}{2E} L) + \sin(\frac{\Delta m_{32}^2}{2E} L) + \sin(\frac{\Delta m_{13}^2}{2E} L) \tag{1.37}$$

If any of the mixing angles were equal to zero or 90°, J_{CP} would vanish. That is why, the determination of δ_{CP} has become one of the most important goals in this field after the discovery of the non-zero value of θ_{13}. Furthermore, since the relation $\Delta m_{12}^2 + \Delta m_{23}^2 + \Delta m_{31}^2 =$ holds, even if any of the mass splitting were zero, the CP asymmetry would vanish.

Equations 1.36- 1.37 are satisfied only in case of oscillations in vacuum. However, we know that the majority of neutrino oscillation experiments have to deal with oscillations trough matter. Since matter effects are not CP invariant, this induces an additional "fake" CP-violating term into the oscillation probabilities (see 1.4.3), which could result in ambiguities when trying to determine δ_{CP} and the neutrino mass ordering in the same experiment [79]. Figure 1.20 illustrates the degenerate cases that can arise from the interference of the matter and CP asymmetries.

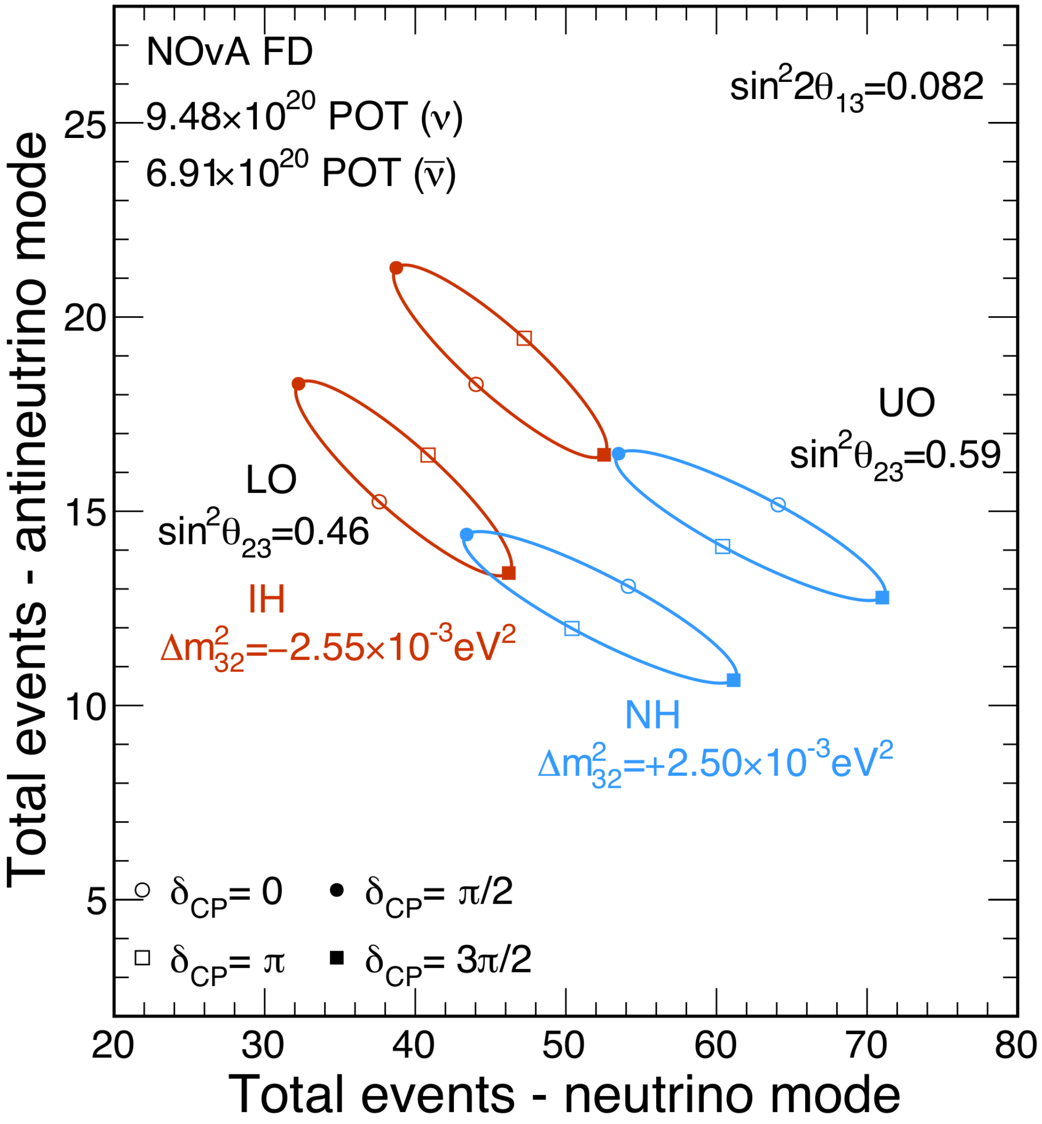

Figure 1.20: Expeced number of events in ν and $\bar{\nu}$ mode at the NOνA far detector, assuming both normal and inverted mass ordering (blue and red ellipses), θ_{23} in the lower and in the upper octant, and for different true values of δ_{CP} [49].

At the NOνA baseline ($\sim$ 810 km) the degeneracy is maximal between normal mass ordering and $\delta_{CP} = \pi/2$ versus inverted hierarchy and $\delta_{CP} = 3\pi/2$.

The T2K Collaboration recently reported the first indication of a non-zero value of δ_{CP} [80], and, combining their results with the ones from reactor experiments, the hypothesis of CP conservation is excluded at the 90% confidence level. Several experimental setups are under study in order to constrain even more the value of δ_{CP} and confirm whether there are hints for CP violation in the neutrino sector. Among these, the potential of DUNE and T2HK has been studied [81] and it is shown in Figure 1.21.

The potential for the determination of δ_{CP} has recently been investigated also by the KM3NeT Collaboration [82], which studied the possibility of sending a neutrino beam from the accelerator complex in Protvino (Russia) to ORCA.

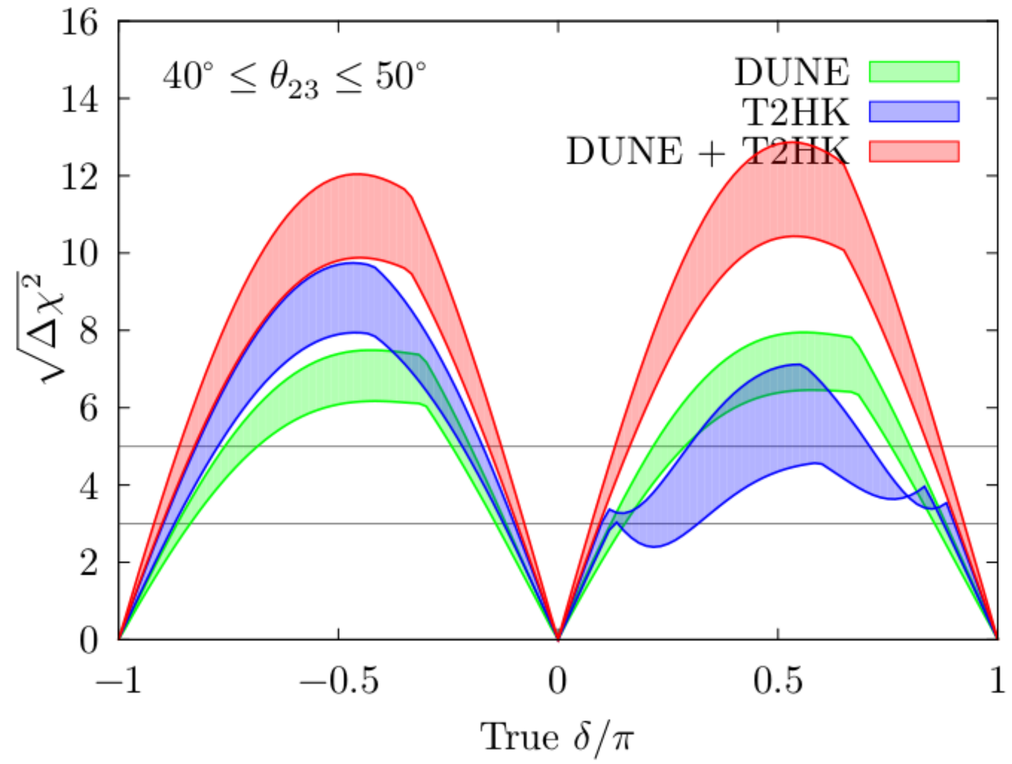

Figure 1.21: The expected sensitivity to CP violation for DUNE and T2HK and their combined potential, as a function of the true value of δ_{CP}. The considered lifetime is of 10 years both for DUNE and T2HK (5 years in ν mode plus 5 years in $\bar{\nu}$ mode for DUNE, and 2.5 years plus 7.5 years for T2HK) [81].

1.6.3 Majorana or Dirac neutrinos?

Once the non-zero mass of neutrinos had been established by the discovery of neutrino oscillations, a new question arose, namely whether they are Dirac or Majorana particles. The first case foresees that neutrino and anti-neutrino are two distinct particles, while the second one assumes they are actually the same particle, implying the violation of lepton number conservation during interactions. The observation of lepton number violation in the neutrino sector would have important consequences for our understanding of Particle Physics, and could explain the matter-antimatter asymmetry in the Universe, together with CP-violation.

Experimentally, the Majorana nature of neutrinos could be confirmed by observing a neutrinoless double β-decay ($0\nu\beta\beta$). Indeed, if neutrinos were Majorana particles, the process in which the neutrino emitted at one β-decay vertex is absorbed at the second decay vertex as an anti-neutrino would be possible.

The search for $0\nu\beta\beta$ evidence spreads over many isotopes and different detection techniques. The $2\nu\beta\beta$, which does not violate any known conservation law, has been observed for several nuclei, which represent then potential candidates for $0\nu\beta\beta$. Depending on the chosen isotope, different challenges in terms of background rejection, energy resolution and detection efficiency have to be addressed. Even though it has not been observed yet, the collected data have allowed to infer limits on the half-life time of the process as well as on the related mass, $m_{\beta\beta}$:

$$m_{\beta\beta}^2 = |\sum_i U_{ei}^2 m_i|^2 \tag{1.38}$$

Among the various isotopes, ^{136}Xe, ^{76}Ge and ^{130}Te are the most used for this kind of experiment [83]. The first one is well suited thanks to the low radioactive background contamination in the region of interest; the advantage of Germanium, instead, is the possibility to be embedded in solid state detectors, allowing to use a calorimetric approach; the strength of ^{130}Te is its natural abundance compared to the other two elements.

Two experiments have looked for $0\nu\beta\beta$ in ^{136}Xe: EXO-200 [84] and KamLAND-Zen [85]; GERDA [86] in Europe, and MAJORANA [87] in the USA are employing the Germanium technology; CUORE [88] is instead using ^{130}Te as source. Among these experiments, GERDA recently reported, at the 90% CL, a lower limit for the half-life time of 1.1×10^{26} yr, which corresponds to a $m_{\beta\beta} < 0.2\,\text{eV}$ [89].

1.6.4 Absolute neutrino mass

As seen in 1.4, neutrino oscillation probabilities depend on the difference between the square of the mass eigenstates, but are not sensitive to the absolute value of the neutrino masses. Knowing the absolute value of the neutrino masses would help in testing the models for mass generation within the Standard Model, but also in understanding the composition of the energy density of the Universe [90].

Since neutrino oscillation experiments constrain the mass splitting $\Delta m_{i,j}^2$, it would be sufficient to measure the absolute mass of one neutrino flavour.

Neutrinoless double β-decay can be used to measure the absolute neutrino mass. However, this process is only possible if neutrinos were Majorana particles. Furthermore, strong cancellations in the terms of Equation 1.38 are possible due to the unknown Majorana phases.

Direct investigation techniques, instead, which make use of the energy and momentum conservation laws and on their relation, do not rely on any assumption on the nature of neutrinos. The observable in this kind of experiments can be expressed as:

$$m_{ee} = \sum_i |U_{ei}|^2 m_i \tag{1.39}$$

where it is evident that no cancellation due to phases can occur.

If a very large distance between the source and the detector is available, the measurement of the neutrino time of flight can be used to set upper limit on neutrino masses. In this way, studying the detected neutrinos from the supernova $SN1987A$, a limit of 23 eV has been put to the electron neutrino mass, m_{ν_e} [91]. Measuring the charged decay products of weak decays, upper limits have been inferred also on the masses of the other neutrino flavours [92, 93]. Limits on m_{ν_e} can be inferred also by single β-decay experiments, studying the tails of the electron energy spectrum. The most sensitive element to be used for such direct searches up to now is the Tritium, ^3H. In Figure 1.22 the electron energy spectrum of ^3H β-decay is shown, together with a zoom in the region of interest, both for the case of $m_{\nu_e} = 0\,\text{eV}$ and $m_{\nu_e} = 1\,\text{eV}$.

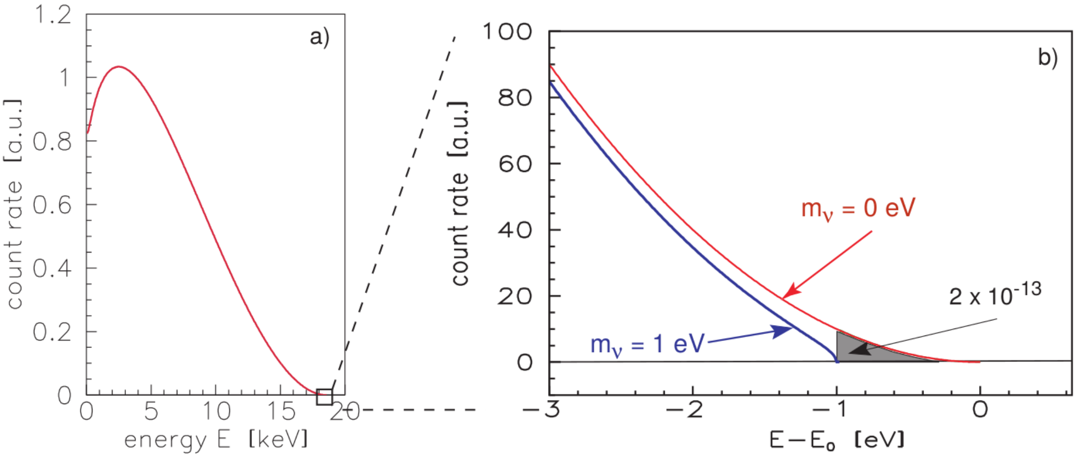

Figure 1.22: The electron energy spectrum of Tritium β-decay: complete (a) and narrow region around the endpoint E_0 (b). The β spectrum is shown for neutrino masses of 0 and 1 eV [94].

As can be seen in the figure, the challenge of this kind of experiments relies on the fact that only a very small region close to the spectrum endpoint ($E = E_0$) shows a statistically significant distortion between the two cases. Since the fraction of β-decays in this region is proportional to $1/E_0$, the Tritium represents a very good candidate thanks to its low endpoint energy of 18.6 keV. On the other hand, a huge luminosity and a high energy resolution are required. The current limits are $m_{\nu_e} < 3\,\text{eV}^2$.

KATRIN [94] is a Tritium β-decay experiment designed to reach a sub-eV precision in the determination of m_{ν_e}. Data taking has started in May 2018, and preliminary results of the commissioning phase have been presented, showing the stability and functioning of the whole apparatus [95].

Cosmological observations provide a measurement of the sum of all the neutrino mass eigenstates, $\sum_i m_{\nu_i}$, independently from the mixing parameters [90]. The Standard Cosmological Model depends on several parameters, among which the neutrino density, Ω_ν:

$$\Omega_\nu h^2 = \frac{\sum_i m_{\nu_i}}{93.2eV} \tag{1.40}$$

where h is the Hubble parameter in units of 100 km/s/Mpc. The galaxy-galaxy power spectrum from Large Scale Structure (LSS) survey is the most used measurement to access matter distributions. In order to avoid degeneracies among the cosmological parameters, the LSS data are usually combined with data from the Cosmic Microwave Background (CMB). Limits of the order of sub-eV are obtained in this way [96] ($\sum_i m_{\nu_i} < 0.17\,\mathrm{eV}$ at 95% CL).

Chapter 2

The ANTARES neutrino telescope

In this Chapter the ANTARES neutrino telescope is described. First the detection principle, based on the Cherenkov radiation mechanism is presented; the detector layout is illustrated, together with the data acquisition, the monitoring and the trigger systems. Since part of this thesis work has been focused on the determination of the ANTARES optical modules photon detection efficiency (see Chapter 3), a particular attention is paid to the characterization of these important detector components. The main aspects of the ANTARES physics program are also described.

2.1 The detection principle

The detection principle of ANTARES is based on the Cherenkov radiation mechanism. Relativistic particles, which travel in a medium faster than the light, emit radiation, in an analogous way to the shock wave produced by a plane moving faster than the speed of sound. This phenomenon was first observed by Pierre and Marie Curie in the early XX Century, even though no further investigation was taken at that time, while the experimental evidence as well as the theoretical explanation of the effect was possible thanks to the work of P. Cherenkov, I. Frank and I. Tamm, who were awarded the Nobel Prize in 1958 [97].

The emitted Cherenkov radiation follows a cone, whose opening angle is described by the Equation:

$$\cos\theta = \frac{1}{n\beta} \tag{2.1}$$

where θ is the opening angle, n is the refractive index of the medium, and β is the ratio between the velocity of the particle and the speed of light. A representation of a particle emitting Cherenkov radiation is shown in Figure 2.1.

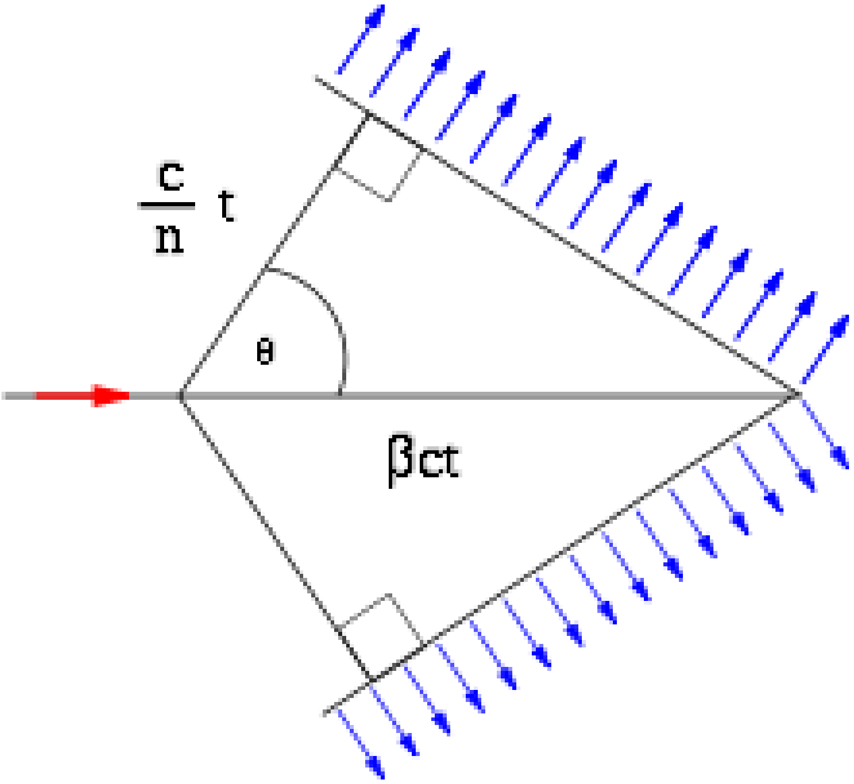

Figure 2.1: Schematic representation of a particle emitting Cherenkov radiation [98].

When a neutrino interacts with a particle in sea water, it produces secondary relativistic charged particles, which in turn emit Cherenkov radiation. This is the actual signal which is recorded by the ANTARES optical modules.

2.2 The ANTARES detector

The ANTARES (Astronomy with a Neutrino Telescope and Abyss environmental RESearch) neutrino telescope [99] is located 40 km off the coast of Toulon (France), at a depth of 2475 m. It was completed on 29 May 2008, and it constitutes the largest neutrino telescope in the northern hemisphere and the first to operate in the deep sea.

The detector is composed of 12 lines; in its nominal configuration, a line is formed by a chain of 25 Optical Module Frames (OMFs) linked with Electro-Mechanical Cable segments (EMC). Each OMF supports three optical modules (OMs) and a titanium container, the Local Control Module (LCM), which hosts the offshore electronics. The group of three OMs is generally called a *storey*. The distance between each OMF is 14.5 m and the one from the seabed to the first OMF is 100 m. ANTARES comprises 11 lines in the nominal configuration and a twelfth being equipped with 20 OMFs and completed with devices dedicated to acoustic detection. The lines are arranged in the seabed in an octagonal shape, at a distance of 60-75 m among them. An additional Instrumentation Line, IL07, is equipped with instruments devoted to environmental measurements. A schematic representation of the ANTARES layout is shown in Figure 2.2.

The data communication and the power distribution to the lines are done via an infrastructure on the seabed, which consists of Inter Link cables (IL), a Junction Box (JB) and the Main Electro-Optical Cable (MEOC). In order to minimize the number of single point failures for a full line, each line is divided in 5 sectors of 5 storeys; the sectors are independent from the point of view of power distribution and data transmission.

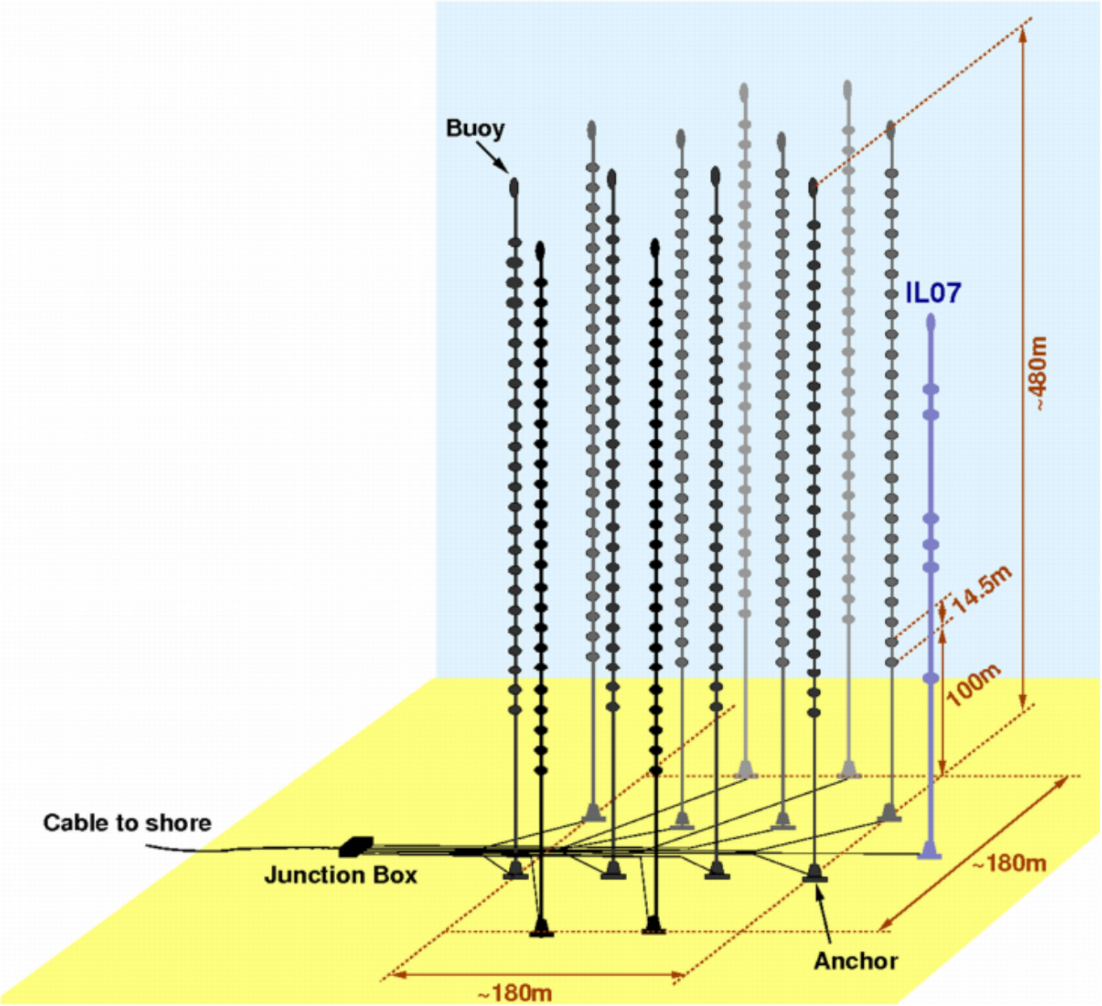

Figure 2.2: Schematic representation of the ANTARES layout [99].

2.2.1 The ANTARES optical module

The key ANTARES detection element is the optical module (OM), which hosts a photomultiplier tube (PMT) in a pressure resistant glass sphere (see Figure 2.3). In order to obtain a highly sensitive light detector, the PMT should provide a large photocathode area combined with a large angular acceptance. Following these criteria, the best candidates are large hemispherical tubes. In the R&D phase several tests were performed on different available PMT models. The R7081-20, 10" hemispherical tube from Hamamatsu [100] was chosen. The glass sphere which protects the PMT is made of two hemispheres: the "back hemisphere", which is painted in black and has two drilled holes through which electrical connection is provided via a penetrator and a vacuum port; and the "front hemisphere", which is transparent and houses the PMT, which is kept in position by an optical gel. A magnetic shield is implemented through a grid made of wires of $\mu-$metal which surrounds the PMT bulb. A blue LED is glued on the rear part of the bulb and is used for internal time calibration of the OM. Each PMT points 45° downward.

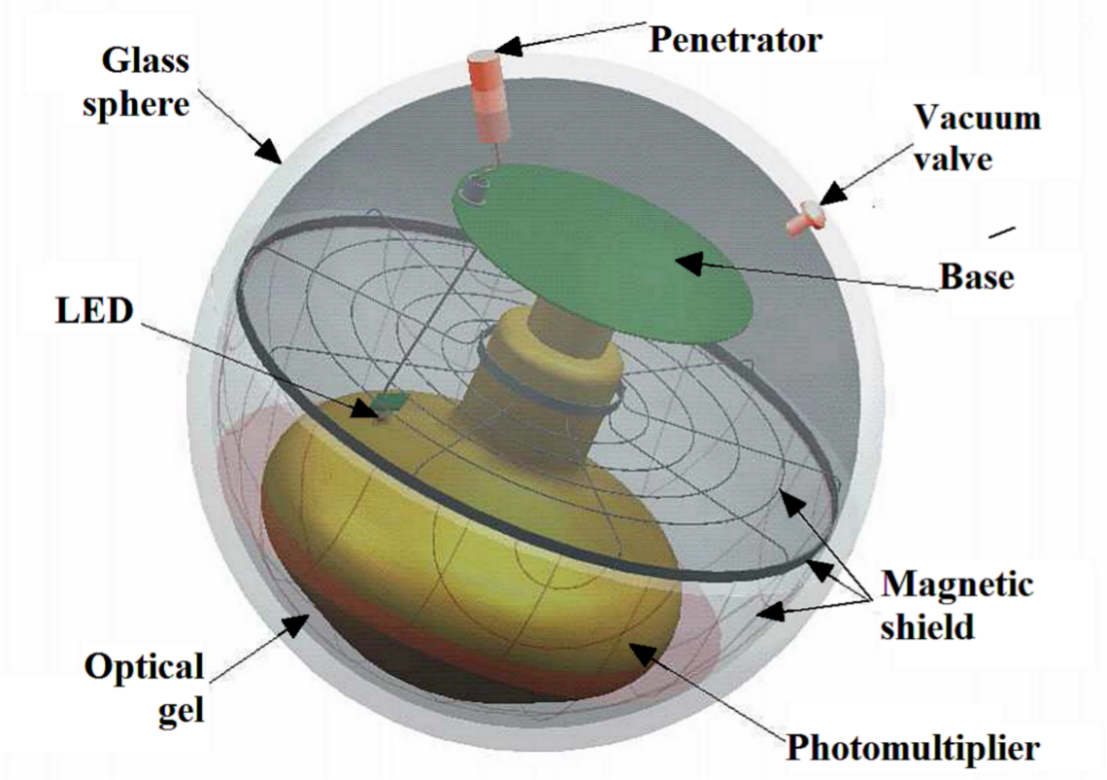

Figure 2.3: Schematic representation of an ANTARES OM [99].

2.2.2 Data acquisition and monitoring systems

The ANTARES Data Acquisition system (DAQ) is based on the "all-data-to-shore" concept, which means all signals recorded from the PMTs that pass a given threshold (typically 0.3 Single Photo Electrons) are digitized and sent to shore. The set of digitized timestamp, amplitude and reference to the PMT which has recorded the signal constitutes a *hit*.

In order to get an angular resolution better than 0.3° for neutrinos of energies above 10 TeV, a timing resolution of the order of 1 ns is required. To achieve such precision a 20 MHz master clock system, based onshore, delivers a common reference time to all the offshore electronics, via a network of optical fibers. Further calibration is needed for the time delay between the electronics in the LCM and the photon arrival time at the PMT photocathode. These time calibrations were performed during the detector construction and are continually kept under control on a weekly basis [101]. Two systems of external light sources are used: LED beacons located in four positions on each detector line, and laser beacons located at the bottom of several lines. ^{40}K decays in sea water are used to complete the time calibration of the detector (see Chapter 3).

Another important ingredient in order to ensure optimal event reconstruction accuracy is the knowledge of the relative positions of all the OMs, as well as their orientation. The detector lines, in fact, are flexible and are continuously floating in the sea current. Two independent systems are used to monitor these parameters: a High Frequency Long Base Line acoustic system (HFLBL) gives the position of the hydrophones placed along the lines; while a set of tiltmeter-compass sensors gives the local tilt angles of each storey with respect to the vertical line and to the Earth magnetic North.

2.2.3 Trigger system

Not all the data sent to shore can be saved for further analysis. Due to bioluminescence and ^{40}K decays, each ANTARES PMT has an average counting rate of 50 kHz, which generates a total output of 4 TB per day. For this reason, a trigger system has been developed, in order to select only *interesting* events and save them for later studies.

The basic concept of the trigger system is the search for correlated signals, such as those coming from a muon; thus the employment of coincidences and cluster algorithms allows to distinguish the signals from random background. In particular, coincidences refer to time correlated hits nearby, while cluster algorithms identify groups of hits anywhere in the detector that fulfill a causality relation.

The ANTARES trigger system is implemented on multiple levels. As first step, each raw hit is calibrated and is referred to as *L0* hit. If two *L0* hits have been recorded on the same storey within a time window of 20 ns, then they constitute an *L1* hit. The next level consists in looking for coincidences of *L1* hits between different storeys on the same detection line. This stage is called the *T*-level; thus, for instance, a *T2* hit is defined as two *L1* hits recorded in adjacent floors within a time window of 100 ns, while a *T3* hit is defined by two *L1* hits in adjacent floors or next-to-adjacent floors within 200 ns. Figure 2.4 illustrates some examples of triggered hits.

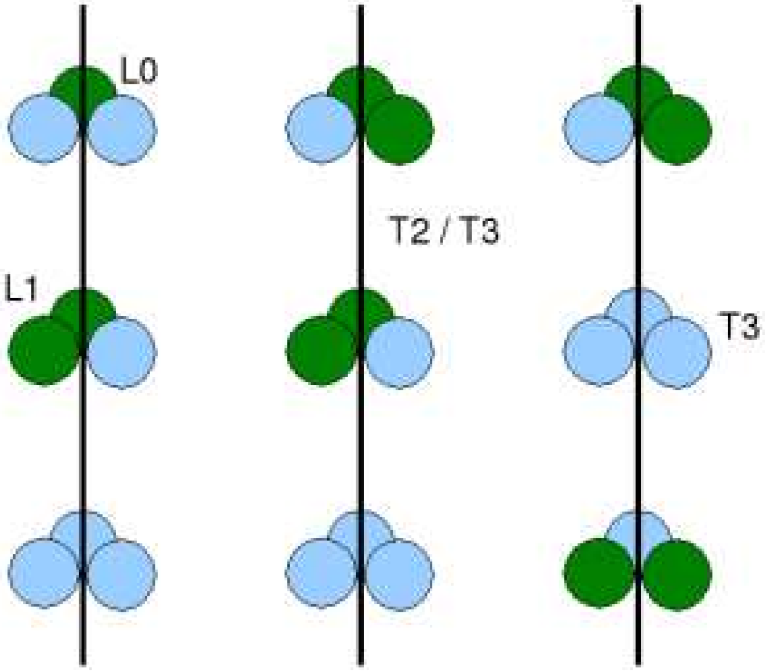

Figure 2.4: Schematic representation of some ANTARES tirggered hits. Each vertical line represents a detection line, while the three spheres stand for the three OMs in each floor [102].

When a trigger condition is satisfied all *L0* hits in a time window of several μsec around the trigger time are stored for late analysis steps.

2.3 Doing physics with ANTARES

ANTARES has been optimized for the detection of high energy neutrinos. Its main goal is to detect galactic and extra galactic neutrinos, in order to shed light on the origin of cosmic rays and the mechanisms of their sources. However, in its more than ten years of operation, ANTARES has given the possibility to study a variety of phenomena, not only in Astroparticle Physics, making it an actual multi-disciplinary experiment. In the following subsections the main achievements of ANTARES are described.

2.3.1 Searches for cosmic rays sources

After the discovery of cosmic rays (see Chapter 1), several efforts have been made by different scientific collaborations to find the sources behind this phenomenon, as well as to understand their acceleration mechanism. As we have already discussed, due to their weak interaction nature, cosmic neutrinos are very good probes to determine the position of these sources in the sky.

Several analyses have been performed with ANTARES data, looking for different kind of possible cosmic rays sources. Looking at the expected cosmic rays interactions in the galactic plane, one can constrain the flux of cosmic neutrinos [103]. Point-like cosmic neutrino sources located in the southern hemisphere can be investigated thanks to the very good angular resolution achievable in sea water and, when no source is found, limits on the expected neutrino flux from that particular location can still be inferred [104]. While the neutrino flux from a single source might be too low to be detected, the existence of many faint sources would result in a diffuse neutrino flux. The observation of a diffuse flux of ultra high energy cosmic rays can be used to set theoretical upper bounds on the total flux of neutrinos from extra-galactic sources [105, 103].

Transient sources as gamma-ray bursts (GRBs), active galactic nuclei (AGN) or core-collapse supernovae (CCSNe), are promising candidates for the production of high energy cosmic rays and neutrinos. They emit in multi-wavelengths spectra and, for this reason, in order to enhance the sensitivity to their detection, a method based on multi-wavelength follow-up of neutrino alerts has been developed within the ANTARES Collaboration [106]. This program, called TAToO, triggers a network of robotic optical telescopes and the Swift-XRT, which start observing the corresponding region of the sky looking for possible electromagnetic counterpart when a neutrino candidate has been observed.

On the other hand, real-time searches for ANTARES neutrino candidates coincident with gamma-ray bursts, High-Energy Starting Events and Extremely High-Energy Events detected by IceCube and gravitational wave candidates observed by LIGO/Virgo are performed [107].

2.3.2 Dark matter and magnetic monopoles

Nowadays it is generally accepted by the astrophysical community that the majority of matter in our Universe is constituted by non-luminous *dark matter*. The clearest indirect evidence of the dark matter existence is that galaxies are rotating with such a high speed that the gravity generated by the observable matter they are made of could not possibly hold them together; it must exist additional matter which prevent them to be torn apart. Dark matter does not interact trough the electromagnetic force, which means it does not absorb, reflect or emit light, making it extremely difficult to detect. No presently known particle has the properties to represent a dark matter particle candidate, but some *supersymmetric particles*, hypothesized particles that are partners to those already known in the Standard Model, could in principle be such candidates.

Neutrino telescopes are not directly sensitive to *supersymmetric particles*. However, these particles are expected to accumulate in the cores of the Sun and the Earth or in the center of the Galaxy through gravitational capture. This would result in an increase of their density and in subsequent annihilation reactions, producing also high-energy neutrinos. ANTARES is sensitive to these neutrinos over a wide range of hypothetical *supersymmetric particle* masses. Several studies have been published and limits on these particles masses have been inferred. For the most recent results see [108] and [109].

Search for magnetic monopoles are also possible with the ANTARES neutrino telescope. So far, no indication for such particles has been found, but limits on their flux are inferred [110].

2.3.3 Neutrino oscillations

At energies below 100 GeV, atmospheric neutrino oscillations can be studied through the distortion of the energy and angular spectra of up-going events. For a vertically up-going muon neutrino, the first oscillation peak is reached at energies of around 24 GeV, which is still detectable by ANTARES, whose threshold is at around 20 GeV.

The study of atmospheric neutrino oscillations is the main topic of this thesis, therefore a dedicated Chapter will be presented.

2.3.4 Environment and Earth science

ANTARES provides an important site to study and monitor the deep-sea environment. The majority of the oceanographic instruments on the seafloor are not connected to the surface, but they run on batteries and store data locally, allowing to access them only after their recovery. An experimental setup as ANTARES provides, instead, real-time data acquisition, together with the possibility to interact and monitor directly the sensors. Several programs benefit from the ANTARES instrumentation site: from bioluminescence studies to the characterization of acoustic signals from marine mammals, up to real-time seismic and tsunami alerts. For more details on these subjects, see [111].

Chapter 3

Long-term monitoring of the ANTARES optical modules efficiency using ^{40}K decays in sea water

In this Chapter the determination of the ANTARES optical modules photon detection efficiency through ^{40}K decays in sea water is described. This work has been an important part of the thesis project and the results are currently used as input for the most up-to-date ANTARES Monte Carlo (MC) production (see Chapter 4).

Using the data collected by the ANTARES neutrino telescope from mid 2008 to 2017, the optical modules (OMs) efficiency has been determined through the so called ^{40}K method. The results have been computed after applying selection cuts in order to provide reliable time-dependent OM efficiencies for most of the individual OMs. The ^{40}K method provides as well an integral part of the intra-storey time calibration of the detector.

In the following sections, after a brief introduction, the ^{40}K method is described, together with all the analysis steps. The treatment of statistical and systematic uncertainties is presented as well. A description of the ^{40}K method as part of the overall detector time calibration is explained and a final study on the dependence of the OM efficiencies on the position in water is presented.

3.1 ^{40}K decay rate at the ANTARES site

The decay products of radioactive elements dissolved in sea water constitute the principal source of background light for deep-sea neutrino telescopes. Among these isotopes, potassium-40 (^{40}K) is the most abundant. Other radioactive decays (mainly from the U/Th chain) induce Cherenkov photons on the permille level compared to ^{40}K decays and can be neglected. This process constitutes an important calibration tool as well. If a ^{40}K nucleus decays near a storey, the resulting Cherenkov light can be recorded by two OMs almost simultaneously. Such coincidences are used to derive the relative photon detection efficiencies [112] and for time calibration between OMs in the storey.

The main decay channels of ^{40}K are:

$$^{40}\mathrm{K} \rightarrow \ ^{40}\mathrm{Ca} + e^- + \overline{\nu}_e \qquad\qquad (89.3\%)$$

$$\begin{array}{ll} ^{40}\mathrm{K} + e^- \rightarrow \ ^{40}\mathrm{Ar}^* + \nu_e & \qquad (10.7\%) \\ \qquad\qquad \hookrightarrow \ ^{40}\mathrm{Ar} + \gamma & \end{array}$$

The electron produced in the β-decay channel, with an energy up to 1.3 MeV, leads to the production of Cherenkov light when traveling in water. In the electron capture channel, fast electrons with subsequent Cherenkov light emission are produced by Compton scattering of the 1.46 MeV photon, released by the excited Ar nuclei.

The detection rate, R_s, of Cherenkov photons from products of ^{40}K decays on an ANTARES optical module can be factorised as:

$$R_s = B_q \cdot V_s, \tag{3.1}$$

with B_q the ^{40}K decay rate per unit volume and V_s the effective volume around a single OM for detecting a single photon from a ^{40}K decay. As there is no preferred decay direction, V_s can be calculated in a semi-analytical way, by integrating over the decay positions around the OM. One obtains, for a given wavelength λ, a factorisation into a wavelength-dependent effective area $A(\lambda)$ and the corresponding photon absorption length $L_{abs}(\lambda)$ of sea water. V_s can then be written as:

$$V_s = A_s \cdot L^0_{abs}, \tag{3.2}$$

with $A_s = \int A(\lambda)\Phi(\lambda)L_{abs}(\lambda)d\lambda/\Phi_{tot}L^0_{abs}$, with $\Phi(\lambda)$ containing the — arbitrarily normalised — λ dependence of the Cherenkov photon flux (close to $1/\lambda^2$), Φ_{tot} its integral over a given wavelength range and L^0_{abs} the absorption length at some reference wavelength. $A(\lambda)$ is determined by simulating an isotropic photon flux around an OM and depends on the OM properties such as the size of its photocathode, its quantum efficiency, and its angular acceptance. These simulations yield $A_s = 420 \pm 50\,\mathrm{cm}^2$, where the error is dominated by uncertainties in the OM properties. The absorption length at the ANTARES site has been measured to $L^0_{abs} = 60 \pm 8\,\mathrm{m}$ for $\lambda = 470\,\mathrm{nm}$ [113].

If a ^{40}K nucleus decays near a storey, the associated Cherenkov light can be recorded by two OMs almost simultaneously: this kind of signal is referred to as *genuine* coincidence. Its rate can be written as:

$$R_c = B_q \cdot V_c, \tag{3.3}$$

where V_c is an effective volume around a pair of OMs for the detection of a coincident signal from a single ^{40}K decay. The value of V_c is derived from Geant-3 simulations, modeling ^{40}K decays around a pair of OMs and propagating the resulting Cherenkov photons through the sea water with a full tracking of electrons, including multiple scattering and velocity dependence of Cherenkov light emission. These simulations yield $V_c = 1100 \pm 370\,\mathrm{cm}^3$. Whereas ^{40}K decays can contribute to the rate of a single OM, R_s, up to a distance of $\sim L^0_{abs}$, contributions to the rate of genuine coincidences, R_c, are confined to a small volume in the vicinity of the storey, with 90% occuring within 3 m. At such a distance, the effect of absorption is below 5% and the associated uncertainties become negligible. The dominating error for R_c originates from the uncertainties on the OM properties.

Both R_s and R_c depend on B_q, with:

$$B_q = r_s \cdot r_K \cdot r_I \cdot \rho \cdot \frac{\ln 2}{\tau_{1/2}} \cdot \frac{N_A}{A}, \tag{3.4}$$

where N_A is the Avogadro number, $A = 39.96$ [114] and $\tau_{1/2} = 1.25 \times 10^9$ years [115] are the atomic mass and lifetime of ^{40}K, and $\rho = 1.038\,\mathrm{g/cm}^3$ is the density of deep-sea water at the ANTARES site, which is derived from in situ measurements of pressure, temperature and salinity, r_s. The parameter r_K is the potassium fraction in Mediterranean Sea salt and r_I is the isotope fraction of ^{40}K. The last three quantities can be considered stable over the lifetime of ANTARES with variations smaller than 1%. The salinity is monitored directly with the ANTARES instruments and found to be $r_s = 3.844\%$, while $r_K = 1.11\%$ from [116] and $r_I = 1.17 \cdot 10^{-4}$ from [117]. This yields $B_q = 13700 \pm 200\,\mathrm{s}^{-1}\mathrm{m}^{-3}$.

With this value, $R_s = 35 \pm 8\,\mathrm{kHz}$ and $R_c = 15 \pm 5\,\mathrm{Hz}$ are the single and genuine coincidence rates obtained from simulations. The observed single photon rates in ANTARES OMs are about 55 kHz, due to additional light from bioluminescence that cannot be filtered out at the single photon level. This phenomenon can result in variation of the single photon rates up to several order of magnitude. For this reason, single photon rates are difficult to exploit as calibration source. On the other hand, no impact due to bioluminescence is observed at the level of the genuine coincidence rates. Additional coincident light background from low-energy muons does not exceed 1%. Therefore, the rest of the paper is devoted to the analysis of the coincident signal.

3.2 Detection efficiency calibration using ^{40}K

Data collected from mid 2008 to December 2017 have been analysed in this work. The ^{40}K trigger selects coincident photons in adjacent OMs if they are detected within a narrow time window of 50 ns.

From the completion of the detector in May 2008 until November 2009, dedicated runs with ^{40}K triggers have been taken once per week, with a down-scaling factor of 4 in order not to saturate the readout data acquisition system. For these runs, the ones belonging to the same month have been merged together.

The ^{40}K trigger has then been integrated into the standard data-taking setup, with a down-scaling factor of 200. For these runs, each month of data taking has been divided into five periods.

Both the genuine coincidences induced by the same ^{40}K decay process and random background coincidences, which are due to distinct ^{40}K decays as well as to bioluminescence effects, contribute to hit pairs on adjacent OMs with small time differences Δt. Figure 3.1 shows an example of the distribution of the time difference between hits on two adjacent OMs. A Gaussian peak from genuine coincidences is clearly visible on top of a flat pedestal from uncorrelated coincidences.

The distribution of the coincidence signals is fitted with a Gaussian distribution

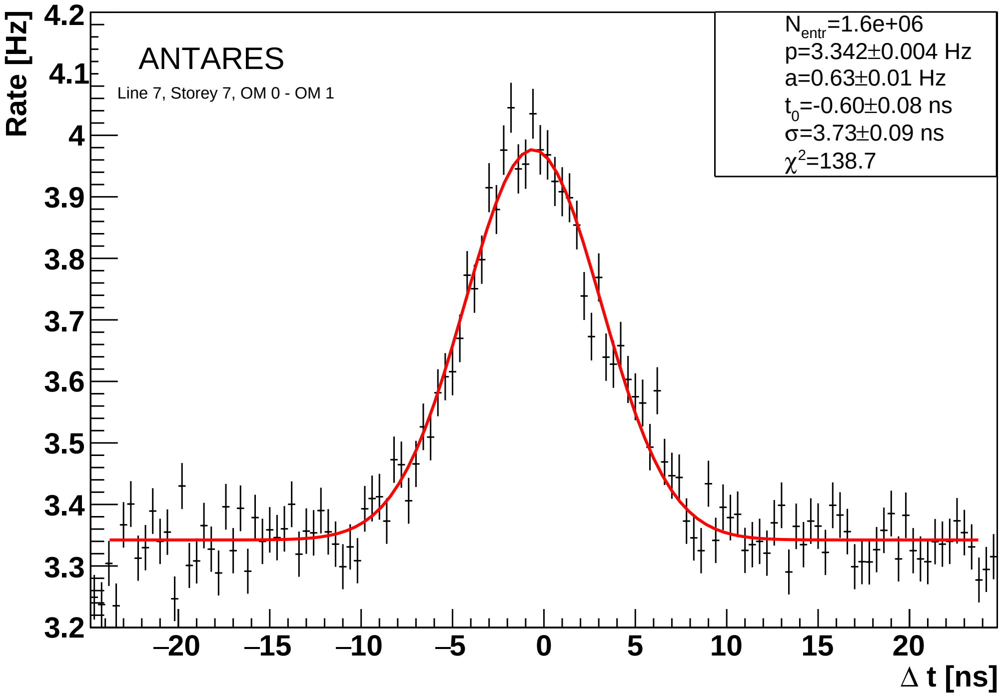

Figure 3.1: Example of the detected hit time differences, Δt, between two adjacent OMs. The fitted parameters are listed as well (see Equation 3.5 for details). The plot refers to one pair of OMs in the same storey (Line 7, Storey 7, OM 0 - OM 1) for one of the periods considered in the analysis.

added to a constant:

$$f(t) = p + a \cdot \exp(-\frac{(t - t_0)^2}{2\sigma^2}), \tag{3.5}$$

where p is the baseline, a the amplitude of the Gaussian peak due to genuine coincidences, σ is the peak width and t_0 the residual time offset between the hits on adjacent OMs. A value of $\sigma \sim 4\,\mathrm{ns}$ is expected, mainly due to the distance between the OMs and the spatial distribution of detected ^{40}K coincidences around the storey. A simple estimation can be obtained by considering the difference in the distance traveled by two photons emitted at the same position and detected by two different PMTs. In ANTARES the distance between the centers of photocathodes of two PMTs of the same storey is $l = 1.0\,\mathrm{m}$, while the photocathode diameter d

is about 25 cm. Therefore, neglecting light scattering, the maximum traveled path difference for two photons is $l + d = 1.25\,\mathrm{m}$. Given the Cherenkov light velocity of $v_g = 0.217\,\mathrm{m/ns}$, the corresponding time difference is about 5.8 ns. By averaging over all the ^{40}K disintegration positions which yield a genuine coincidence, a value of $\sigma = 4\,\mathrm{ns}$ is obtained, compatible with Figure 3.1.

For perfectly calibrated OMs, t_0 would be expected at 0 ns. Deviations from the expected value of t_0 are mainly due to different PMT transit times. This makes the ^{40}K method an integral part of the time calibration procedure, as will be discussed in more detail in Section 3.4.

The fit parameters can be used to estimate the number of events corresponding to the peak area, as:

$$R = \frac{a \cdot \sigma \cdot \sqrt{2\pi}}{\Delta\tau}, \tag{3.6}$$

where $\Delta\tau = 0.4\,\mathrm{ns}$ is the bin width used for the histogram.

For each storey three coincidence rates are measured (R_{01}, R_{12} and R_{20}). These quantities are directly related to the photon detection efficiency of the three OMs (ϵ_0, ϵ_1 and ϵ_2):

$$R_{ij} = R_c^* \cdot \epsilon_i \cdot \epsilon_j, \tag{3.7}$$

where R_c^* is the rate for two nominal OMs with efficiencies equal to 1. A value of $R_c^* = 15\,\mathrm{Hz}$ is used. This value is obtained as an average detector coincidence rate at the beginning of the analysed data set, and coincides with what is found in simulation. Solving the system of three equations, the corresponding efficiencies are derived:

$$\epsilon_i = \sqrt{\frac{1}{R_c^*}\frac{R_{ij} \cdot R_{ki}}{R_{jk}}}. \tag{3.8}$$

When an OM in a storey is not working for a given period, only one coincidence rate is measured, which is not sufficient to determine the two efficiencies. In this case, equal efficiencies for the two working OMs are assumed, namely:

$$\epsilon_i = \epsilon_j = \sqrt{\frac{R_{ij}}{R_c^*}}. \tag{3.9}$$

If two OMs in a storey are inactive no coincidences can be measured. In this case the average efficiency value of the line hosting that particular storey is assigned to the working OM for this period.

All coincidence histograms for all periods have been fitted according to Equation 3.5. Data quality selection criteria have been applied, to ensure stable and reliable input for the subsequent efficiency calculation. A cut on the number of entries on each histogram, N_{entr}, excludes from the analysis all those cases for which the fit fails due to lack of statistics. This includes the cases, for instance, in which one of the two OMs is only partially active. Taking into account that there are four fitted parameters and 120 bins in each histogram, a χ^2 of 116 is expected for a good fit. Histograms with $\chi^2 \geqslant 200$ are excluded. Additional cuts on the fitted amplitude value and its uncertainty, Δa, have been applied to ensure a clear signal above the background. Furthermore, expected values of the Gaussian mean and width are known, thus cuts on these parameters have been applied. All the selection criteria applied are reported in Table 3.1.

Accepted Values
$N_{entr} > 2000$
$\chi^2 < 200$
$a > 0.1\,\mathrm{Hz}$
$\Delta a/a < 0.1$
$1.5\,\mathrm{ns} < \sigma < 6.5\,\mathrm{ns}$
$\lvert t_0 \rvert < 20.0\,\mathrm{ns}$

Table 3.1: Values of data selection criteria applied in the analysis. The parameter nomenclature corresponds to the one used in Equation 3.5.

After applying these cuts, the efficiency can be determined on average for 77% of those OMs which are active in a given period. The efficiency of the remaining working OMs is derived from adjacent OMs or from the average of the corresponding detection line as described above.

3.3 Results

Histograms passing the quality criteria are then used to compute the OM photon detection efficiency, as described in Section 3.2. Figure 3.2 shows the photon detection efficiency as a function of time for one OM as an example. The uncertainty on the resulting photon detection efficiency of each OM has been calculated from the uncertainty on the fitted parameters and it is found to be around 3% for all analysed periods. The total uncertainty is dominated by the statistical error. The systematic uncertainties (discussed later in this section) contribute on average only about 20% of the total uncertainty.

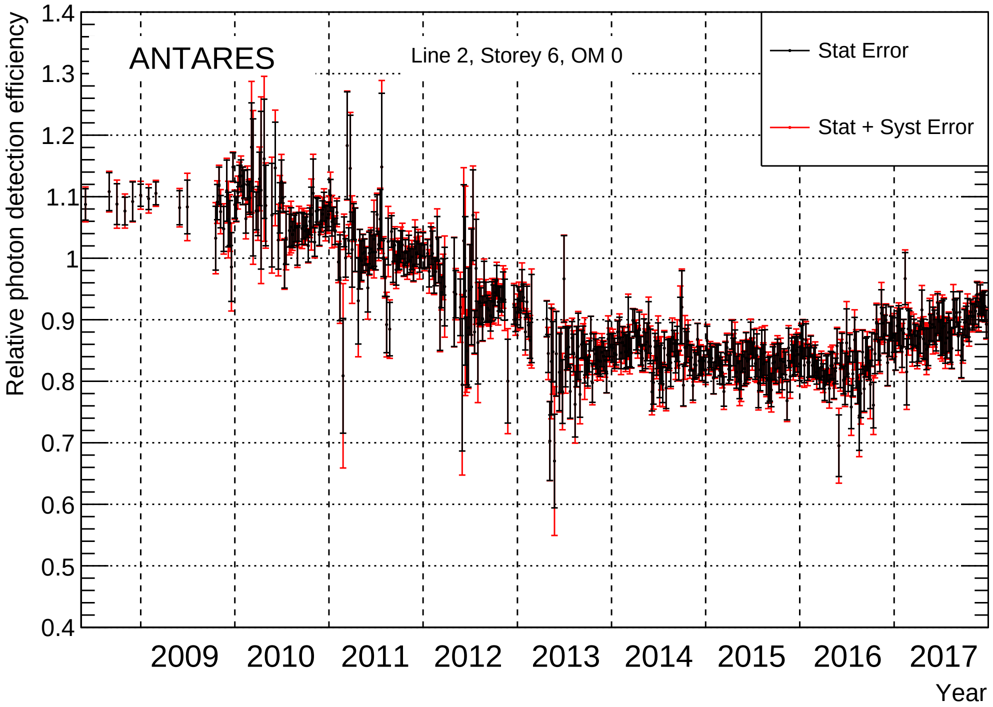

Figure 3.2: Photon detection efficiency as a function of time for one ANTARES OM (Line 2, Storey 6, OM 0). Error bars correspond to statistical (black) and statistical plus systematic (red) contributions.

In order to monitor the status of the whole detector over several years, the average photon detection efficiency $\bar{\epsilon}$ as a function of time has been determined. For each period, the average $\bar{\epsilon}$ is computed over all OMs with non-zero efficiency. The result is shown in Figure 3.3. It can be seen that, after a decrease over several years, the OM photon detection efficiency has finally stabilised over the last years. An overall modest detection efficiency loss of 20% is observed over the whole analysed time period.

The detection efficiency drop, as observed from 2010 to 2012, may be correlated with changes in deep water masses, experienced by the upper ocean layer in the Gulf of Lion and which lead to the formation of dense water through a process known as "open-sea convection" [118]. Sedimentation as well as biofuling processes might also be among the causes for such a decrease in photon detection efficiency.

The distribution of the detected charge is regularly monitored for all PMTs and if either a significant broadening or a shift from the nominal position of the peak due to a single photoelectron is noticed a recalibration is performed by means of high voltage tuning (HVT). The HVT procedure adjusts the effective gain of individual PMTs to the nominal one; the procedure thus prevents detection effeciency losses due to a low gain and bias on the trigger logics. The effects of the HVT procedure, which is performed once or twice per year, are evident on the time dependence of $\overline{\epsilon}$ shown in Figure 3.3. In particular, it can be seen that from 2014, almost the total OM photon detection efficiency can be recovered by means of the HVT procedure, showing that biological phenomena do not play a role anymore.

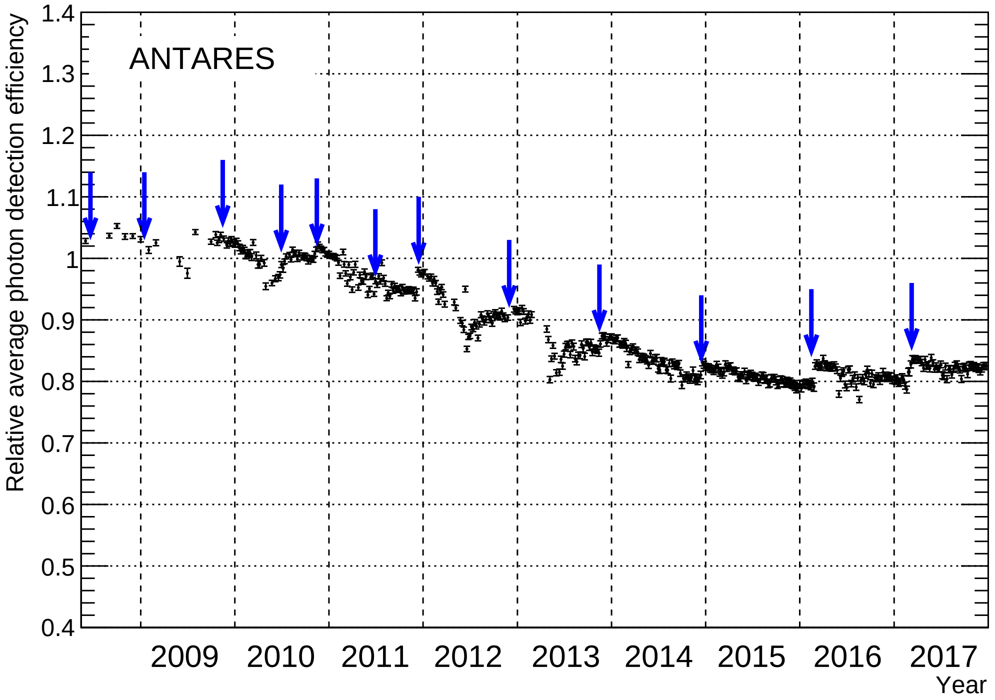

Figure 3.3: Relative OM efficiency averaged over the whole detector as a function of time. The blue arrows indicate the periods in which high voltage tuning of the PMTs has been performed, while error bars indicate the statistical error σ_{mean} on the mean efficiency.

When averaging the efficiencies of individual PMTs over the whole detector, two statistical quantities are considered: the standard deviation and the error on the mean. The standard deviation is given by:

$$\sigma_{\text{std}} = \sqrt{\frac{1}{N-1}\sum_i (\epsilon_i - \bar{\epsilon})^2}, \tag{3.10}$$

where N is the total number of considered OMs for a given period and ϵ_i is the efficiency of OM i in that particular period. Thanks to the HVT procedure, the σ_{std} remains stable at the order of 10%, as can be seen in Figure 3.4, where this quantity is shown for all analysed periods. This justifies the fact that we used the average efficiency of the OMs on a given line for those working OMs whose efficiency cannot be computed through the ^{40}K calibration.

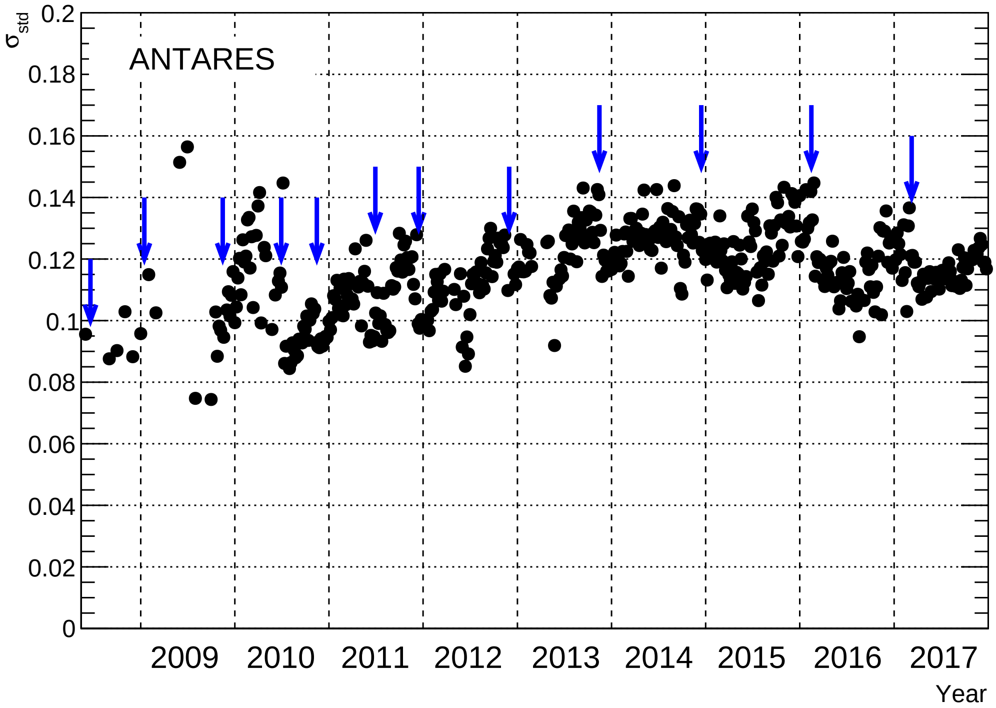

Figure 3.4: Standard deviation σ_{std} of the relative photon detection efficiency as a function of time. The blue arrows indicate the periods in which high voltage tuning of the PMTs has been performed.

The statistical error shown in Figure 3.3 is the error on the mean, defined as:

$$\sigma_{\text{mean}} = \frac{\sigma_{\text{std}}}{\sqrt{N}}. \tag{3.11}$$

This quantity is typically of the order of 1%.

Possible systematic uncertainties on the individual OM efficiencies, based on the assumption on the Gaussian shape for the distribution of the coincidence rates, have been considered as well. In addition to the intrinsic width of the coincidence peak due to the arrival of photons from a ^{40}K decay process, the shape of the distribution is also affected by photon scattering and the time response of the PMTs. In order to account for these effects, the analysis considers an additional Gaussian term with a larger width compared to that already shown in Equation 3.5. Using as genuine coincidence rate the sum of the areas under the two Gaussians, the systematic uncertainty has been evaluated as the difference between the resulting efficiencies from the two procedures. Generally it is found that the area under the leading Gaussian is equal to the one of the one Gaussian fit, and the area under the second Gaussian is compatible with zero within its error.

It is worth mentioning that the effects due to some known artefacts from a typical PMT response [100], such as delayed hits, remain undetectable in the narrow time window used in this work. The calculated efficiencies exclude these hits, which are later added in the ANTARES simulation chain.

3.4 Time calibration

In order to meet the target angular resolution of the detector, a time syncronisation between all detector components better than 1 ns is required [101]. To achieve such precision a master clock system, located onshore, provides a common reference time to all the offshore electronics, via a network of optical fibers. Further calibration is needed for the delay between the time when the hit is detected and the photon arrival time at the photocathode of the PMT. As previously discussed in Chapter 2, these time calibrations were performed during the detector construction and are continuously monitored on a weekly basis. Two systems of external light sources are used: LED beacons located on four storeys on each detector line, and laser beacons located on the base, at the bottom of several detection lines. They allow to perform both inter-line and inter-storey time calibrations [119]. Reconstructions of tracks from downward going muons created in cosmic-ray interactions in the atmosphere are used as well to determine inter-line and inter-storey time calibrations [120]. The ^{40}K method completes the time calibration chain by providing intra-storey timing. All three methods combined assure a precision level of 0.5 ns for each individual PMT.

In Figure 3.5 the distribution of the fitted time offset, t_0, obtained from the ^{40}K coincidence histogram of one OM pair is shown as a function of time.

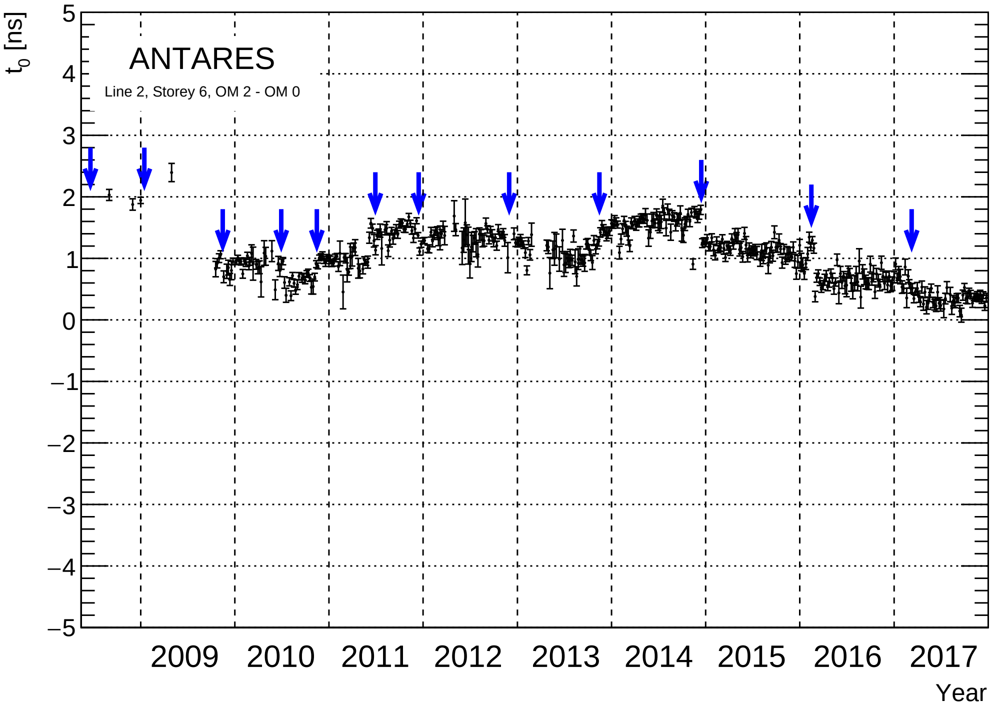

Figure 3.5: Fitted time offset as a function of time for one OM pair (Line 2, Storey 6, OM 2 - OM 0). The blue arrows indicate the periods in which high voltage tuning of the PMTs has been performed.

It can be seen that between subsequent HVT procedures the time difference between two adjacent OMs is stable and its value can be monitored to better than 0.5 ns. These values, which are produced for each OM pair, serve as input for the intra-storey calibration procedure.

The standard deviation of the time offset distribution, averaged over the whole detector, is illustrated in Figure 3.6. The apparent trend is an increase of the standard deviation as a function of time (from ~ 2 to ~ 4.5 ns in 9 years). This increase could be correlated to the HVT procedure, which is performed in order to keep the OM detection efficiency at their best. This procedure, in fact, acts on each OM transit time independently, in order to adjust each individual PMT gain, resulting in an increase of the standard deviation.

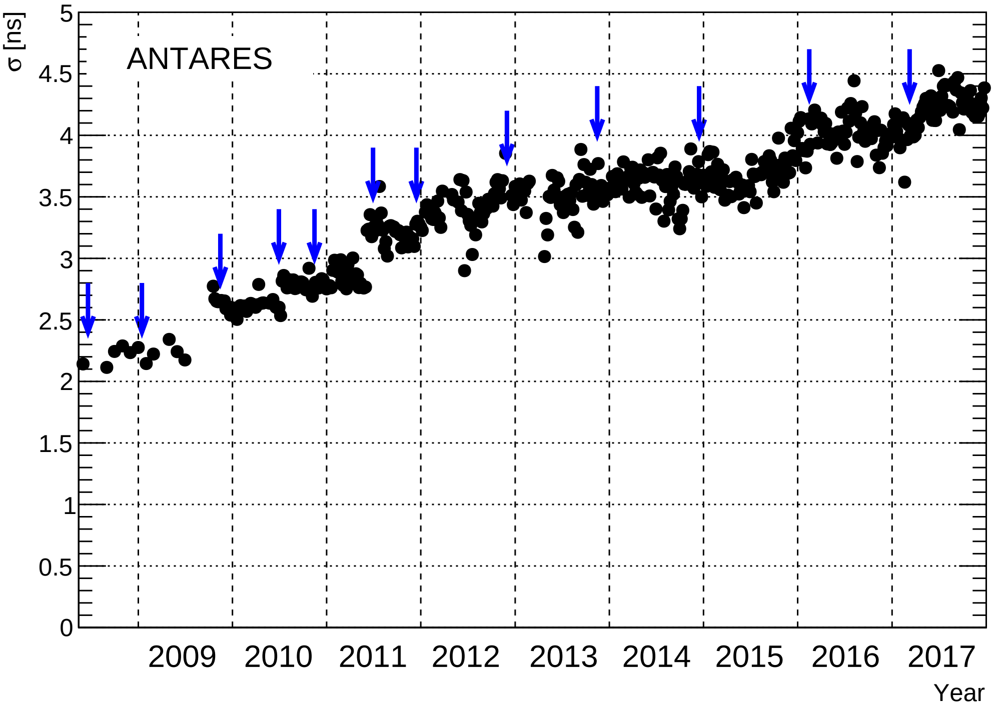

Figure 3.6: Standard deviation, σ, of the average time offset as a function of time. The blue arrows indicate the periods in which high voltage tuning of the PMTs has been performed.

3.5 OM efficiency dependence on position in water

An additional study has been done in order to determine whether there is a dependence of the OMs efficiency on the positions of the devices along the ANTARES detection lines. To this purpose, OMs efficiency for storeys 1, 12 and 20 of each line have been used. These storeys are located closest to the seabed, in the middle of the line and almost on top of it, respectively. The efficiency of OMs at the same depth have been averaged, in order to obtain an efficiency mean value for each depth and at each period.

In Figure 3.7, the efficiency as a function of time is shown for the three different storeys depths.

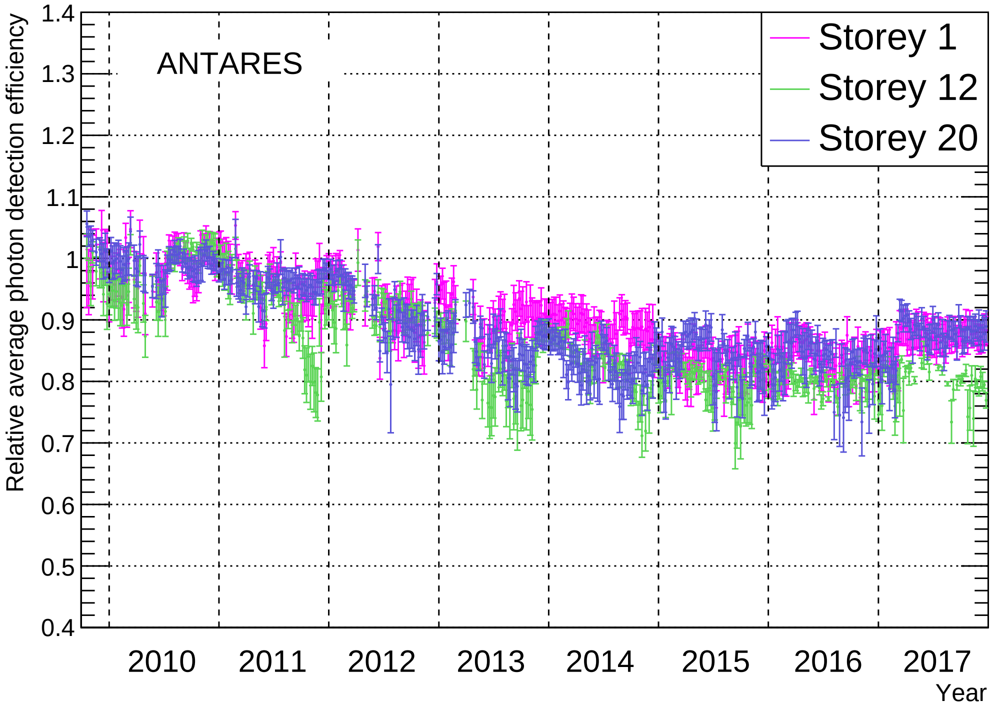

Figure 3.7: OM photon detection efficiency for storeys at different depths: storey 1 (purple), storey 12 (green) and storey 20 (blue).

As can be inferred from the figure, no evidence of a particular correlation between the storey position in the water and the corresponding OM efficiency is seen.

3.6 Conclusions and outlook

Using data collected by the ANTARES neutrino telescope with a dedicated ^{40}K trigger, the photon detection efficiencies for all OMs have been computed from mid 2008 to the end of 2017. This analysis presents the stability of a PMT based detector in the hostile environment of the deep-sea, for the longest period ever recorded. It demonstrates that future underwater experiments can remain in operation for timescale of at least a decade without major efficiency degradation. An average decrease of the OM efficiency by 20%, as observed from 2008 to 2017, implies a loss of only 15% in the detection efficiency of an astrophysical signal with a full sky E^{-2} spectrum. The effect of PMT ageing is surely present. The best way to test the biofouling development is the recovery the the OMs, which is planned at the end of the ANTARES physical operation, around 2020.

The results of this study serve as input for detailed Monte Carlo simulations of the ANTARES detector, which include a realistic simulation of the OM efficiencies in each data taking run. The ^{40}K method is also part of the time calibration of the detector. This analysis has been recently published in the *European Physical Journal C* [121].

This procedure can be also exploited in KM3NeT, the next-generation neutrino telescope in the Mediterranean Sea [53]. KM3NeT will consist of two main detectors, ARCA in Sicily, devoted to high energy astroparticle physics, and ORCA in France, focused on few-GeV atmospheric neutrino studies. They both use a configuration similar to the one of ANTARES, but with 31 instead of three PMTs on each storey. This will allow to collect not only double coincidences from ^{40}K decays, but also higher multiplicities, improving the technique to determine the photon detection efficiencies.

Chapter 4

Monte Carlo simulations

In this Chapter the ANTARES Monte Carlo (MC) chain will be presented. First the main input models will be described, and then the different software used to simulate neutrino as well as atmospheric muon generation and propagation will be illustrated. The ANTARES MC has been recently updated to its last version, whose main changes with respect to the previous production are in the water model and in the treatment of the OM efficiencies. Both these ingredients have been studied as part of this thesis work; the former will be discussed in more details in this Chapter, while to the latter a dedicated part has been devoted in Chapter 3.

4.1 General scheme

Before entering the details of each step of the ANTARES MC chain, let us first draw a more general picture of the whole process.

The aim of the MC production is to reproduce in the most realistic way as possible the events expected at the detector, as well as the response of the apparatus when recording such events. The environment conditions are not always stable over time; seasonal changes in the event rates are expected due to biological activity in the sea. Moreover, the detector itself is not running always in the same conditions: some components could be temporary off or degrading in time, resulting in a variation of efficiency. Furthermore, active triggers are adjusted depending on the sea conditions. In order to take into account all these *non-constant* effects, ANTARES applies a *run-by-run* MC approach, in which the particular conditions at the time of a data run acquisition are used as input for the MC simulation of the corresponding run.

The whole MC process can be divided in three main steps:

- **Event Generation**: particles detectable by ANTARES are generated and their physical properties are stored;
- **Event Propagation**: particles are propagated through the detector and the emitted Cherenkov light path to the OMs is simulated;
- **Event Detection**: the data acquisition chain is simulated, taking into account environmental conditions at the time of the run, as well as the OMs status and the active triggers.

In the following sections these three parts will be described in more detail. A dedicated additional section (4.4) will be devoted to some tests, performed in order to compare different water models.

4.2 Event generation

In this stage the main physics events detectable by ANTARES are generated; these are neutrino induced interactions and atmospheric muons produced by cosmic rays. The generation volume is a cylinder, called *can*, which surrounds the ANTARES instrumented volume, and extends it by a certain number of light attenuation length. Inside the *can*, the Cherenkov light is generated, while, outside this volume, only energy loss of particles such as muons is considered. The direction and energy of the generated particles are stored together with the ones of secondary particles, produced by neutrino interactions within a detectable distance from the apparatus.

For generating neutrino events the *GENHEN* (GENerator of High Energy Neutrinos) [28] package has been developed inside the ANTARES Collaboration. It allows to simulate neutrino events of all flavours and for all interactions. The energy range spreads from a few GeV to multi-PeV, making it suitable for all kind of neutrino studies. The generation spectrum follows a power law $\propto E^{-\gamma}$, with $\gamma = 1.7$; then, events can be weighted according to different neutrino fluxes, producing the expected event rate under a specific assumption. In terms of available MC statistics, for atmospheric neutrinos with $E_\nu \in [20 - 100]$ GeV, we dispose of a lifetime almost three hundreds times larger than the actual one.

Even though ANTARES sub-marine location provides a good shielding against atmospheric muons, still a large amount of them will reach the detector. The generator used in ANTARES to simulate atmospheric muons is *MUPAGE* [122]; the energy and angular distributions, as well as the multiplicity of muons propagating in sea water are parametrized. This method is preferable with respect to full simulation of the air shower, since it allows to save computational time, which has to be taken into account since a very high statistics is needed. For the same reason, only 1/3 of the actual lifetime is simulated in atmospheric muons.

4.3 Event propagation

All the generated particles are then propagated through the *can* volume. This is done thanks to a *GEANT*-based package [123], which takes into account all the involved physics processes and computes the probability that photons emitted by a particle reach the OM surface, producing a hit. This software is composed by three main parts. The first one simulates the Cherenkov photons emitted by a particle when traveling in water, including the light contribution from secondary particles and accounting for wavelength-dependent absorption and scattering. In case of muons, the tracking is done for steps of 1 m; for electrons, instead, the track length depends on the momentum and on the medium density. The second step builds probability hit distributions on OMs, taking as input the Cherenkov photons generated by the previous step. These distributions depend on 5 parameters: the distance from the particle, 3 angles defining the direction of the photons with respect to the particle and to the OM and the photon arrival time. These probability tables are filled for muons as well as for electromagnetic showers, using electrons for the light generation step. In the third step, these pre-compiled tables are employed, together with a geometrical description of the detector in order to simulate the events within the ANTARES volume.

In principle, the same reasoning could be applied to hadronic showers, but this would require a huge computational time due to the complexity and the diversity of each hadronic process. For this reason, each hadron is treated as an electron, for which the existing tables can be used with dedicated correction weights, according to the hadron under study.

4.4 Data/MC comparison study with different water models

Another important input parameter for the MC simulation is the water model at the ANTARES site. Since some tests on different water models have been performed as part of this thesis work, a dedicated Section is devoted to these results.

Three different water models have been studied, which differ one from the other by the absorption length as a function of the light wavelength. The three tested models will be referred in the following as *antares*, *intermediate* and *nemo*. The first one is the model used until the previous ANTARES MC production [113], the latter is the one employed by the NEMO Collaboration [124], while the second, as the name suggests, is an intermediate solution between the other two. In Figure 4.1, the wavelength dependence of the absorption length is shown, as in *antares* and *nemo* models, compared to the reference measurement for pure sea water by Smith & Baker [125].

In order to define the three water models starting from the parameterizations presented in Figure 4.1, one can simply write the absorption length $a(\lambda)$ as:

$$a(\lambda) = a_{ANT}(\lambda) + C_N[a_N(\lambda) - a_{ANT}(\lambda)] \tag{4.1}$$

where $a_{ANT}(\lambda)$ is the *antares* absorption wavelength, $a_N(\lambda)$ is the *nemo* one, and C_N is a coefficient, such that:

- $C_N = 0 \Rightarrow$ *antares* water;
- $C_N = 0.5 \Rightarrow$ *intermediate* water;
- $C_N = 1 \Rightarrow$ *nemo* water.

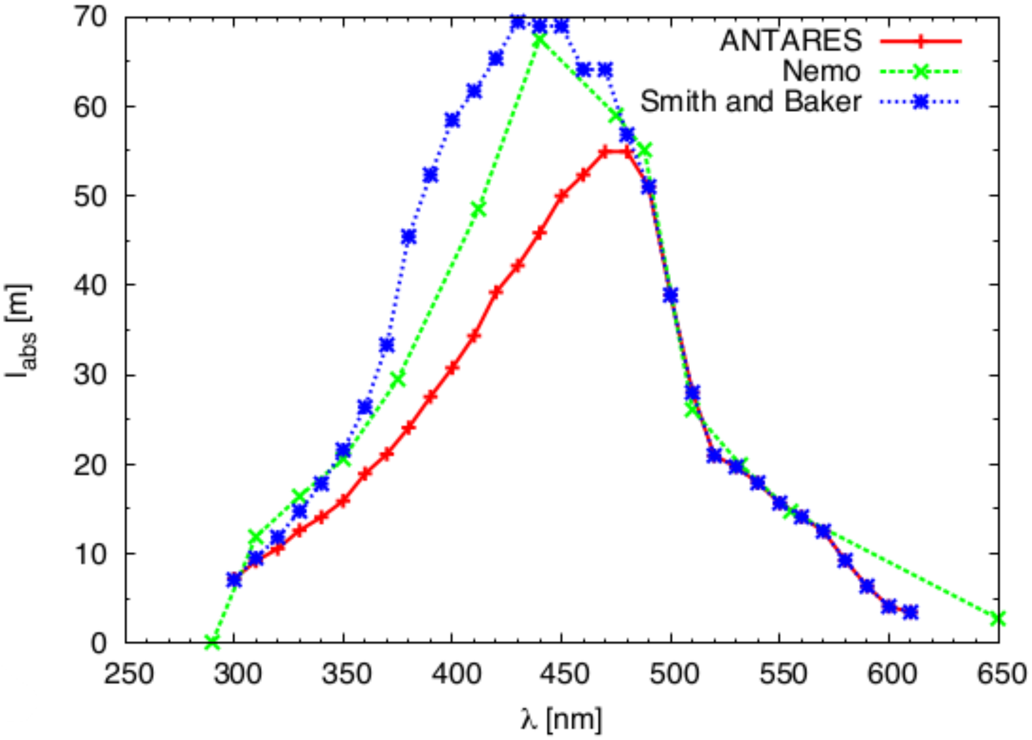

Figure 4.1: Absorption length as a function of wavelength, for *antares* model (red), *nemo* model (green) and Smith & Baker measurements (blue) [113].

The study has been based on data/MC comparison plots. Only events reconstructed as up-going and induced by CC interactions of ν_μ neutrinos have been considered. The muon track reconstruction has been performed by *AAFit* (see Chapter 5 for a detailed description of the algorithm) and some dedicated quality cuts have been applied in order to obtain a sample practically free from atmospheric muon background. The quantity considered for the comparison has been the hit time residual distributions with respect to the reconstructed muon track. Two distinct periods of data have been analyzed, namely March 2008 and December 2015.

The MC histograms have then been normalized with the ratio of the number of entries between the data and MC itself, in order to test the shape of the distributions. Four different modes have been analysed, differing on the histogram binning as well as on the time interval considered.

- Mode 1: histograms of 200 bins of 1 ns, from -100 ns to 100 ns;
- Mode 2: histograms of 100 bins of 1 ns, from 0 ns to 100 ns;
- Mode 3: histograms of 100 bins of 2 ns, from -100 ns to 100 ns;
- Mode 4: histograms of 50 bins of 2 ns, from 0 ns to 100 ns.

In the second and fourth mode results have been considered after removing the noise-dominated part of the histogram, namely from the peak at 0 ns to the tail on the left-hand side. In the following figures, the results obtained in the different modes are shown, for both analyzed periods and for all the water models described above.

Mode 1

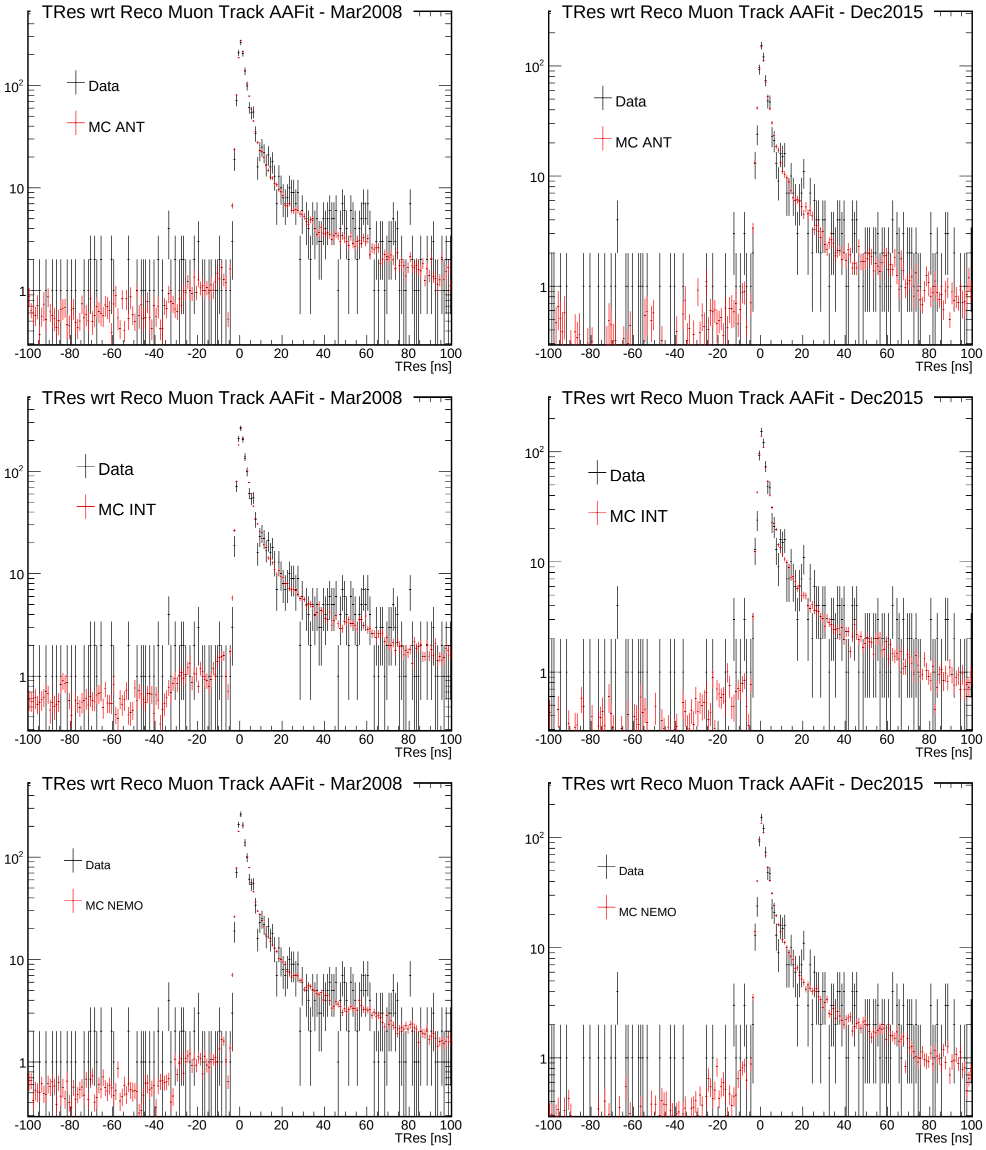

Figure 4.2: From top to bottom: *antares*, *intermediate* and *nemo* MC productions vs data; from left to right: the two analyzed periods, March 2008 and December 2015. Histograms are in 200 bins of 1 ns, and MC are normalized with the ratio between the number of entries of data and MC itself.

Mode 2

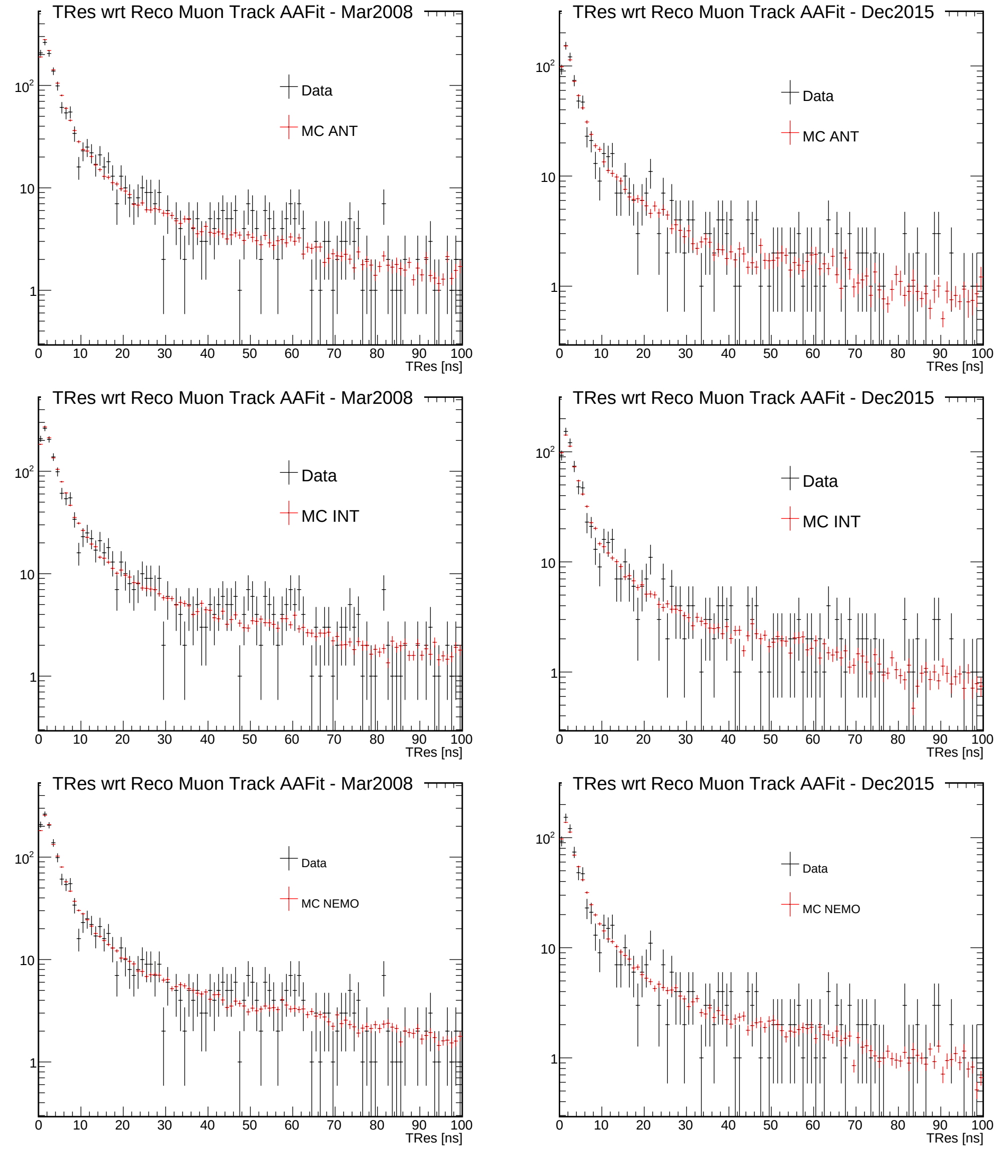

Figure 4.3: From top to bottom: *antares*, *intermediate* and *nemo* MC productions vs data; from left to right: the two analyzed periods, March 2008 and December 2015. Histograms are in 100 bins of 1 ns, and MC are normalized with the ratio between the number of entries of data and MC itself.

Mode 3

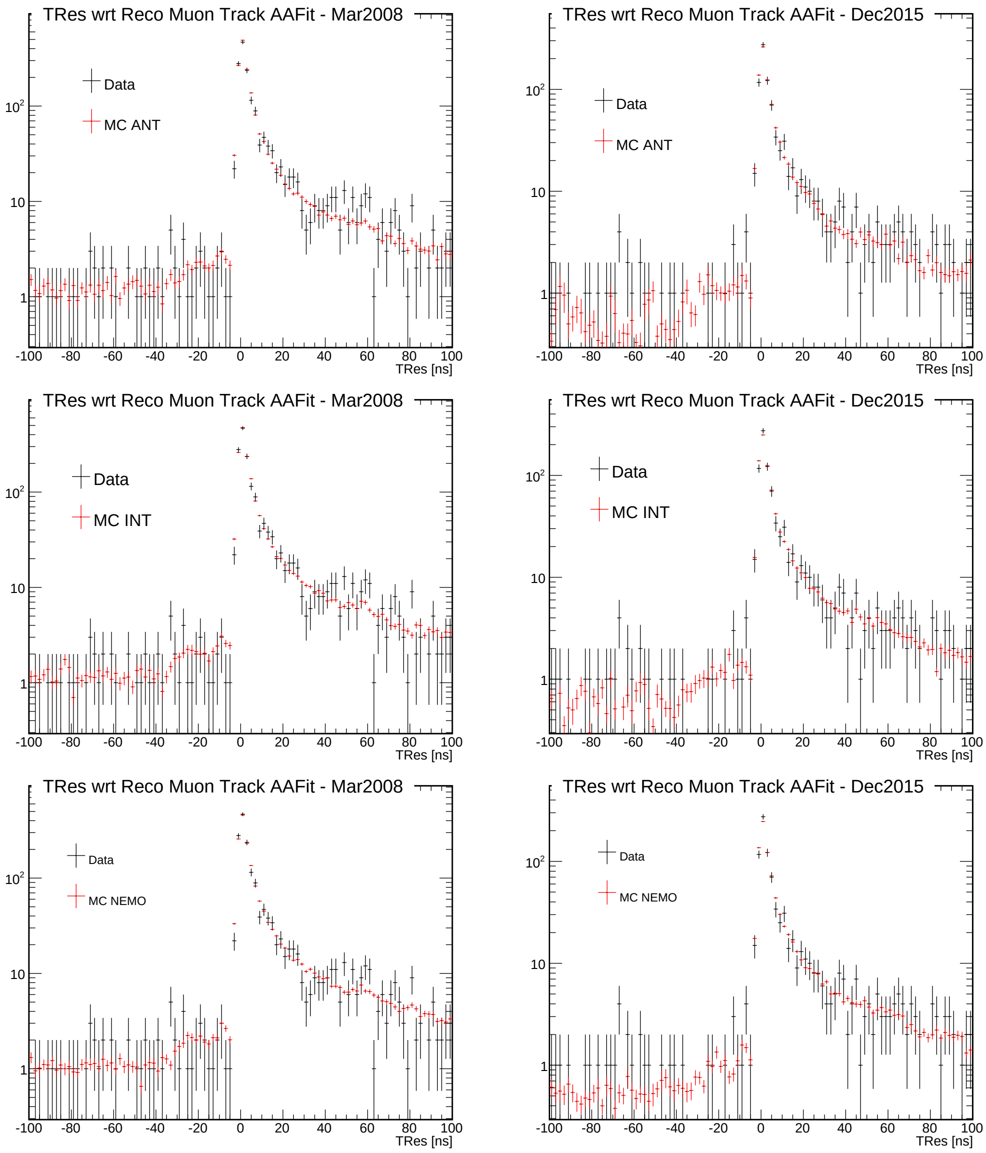

Figure 4.4: From top to bottom: *antares*, *intermediate* and *nemo* MC productions vs data; from left to right: the two analyzed periods, March 2008 and December 2015. Histograms are in 100 bins of 2 ns, and MC are normalized with the ratio between the number of entries of data and MC itself.

Mode 4

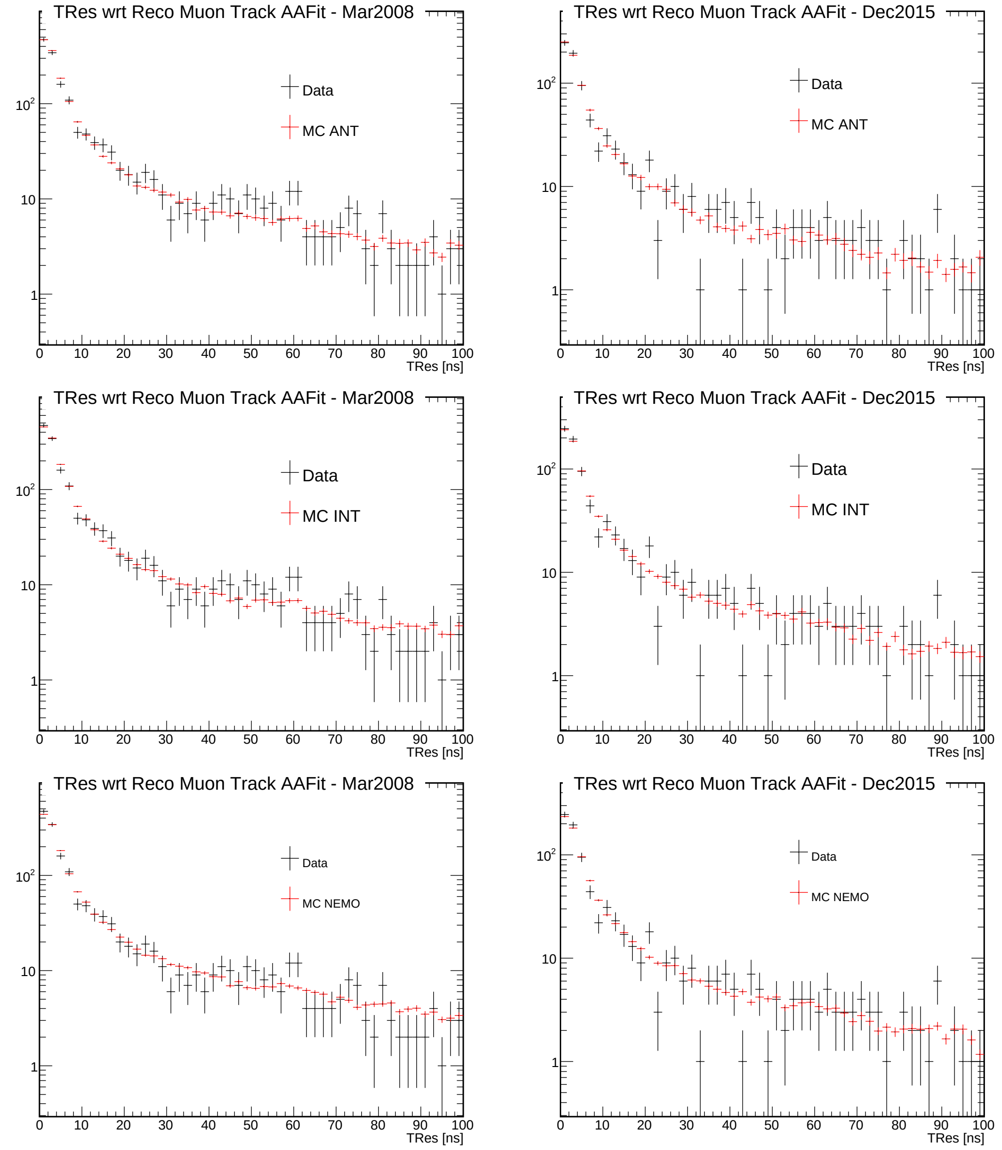

Figure 4.5: From top to bottom: *antares*, *intermediate* and *nemo* MC productions vs data; from left to right: the two analyzed periods, March 2008 and December 2015. Histograms are in 50 bins of 2 ns, and MC are normalized with the ratio between the number of entries of data and MC itself.

One can clearly distinguish in the figures a peak, which is due to the direct photons and ends in the right-hand side tail, which accounts for delayed photons, namely those photons which scattered before being detected. The tail on the left-hand side, instead, is expected due to uncorrelated noise hits. This is the reason why we cut it for some of the performed tests.

A change in the water properties at the ANTARES site, which is represented by a change on the absorption length, would result in a variation of the hit time residual distribution, since it would affect the probability for a photon of being scattered before reaching the PMT.

In order to compare the obtained results in a quantitative way, a χ^2 test has been performed. The ROOT [126] function `Chi2Test()` has been used, with the "UW" option, which allows to compare unweighted with weighted histograms. The p-values have also been computed, since it allows to directly compare the results of the different χ^2 tests.
The current ROOT implementation of `Chi2Test()` is based on [127]; it follows the analysis of the residuals, namely the difference between bin contents and expected bin contents. The test statistic is defined as:

$$\chi^2 = \sum_{i=1}^{r} \frac{(n_i - N\hat{p}_i)^2}{N\hat{p}_i} + \sum_{i=1}^{r} \frac{(w_i - W\hat{p}_i)^2}{s_i^2} \tag{4.2}$$

where:

$$N = \sum_{i=0}^{r} n_i, \quad W = \sum_{i=0}^{r} w_i \tag{4.3}$$

are the sum of each bin contents for the unweighted and weighted histograms, respectively;

$$\hat{p_i} = \frac{Ww_i - Ns_i^2 + \sqrt{(Ww_i - Ns_i^2)^2 + 4W^2 s_i^2 n_i}}{2W^2} \tag{4.4}$$

and s_i^2 is the sum of the square of the weights of events in bin i.

In the following tables the χ^2 test results are presented, divided by the number of degrees of freedom, for each period and for each considered mode.

Model	Mode 1	Mode 2	Mode 3	Mode 4
antares	0.96	1.06	1.09	1.11
intermediate	0.99	1.09	1.04	1.12
nemo	0.98	1.01	1.02	1.11

Table 4.1: χ^2/dof for March 2008 and all the different modes in which the test has been performed.

Model	Mode 1	Mode 2	Mode 3	Mode 4
antares	1.35	1.08	1.17	1.23
intermediate	1.36	1.03	1.03	1.24
nemo	1.24	0.95	1.05	0.96

Table 4.2: χ^2/dof for December 2015 and all the different modes in which the test has been performed.

In the graphs below the p-values are compared, for the different models and the different modes of performing the χ^2 test. This is a more reliable way to compare the obtained results, since it does not depend on the number of degrees of freedom.

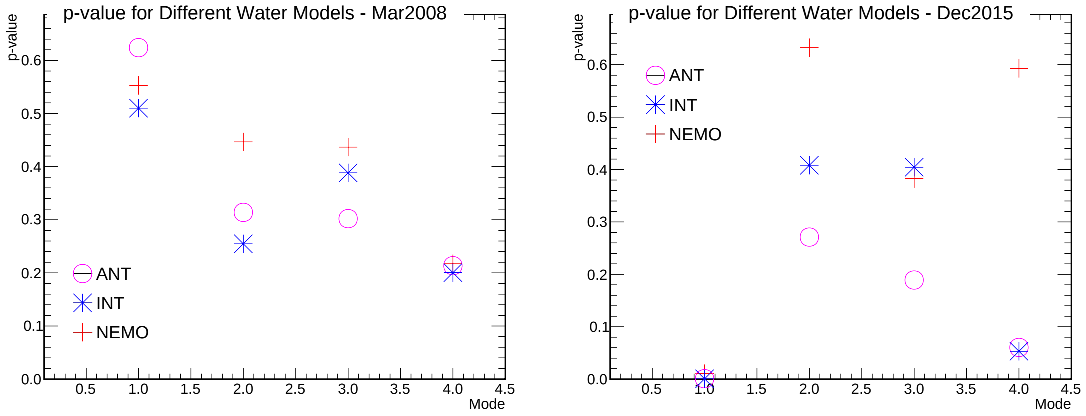

Figure 4.6: p-value as a function of the different modes in which the χ^2 test has been performed, for March 2008 (left) and December 2015 (right).

As can be seen from the graphs above, a part for a few exceptions, *nemo* water seems to be favored with respect to the other models, giving the fact that the p-value in its case is larger than the ones obtained in the other comparisons. This result is in agreement with other internal studies, confirming that *nemo* model describes in the best way the water properties at ANTARES site.

As an additional test, the total normalization of the histograms have been compared. The ratio between the total integrals of data and MC plots, N_{data}/N_{MC}, has then been computed. In the table below these results are illustrated.

Method	*antares*	*intermediate*	*nemo*
N_{data}/N_{MC} (Mar2008)	1.64	1.23	0.83
N_{data}/N_{MC} (Dec2015)	2.30	1.46	1.15

Table 4.3: Ratio between the total integrals of data and MC histograms, after normalizing the MC one with the ratio between the number of selected events and the total run duration of data and MC.

The results in the table above clearly show that, while for *nemo* water the ratio of the integrals is always within the uncertainties of the flux normalization ($\sim 30\%$), this is not the case for the other two models, for which in some cases the value lays outside this range. This conclusion is in agreement with other studies, and hints to a uniformity of water properties between the different neutrino telescope sites in the Mediterranean area.

The analyses on atmospheric neutrino oscillations which will be presented in Chapter 6 and 7 have been done using the most up-dated version of the ANTARES MC chain, which takes as input the *nemo* water model.

4.5 Event detection

The last step of the MC chain is the simulation of the detector response. This is performed through a dedicated program, called *TriggerEfficiency* and developed within the ANTARES Collaboration, which converts the output of the propagation stage to the same format as actual raw data, and applies the identical trigger configurations and readout chain used for the particular data run one has to simulate. At this step, also the individual OM efficiencies, calculated as described in Chapter 3, have to be taken into account.

After this stage, data and MC runs can be treated practically in the same way by the user for further analysis.

Chapter 5

Event reconstruction and selection

In this Chapter the different reconstruction algorithms employed in the various analyses presented in this thesis are described, together with the quality cuts applied in order to obtain a final event sample as pure as possible. After a brief description of the three track reconstruction procedures used, the neutrino energy estimation is presented and the event selection is described.

5.1 Signal and background

As seen in Chapter 2, deep inelastic scattering processes are the most common interactions expected for neutrinos of energies above 20 GeV. Among these interactions, what would constitute, ideally, the final sample for our analyses, are muon neutrinos CC reactions, which result in the production of highly relativistic secondary muons with a clear track detectable within the ANTARES instrumented volume. By reconstructing the direction and the energy of the secondary muon, one can estimate the corresponding direction and energy of the incoming neutrino, and use these observables to constrain the atmospheric neutrino oscillation parameters.

In addition to the very small neutrino cross section, one has to face also the background, namely events which can be misidentified as neutrino CC interactions, resulting in a contamination of the final event sample. The main source of background is represented by atmospheric muons entering the detector from above. These events are, of course, down-going, but sometimes they are wrongly reconstructed as coming from the other hemisphere. These events are in general very energetic muons, which can deeply penetrate through sea water and release only a small fraction of their energy inside the detector. Another event topology which can be sometimes selected as *signal-like* is the one resulting from interactions of electronic neutrinos, both CC and NC, as well as NC interactions of all flavours. Events of these kinds produce hadronic and electromagnetic showers in the detector; particularly bright events can deposit enough light within the detector to be well reconstructed as tracks.

5.2 Track reconstruction algorithms

In this Section three different track reconstruction algorithms are presented, namely *BBFit*, *GridFit* and *AAFit*. The first two have been employed to reconstruct the direction of the incoming neutrino events for the standard oscillation analysis, which will be discussed in detail in Chapter 6, as well as for the sterile neutrino studies, which will be presented in Chapter 7. Both these analyses focus on events at energies of a few tens of GeV, which is where *BBFit* and *GridFit* perform at their best (see Figure 5.9). The third reconstruction algorithm, instead, has been optimized for high energy events (see Figure 5.10); for this reason it has been employed in the study we performed to constrain sterile neutrino parameters in the energy range of $\sim 10^3\,\mathrm{GeV}$ (see Chapter 7). On the other hand, *AAFit* has also been used in the event selection for all the three analyses, as will be illustrated in Section 5.4.

5.2.1 BBFit

BBFit has been developed as a fast algorithm to reconstruct up-going neutrino-induced muons and reject the background of down-going atmospheric muons; it is particularly well-suited for real time applications such as online monitoring and triggering of optical follow-up observations for multi-messenger studies.

The first steps of *BBFit* relies on two main approximations of the ANTARES detector geometry: the detection lines are considered to be perfectly vertical, ignoring possible distortions due to sea currents; the signals recorded by OMs in the same storey are merged, so each storey is considered as a global single OM. This is done to obtain a fast online reconstruction. For offline analyses a further step is added, in which the full detector geometry is taken into account.

A set of hits is selected, based on time causality conditions, and only events with more than five hits are accepted. All merged hits with a charge larger than 2.5 p.e. are called *L1* hits. A *T3* is then defined as the coincidence of two of these *L1* hits within 80 ns for adjacent, and within 160 ns for next-to-adjacent floors. Additional compatible hits are searched for in the adjacent and next-to-adjacent floor of one with a recorded *T3* hit. If all the selected hits have been recorded in the same detection line, a *single-line* (SL) fit is applied, otherwise a *multi-line* (ML) fit procedure is followed. The function to be minimized is:

$$Q = \sum_{i=1}^{N_{hits}} [\frac{(t_\gamma - t_i)^2}{\sigma_i^2} + \frac{A(a_i)D(d_\gamma)}{< a > d_0}] \tag{5.1}$$

where the first term of the sum contains the difference between the hit time, t_i and the expected hit time, t_γ, divided by the time error, σ_i; while, the second term is a penalty term for hits with a large charge but at large distance from the assumed track. In particular, a_i is the hit charge, d_γ the photon traveled distance, $< a >$ is the average hit charge, which compensates the fact that more energetic events leave more light at the same distance; $A(a_i)$ and $D(d_\gamma)$ are two saturation functions, which avoids an excessive pull of the fitted trajectory for hits with large charge and close to the line, respectively; d_0 balances the weight between the two terms and is chosen to be 50 m.

A quality parameter useful to discriminate between well and badly reconstructed events is given by:

$$\bar{Q} = \frac{Q}{dof} \tag{5.2}$$

where *dof* is the number of degrees of freedom in the fit, which corresponds to the number of the hits used in the fit minus the fitted parameters. The distribution of $\bar{Q}$ for a sample of reconstructed up-going neutrinos and misreconstructed up-going atmospheric muons can be seen in Figure 5.1.

The median of the angular error compared to the true neutrino-induced muon direction is of 0.4° for the atmospheric neutrino energy spectrum. For all the details regarding the hit selection and the fitting performed by *BBFit*, see [128].

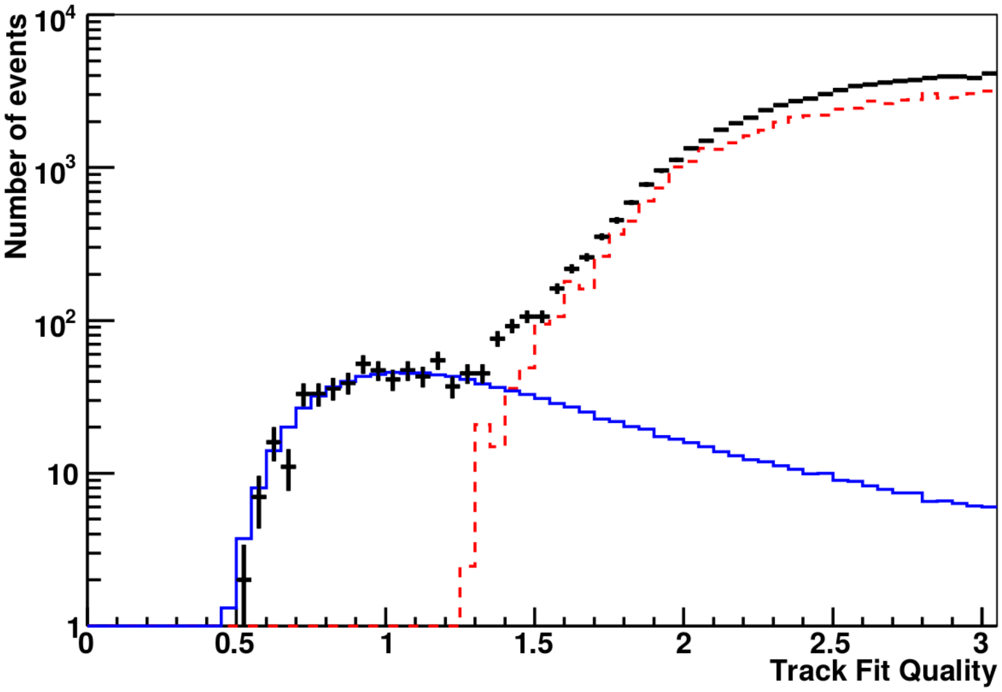

Figure 5.1: Distribution of *BBFit* quality parameter $\bar{Q}$ for all upward reconstructed ML tracks for 2008 data (points with error bars) compared to a MC sample of downward-going atmospheric muons (dashed histogram) and upward-going atmospheric neutrinos (solid histogram) [128].

5.2.2 AAFit

The *AAFit* consists in a chain of subsequent fits, where the first steps provide the starting values for the following ones. A first hit selection is performed, based on charge and hits local coincidence, and a linear fit is done. This provides a first rough estimation of the muon track to be used as starting point in the next steps.

A subsequent hit selection, based on time residual distribution with respect to the prefit result, is performed, and, if more than 15 hits are selected, an M-estimator fit is done, in order to improve the angular resolution. The third step consists in a *maximum-likelihood* fit, which uses as starting point the result of the M-estimator. These last two steps are repeated 8 times, rotating and translating the initial track found by the prefit, in such a way to enhance the probability of falling in the global minimum.

A final ML fit is performed at the end, using a more precise PDF with respect to the previous steps, which takes into account the information on the optical background as well as the charge of the selected hits.

As the $\bar{Q}$ for *BBFit*, one can define a quality parameter for *AAFit*, which helps in discriminating between well and poorly reconstructed events:

$$\Lambda = \frac{\log L_{max}}{N_{hits} - 5} + 0.1 \cdot (N_{comp} - 1) \tag{5.3}$$

where L_{max} and N_{hits} are the maximum likelihood and the number of hits used in the final fit, respectively; while N_{comp} is the number of tracks which give the same direction within 1° compared to the selected track.

Another parameter, which can be used for further event selection steps, is the angular error estimation, written as:

$$\beta_{AA} = \sqrt{\sin^2(\theta)\sigma_\phi^2 + \sigma_\theta^2} \tag{5.4}$$

where θ is the estimated zenith angle, while σ_ϕ^2 and σ_θ^2 are the error on the estimated azimuth and zenith angles, respectively. In Figure 5.2 the distribution of Λ is shown, both for atmospheric neutrinos and atmospheric muons reconstructed as upgoing. For a more detailed description of the *AAFit* track reconstruction algorithm, see [129].

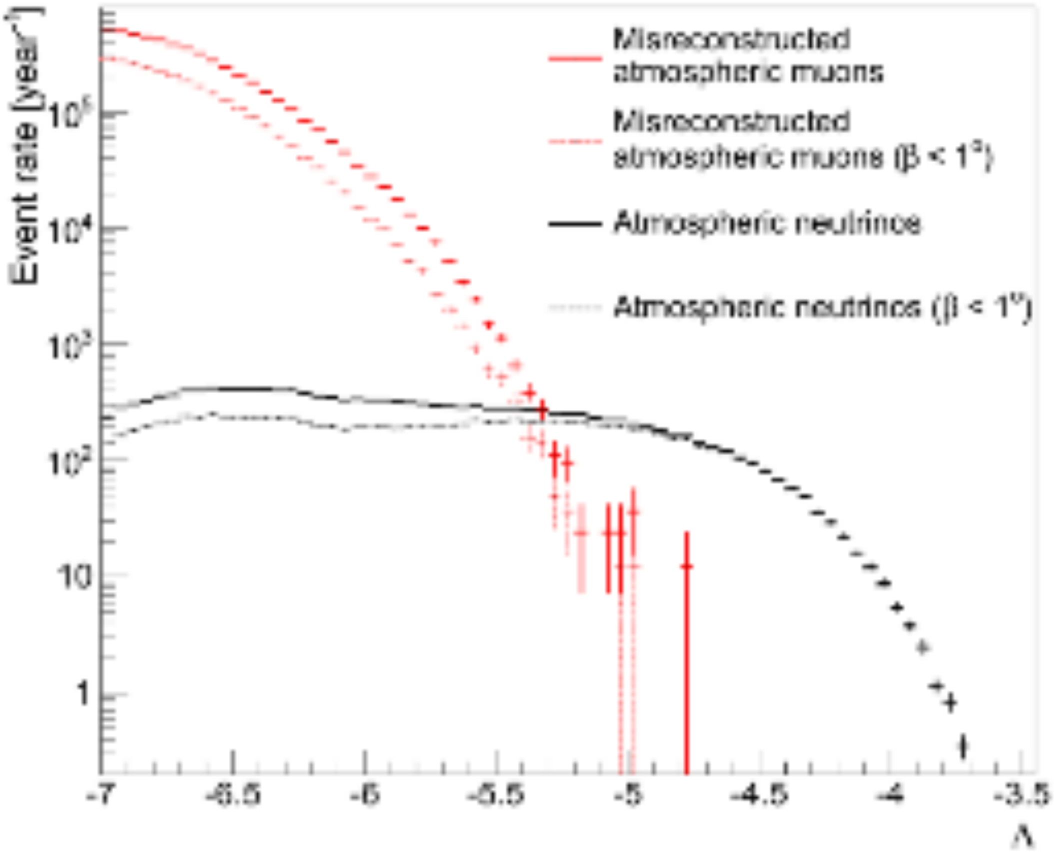

Figure 5.2: Distributions of the Λ variable of *AAFit* for events reconstructed as up-going: atmospheric neutrinos (black) and misreconstructed atmospheric muons (red). An additional cut in β_{AA} has also been applied (softer points) [130].

5.2.3 GridFit

As *AAFit*, also *GridFit* consists in a chain of fits, aimed to improve at each step the track estimation. Starting from a *Cluster Hit Selection*, described in [131], a first prefit, based on the scan of the whole sky with a given number of isotropically distributed directions, is performed. A total of 5000 directions are tested and the best 9 are used as multiple starting points for the final likelihood fit. This first reconstruction stage takes around 300 ms per event, which is larger than for the other two methods. For this reason, a first selection is done, in order to reconstruct only events which are more likely to be neutrino candidates, and exclude the ones which are with higher probability atmospheric muons. The selection is based on the quantity:

$$R = \frac{\sum_{UP} N_{hits,i}}{\sum_{DOWN} N_{hits,i}} \tag{5.5}$$

where the sums $\sum_{UP}$ and $\sum_{DOWN}$ are made over all hits selected on all the directions for which the track would be up-going and down-going, respectively. As illustrated in Figure 5.3, for an atmospheric muon, the number of hits for down-going directions is higher than for the one for up-going directions, while for an up-going neutrino the opposite situation occurs. The quantity R, thus, is expected to be smaller than 1 for atmospheric muons and larger than 1 for up-going neutrinos, and then can be used as discriminant between the two kinds of events. In the algorithm, only events with $R > 0.8$ pass to the subsequent steps of the reconstruction.

As seen for *AAFit*, in order to improve the angular resolution obtained with the prefit, an M-estimator fit is performed. A final *maximum-loglikelihood* fit, with the same PDF used in the last fit of the *AAFit* chain, is applied to each of the 9 best track obtained from the prefit, in order to get the conclusive track estimation. For a more detailed description of the *GridFit* reconstruction, see [130].

In addition to the R parameter, which is used as first event selection criteria and will be later employed to discard misrecontruced atmospheric muons, other two parameters are going to be used in order to select the final event sample for our analyses. These are the reduced likelihood, defined as:

$$r \log L = -\frac{\log L_{max}}{N_{hits} - 5} \tag{5.6}$$

and the estimated angular errors, which is defined in a similar way as for *AAFit*, namely:

$$\beta_{Grid} = \sqrt{\sin^2(\theta)\sigma_\theta^2 + \sigma_\phi^2} \tag{5.7}$$

with θ the estimated zenith angle and σ_ϕ^2 and σ_θ^2 being the error on the estimated azimuth and zenith angles, respectively. In Figure 5.4, the distribution of $r \log L$ is shown for events reconstructed as up-going.

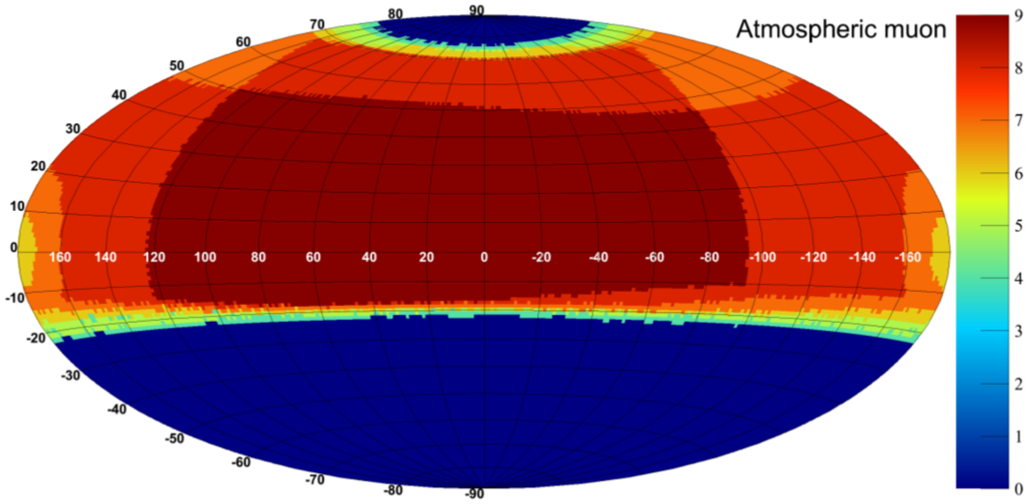

Figure 4.10: Sky-map with the N_{hits} grid for an atmospheric muon.

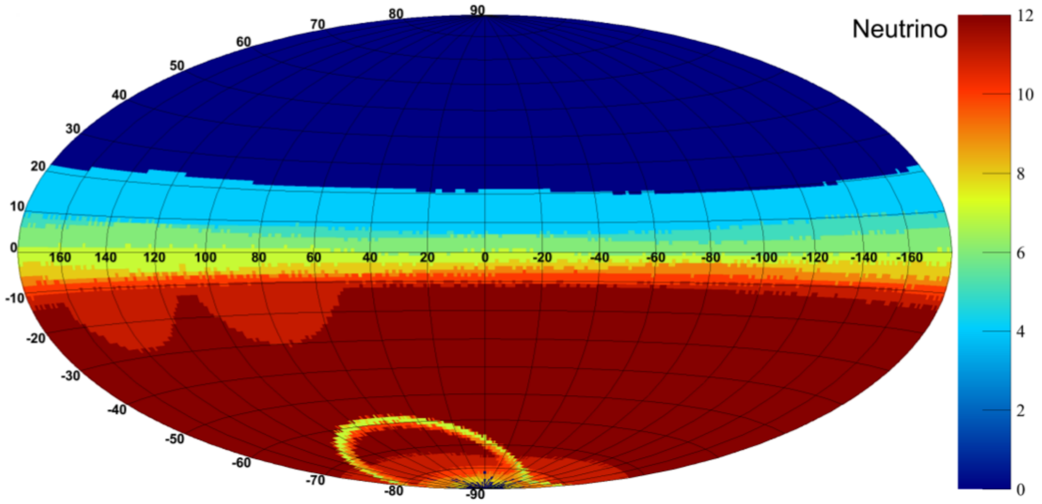

Figure 5.3: Sky maps of N_{hits} in a grid of 500 track candidates. Upper panel: for an atmospheric muon event. Lower Panel: for an up-going neutrino event [130].

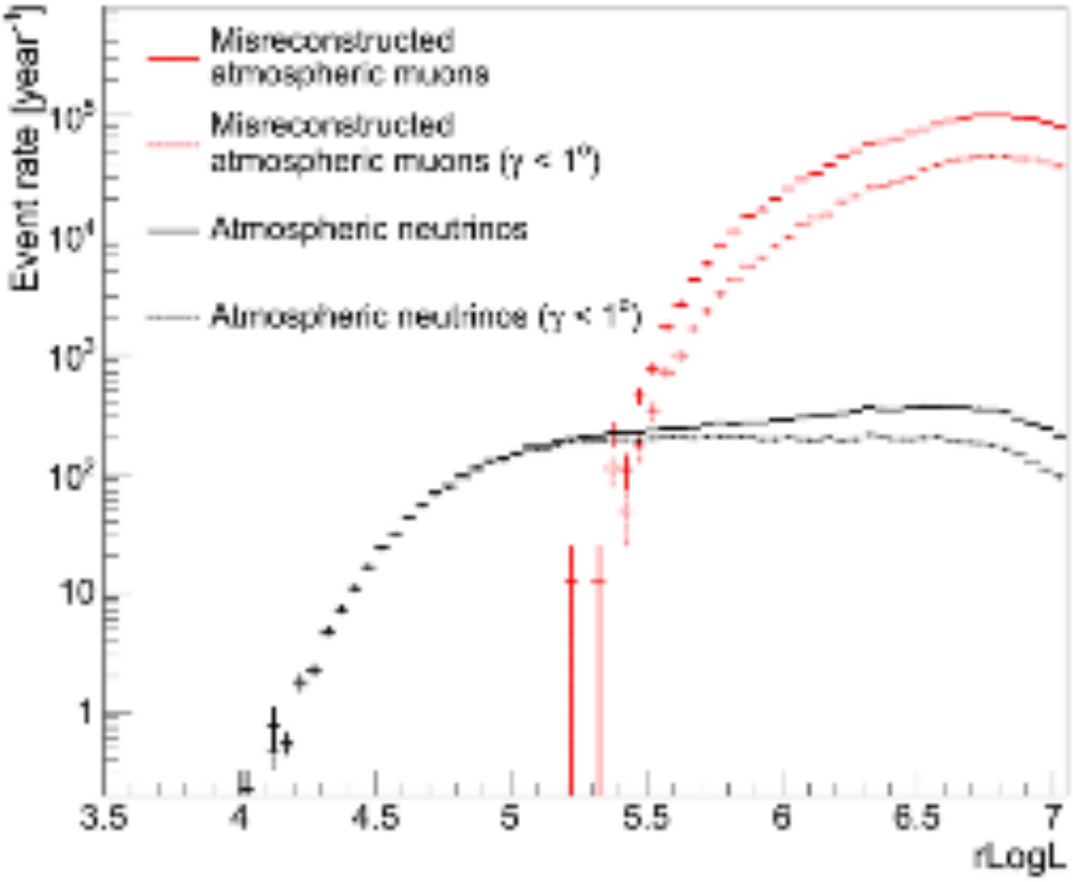

Figure 5.4: Distributions of the $r \log L$ variable of *GridFit* for events reconstructed as up-going: atmospheric neutrinos (black) and misreconstructed atmospheric muons (red). An additional cut in β_{Grid} (γ in the figure) has also been applied (softer points) [130].

5.3 Neutrino energy estimation

Once the direction of the muon produced by neutrino CC interactions in sea water is reconstructed, the next step is the estimation of the energy of the incoming neutrino. This is done in two different ways, depending on the energy of the events we want to select for our analysis. In the following Chapters three different studies will be presented: the *standard* atmospheric oscillation analysis (see Chapter 6) and the sterile analysis in the *low energy* range (see Chapter 7) focus on events with energies of a few tens of GeV, and the same event sample has been used for both of them; on the other hand, the sterile analysis at *high energy* (see again Chapter 7) is aimed to study events of around 10^3 GeV, thus a dedicated high-energy selection has been applied for it. In the following discussions, we are going to refer to the first set of events as the *low energy sample* and to the second one as the *high energy sample*.

5.3.1 Neutrino energy for the *low energy sample*

The neutrino energy estimation for the *low energy sample* is based on the fact that muons produced by neutrinos of a few GeV can be treated as minimum ionizing particles, and their energy can be estimated by their track length, L_μ:

$$E_\mu = L_\mu \times 0.2\,\mathrm{GeV/m} \tag{5.8}$$

where the factor 0.2 GeV/m represents the energy loss of muons in sea water [15]. In order to compute the muon track length one has first to compute the starting and stopping point in the detector. This is done in two separate ways, depending whether the event has been classified as a *single-line* (SL) event or as a *multi-line* (ML) event. In the first case, the z-coordinate of the storey which has recorded the first hit and the one with the last hit are chosen as estimation for the two extreme track points, z_{min} and z_{max}, respectively, and the muon track length is computed as:

$$L_\mu = (z_{max} - z_{min})/\cos\theta \tag{5.9}$$

where θ is the reconstructed zenith angle.

If the event is reconstructed as ML, then also the azimuth angle is uniquely determined, and this allows to project back to the track the Cherenkov photons recorded by the OMs, in order to have an estimation of the starting and stopping points on the muon track. The hits are chosen starting from the ones selected by the corresponding track reconstruction procedure and applying a further selection based on the time residual with respect to the track and on the distance between the OM in which the hit has been recorded and the track. A schematic representation of such a procedure is illustrated in Figure 5.5. In this case the muon track length can be computed by the difference between the two obtained vectors:

$$L_\mu = \sqrt{(x_l - x_f)^2 + (y_l - y_f)^2 + (z_l - z_f)^2} \tag{5.10}$$

where the (x_f, y_f, z_f) and (x_l, y_l, z_l) are the spatial coordinates of the first and last track point, respectively.

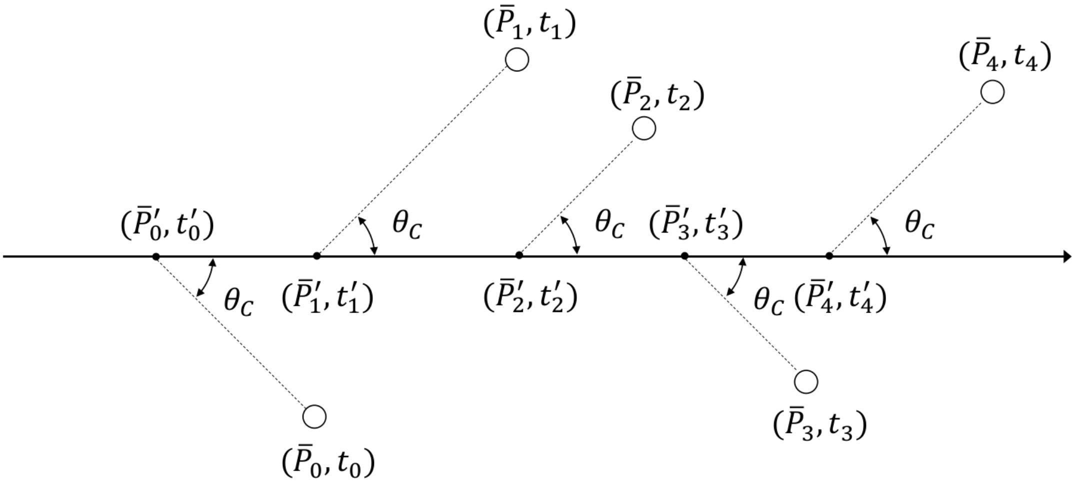

Figure 5.5: Schematic representation of the Cherenkov photons projection along the muon track [53].

The muon energy computed after the track length derivation has been used as neutrino energy estimator. Several attempts have been made in order to improve the energy estimation, from taking into account the hadronic component of the event, to looking for a possible correlation between true neutrino energy and reconstructed variables, but none of them brought to better results in terms of energy resolution. The reason is mainly due to the sparse ANTARES detector layout, in particular the large horizontally spacing among the detection lines.

5.3.2 Neutrino energy for the *high energy sample*

For higher energetic muons, the energy loss in sea water is strongly correlated with the particle energy (see Figure 5.6).

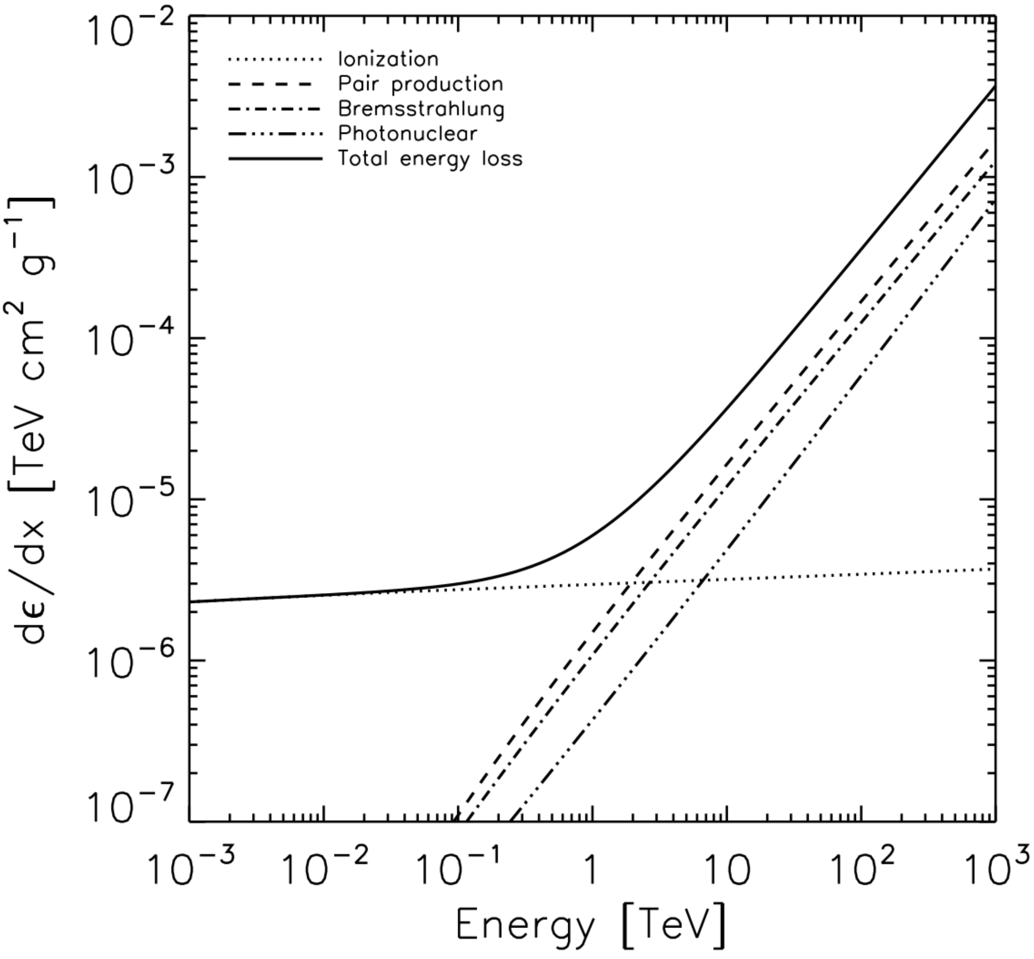

Figure 5.6: Theoretical predictions of the different contributions to the energy loss of high energy muons in water. The total energy loss (solid line) is decomposed into contributions from different processes, indicated in the legend [132].

The algorithm used for the neutrino energy estimation of the *high energy sample* is based on this theoretical expectation. The total deposited muon energy, dE/dX, is estimated, on an event-by-event basis, by the parameter ρ, which can be written as:

$$dE/dX \sim \rho = \frac{\sum_i^{N_{hits}} Q_i}{\epsilon(\overrightarrow{x})} \frac{1}{L_\mu(\overrightarrow{x})} \tag{5.11}$$

where Q_i is the charge recorded by the OM i, $\epsilon(\overrightarrow{x})$ is the light detection efficiency, L_μ is the muon track length within a sensitive volume, equal to the ANTARES instrumented volume extended by twice the attenuation length ($\lambda_{att} = 55\,\mathrm{m}$), and $\overrightarrow{x}$ is the muon track direction. The light detection efficiency depends on the position and direction of the muon track, and can be written as:

$$\epsilon(\overrightarrow{x}) = \sum_i^{N_{OMs}} \exp(-\frac{r_i}{\lambda_{abs}}) \cdot (\frac{\alpha_i(\theta_i)}{r_i}) \tag{5.12}$$

where the sum runs over all the OMs active at the time of the event, r_i is the distance between the OM i and the muon track, λ_{abs} is the absorption length and $\alpha_i(\theta_i)$ takes into account the angular acceptance of the OM i.

MC simulations have been used to correlate the quantity dE/dX, obtained through Equation 5.11, with the true neutrino energy. Averaging over small bins in dE/dX, final calibration tables have been obtained. An example of the correlation distribution is given in Figure 5.7. For a more detailed description of the algorithm, see [133].

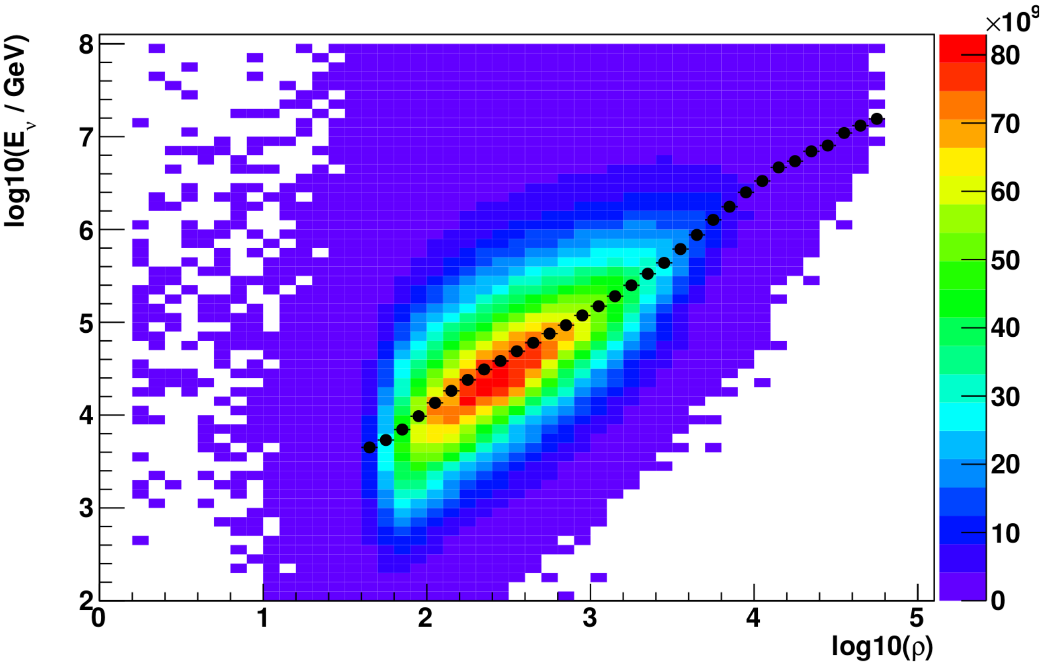

Figure 5.7: The correlation between the reconstructed dE/dX and the true energy is used to calibrate the energy estimator. The black markers denotes the derived calibration table, i.e. the average true energy per dE/dX bin [133].

5.4 Event selection

In this Section the quality cuts are described, in order to obtain a final event sample. As for the neutrino energy estimation, the discussion will be divided accordingly to the two event sets used in the analyses.

5.4.1 Event selection for the *low energy sample*

As described in the Section 5.2, the track reconstruction algorithms which perform their best at low energy are *BBFit* and *GridFit*. The previous oscillation analysis done by the ANTARES Collaboration [47] relied only on *BBFit*; however, a, small but not negligible, percentage of events which would be discarded by basic

BBFit quality cuts, is, instead, reasonably well reconstructed by *GridFit*. For this reason, it has been decided to combine the two reconstruction procedures, in order to increase the statistics of the final sample. On the other hand, since *GridFit*, by construction, does not divide events in *single-line* and *multi-line*, and the importance of the *single-line* events for the oscillation signal has been underlined in the first published analysis (see again [47]), the selection proceeds as follows:

- Events which pass the quality cuts for *BBFit* are selected as *BBFit SL* or *ML* events;
- If the event does not pass the selection criteria for *BBFit*, but it passes that of *GridFit*, then is kept as *GridFit* event;
- Events which do not pass neither the *BBFit* selection nor the *GridFit* one are discarded.

Four different sets of quality criteria have been tested before un-blinding, and the best one in terms of expected sensitivity to the neutrino oscillation parameters has been chosen (see Chapter 6). In the following we are going to refer to these different sets of cuts as *cut 1*, *cut 2*, *cut 3* and *cut 4*.
Let us now, entering the details of the event selection for the two reconstruction procedures.

BBFit event selection

The selection for reconstructed *BBFit* events has been done starting from the one performed in the previous ANTARES oscillation analysis [47], trying to optimize the signal events but still keeping the background under control. The selection is slightly different for SL and ML events, but it is generally based on the quality parameter $\bar{Q}$, defined in 5.2.1, on the number of storeys in which hits for the final track fit have been recorded, and on a containment condition. Furthermore, when an event has been reconstructed also by *GridFit* or *AAFit* or both, the different values of the reconstructed zenith angle obtained by the various procedures are required to be in a certain agreement, namely $|\cos\theta_i - \cos\theta_j| < 0.15$, where i and j denotes the reconstructed zenith for procedure i and j, respectively. If the event is not reconstructed by the other procedures, this cut is not applied. For *cut 2*, *cut 3* and *cut 4* an additional condition on Λ (see 5.2.2) is required. This cut is applied in a softer way compared to the standard value used to select higher energy events (see Section 5.4.2). In this way, one can benefit from this selection to reduce the background without loosing too many events in the energy range we are interested in.

The first step of the selection consists in requiring that the event is reconstructed as up-going by *BBFit* and by the other two reconstruction procedures, in case the reconstruction succeeded also for them. This cut allows to discard a large fraction of the background of atmospheric muons, which are, of course, down-going, and is the starting point for all the tested sets of selection criteria. However, some of the background events are wrongly reconstructed as up-going by the track algorithms, making additional quality cuts needed. As seen in 5.2.1, the quality of the fit helps discriminating between well and poorly reconstructed events. Well reconstructed neutrino events tend to have a fit quality parameter smaller than the one for misreconstructed atmospheric muons. In particular, for our analysis, a cut at $\bar{Q} = 0.8$ and $\bar{Q} = 1.3$ has been chosen, for SL and ML events, respectively, discarding all events with a quality parameter larger than the cut value.

BBFit proceeds with a SL track fit only if hits in at least 4 storeys are found, and with a ML fit only when at least 5 storeys with selected hits are found. An additional cut on the number of storeys has been applied, in order to reduce the contamination from misrecontructed atmospheric muons. For both SL and ML events a minimum number of 5 storeys is then required.

A containment condition is also applied for the ML events, in order to avoid events for which the interaction vertex has been reconstructed very far away from the detector volume. For these events, the reconstructed vertex has been asked to lay within a cube of 170 m side around the detector center. More stringent containment conditions have been found to reduce considerably the number of selected events, without significantly improving the energy resolution, thus have been abandoned.

The difference among the four sets of quality criteria tested lays on the cut on the reconstructed zenith angle for ML events, $\cos\theta_{BB,ML}$ and on the use of the Λ parameter as additional quality cut.

- *cut 1*: $\cos\theta_{BB,ML} > 0.15$, no cut on Λ;
- *cut 2*: $\cos\theta_{BB,ML} > 0.00$, $\Lambda > -6.5$;

- *cut 3*: $\cos\theta_{BB,ML} > 0.15$, $\Lambda > -6.5$;
- *cut 4*: $\cos\theta_{BB,ML} > 0.15$, $\Lambda > -6.0$.

***GridFit* event selection**

Events which have been discarded by the *BBFit* selection are passed to the *GridFit* one. The first step of the selection consists in requiring that the event is reconstructed as up-going by *GridFit*, and, in order to reduce further the atmospheric muon contamination close to the horizon, a more stringent cut is applied, namely $\cos\theta_{Grid} > 0.2$. In the case the reconstruction succeeded also for the other two reconstruction procedures, the different values of the reconstructed zenith angle obtained by the various procedures are required to be in a certain agreement, namely $|\cos\theta_i - \cos\theta_j| < 0.2$, where i and j denotes the reconstructed zenith for procedure i and j, respectively. If the event is not reconstructed by the other procedures, this cut is not applied. The same containment condition applied for the *BBFit* ML events are used here. The other cuts are based on the quality parameters of *GridFit*. As starting point the event selection criteria found in [130] have been tested and optimized in order to obtain a good signal/noise ratio. In particular it has been required, with a logic *or* condition:

- R > 3.50, $\beta_{Grid} < 2.0$, rLogL < 5.8
- R > 1.65, $\beta_{Grid} < 1.0$, rLogL < 6.2

An additional cut has been applied on the number of hits selected for the final track fit. This cut has been found to help in reducing the background of misreconstructed atmospheric muons that, in general, deposit more energy than few GeV neutrinos, in the detector. For this reason events with a total number of selected hits higher than 45 have been discarded.

The difference among the four sets of quality criteria tested lays on the use of the Λ parameter as additional quality cut.

- *cut 1*: no cut on Λ;
- *cut 2*: $\Lambda > -7.0$;
- *cut 3*: equal to *cut 2*;

- *cut 4*: $\Lambda > -6.0$.

MC event sample after selection

The different quality selection criteria have been tested both in terms of energy resolution and background reduction, as well as expected number of signal events. In Figure 5.8 the energy resolution for MC ν_μ and $\bar{\nu}_\mu$ CC events with true energy below 100 GeV is shown for all four sets of selection criteria.

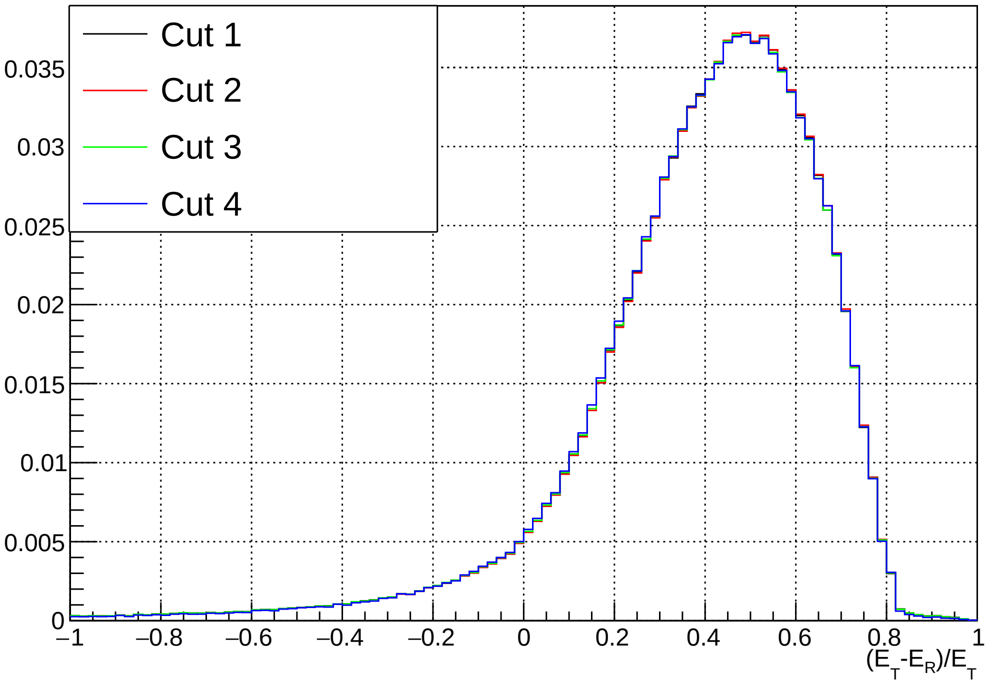

Figure 5.8: Energy resolution for MC ν_μ and $\bar{\nu}_\mu$ CC events with true energy below 100 GeV. E_T is the true neutrino energy, while E_R is the reconstructed one. Different colors stand for different sets of event selection criteria. The distributions have been normalized to one.

As previously said, the neutrino energy estimator is taken from the reconstructed muon energy, which in turn is computed from the muon track length in the detector. The hadronic component of the interaction is missing when reconstructing the neutrino energy in this way. Moreover, the majority of the muons traversing the detector deposits only a small fraction of their energy within the instrumented volume. These are the reasons why a deviation from zero is observed in the figure. The energy resolution obtained in this way is compatible with what was found by the previous ANTARES oscillation analysis [47].

As can be seen from the figure, in terms of energy resolution all the sets of cuts perform basically in the same way, so one cannot decide which one to keep based only on this quantity. In terms of expected neutrino signal, instead, one could look at the true energy distribution of MC ν_μ and $\bar{\nu}_\mu$ CC events. This quantity is shown in Figure 5.9 and in Table 5.1, for all the different sets of selection criteria.

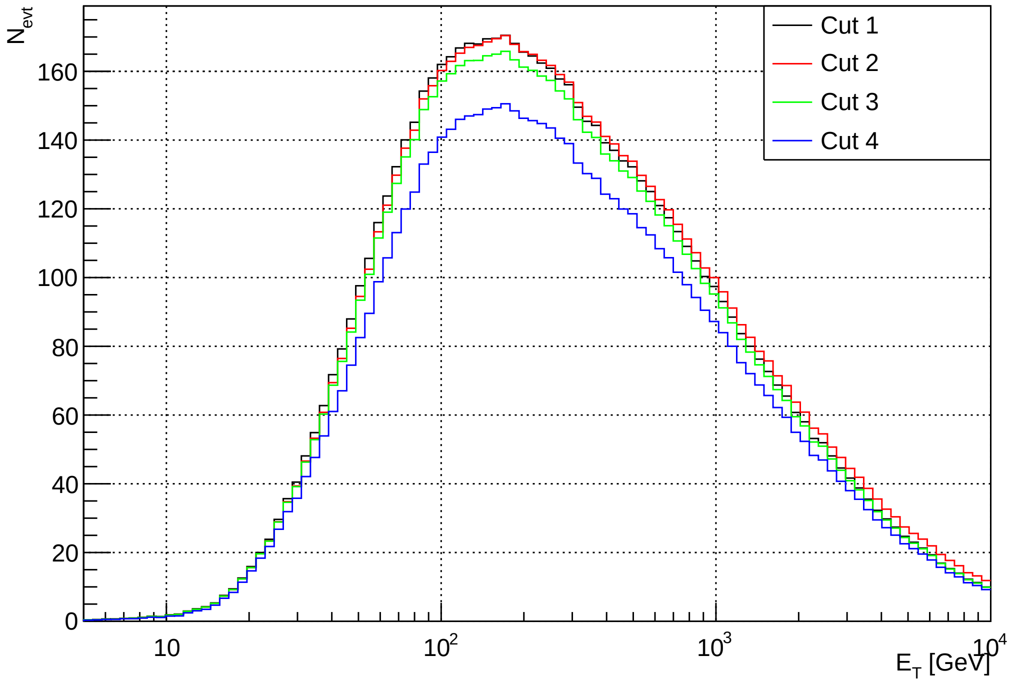

Figure 5.9: True energy distribution for MC ν_μ and $\bar{\nu}_\mu$ CC events. Different colors stand for different sets of event selection criteria. The total number of expected events over the whole lifetime of data considered is also shown.

The number of expected events over the whole considered lifetime of data, which amounts to 2830 days (see Chapter 6 for details), is also shown in Table 5.1. This number has been computed weighting the MC events without assuming neutrino oscillations. However, the strength of the signal is given by the difference between this quantity and the number of events we would expect due to neutrino oscillations. This quantity, estimated over the whole lifetime of the analysis, is reported in Table 5.1 for all the sets of selection criteria. In this case, a simple 2-flavour oscillation model is used to weight the MC ν_μ and $\bar{\nu}_\mu$ CC events, with $\Delta m^2_{32} = 2.46 \times 10^{-3}\,\mathrm{eV}^2$ and $\theta_{23} = 41.38°$.

The quality selection criteria have to be checked also against the background, in order to ensure that this is actually reduced by the cuts and kept under control with respect to the signal we want to measure. The number of MC NC events, as well as ν_e and $\bar{\nu}_e$ CC events, which pass the various selection criteria are found to be at the level of 0.5% (see Table 5.1).

The main source of background, which one should try to keep under control, is represented by the misreconstructed atmospheric muons. As seen in the previous chapter, only 1/3 of the atmospheric muons are actually simulated. In Table 5.1 the total number of expected atmospheric muons, after event selection, is shown as well, for all the four sets of selection criteria. The errors reflect the used MC statistics.

Cut	$\nu_\mu + \bar{\nu}_\mu$ CC	Atm μ	$\nu_e + \bar{\nu}_e$ CC + NC	Signal Strength
1	7591.4 ± 5.5	351.0 ± 32.4	39.3 ± 0.2	716.4 ± 7.6
2	7656.1 ± 5.6	357.6 ± 32.7	38.4 ± 0.2	700.8 ± 7.7
3	7389.7 ± 5.5	311.0 ± 30.5	38.4 ± 0.2	700.7 ± 7.5
4	6718.1 ± 5.2	232.4 ± 26.4	32.3 ± 0.2	648.1 ± 7.1

Table 5.1: Expected number of $\nu_\mu + \bar{\nu}_\mu$ CC events, misreconstructed atmospheric muons, $\nu_e + \bar{\nu}_e$ CC plus NC events of all flavours, and strength of the expected oscillation signal over the whole lifetime of the analysis (2830 days), for the different sets of quality selection criteria.

5.4.2 Event selection for the *high energy sample*

For the *high energy sample* selection, events which have been well reconstructed as up-going by *AAFit* are kept. The quality of the reconstruction is based on the values of the two main parameters defined in 5.2.2, namely Λ and β_{AA}. Events with $\Lambda > -5$ and $\beta_{AA} < 1$ are selected, which yield a clean sample of atmospheric $\nu_\mu + \bar{\nu}_\mu$ CC events (see Figure 5.2). In Figure 5.10 the energy distribution of the MC $\nu_\mu + \bar{\nu}_\mu$ CC events after the selection is shown.

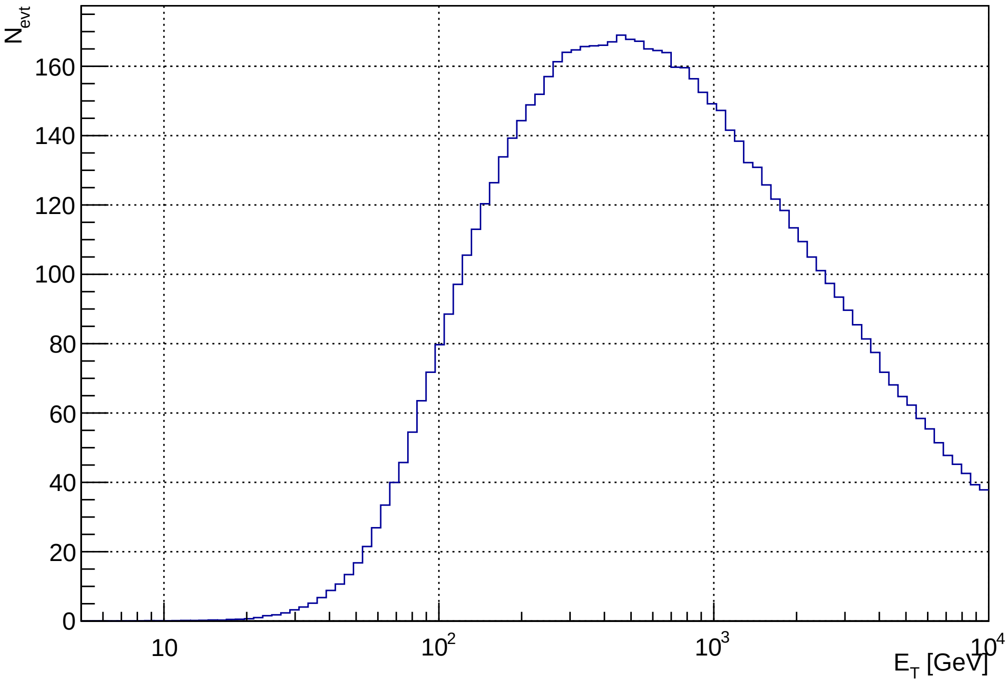

Figure 5.10: True energy distribution for MC $\nu_\mu + \bar{\nu}_\mu$ CC events, which pass the *high energy* selection.

Chapter 6

Measuring the atmospheric neutrino oscillation parameters with ANTARES

In this Chapter the analysis of the ANTARES data in order to constrain the atmospheric neutrino oscillation parameters is presented. After a brief description of the followed minimization procedure, the different sources of systematic effects are illustrated together with their treatment in the analysis. The strategy followed to estimate the total atmospheric muon background is also discussed. Starting from a first sensitivity study, based only on MC simulations and aimed at the optimization of the whole procedure, the final results are presented.

6.1 Method

As seen in Chapter 1, atmospheric neutrino experiments are most sensitive to the mixing angle θ_{23} and the mass splitting Δm^2_{32}. If neutrinos did not oscillate, we would expect to detect the same amount of neutrinos of a certain flavour coming from above as coming from the opposite hemisphere. However, since neutrinos do oscillate and the ones traversing all the Earth have enough time to change their flavour, the expected event rate at our detector is different than the one we would have in absence of oscillations. As seen in the previous Chapter, the applied event selection is aimed at preserving events which come from up-going ν_μ and $\bar{\nu}_\mu$ CC interactions, while discarding the others. After reconstruction, the distribution of energy and direction of the selected events can be evaluated. The number of expected events for a given energy and a given direction will depend on the oscillation parameters.

Through a 2-dimensional minimization procedure, based on the *ROOT* package *Minuit* [126], the distribution of selected data is compared to the one obtained by the MC sample under a certain *oscillation hypothesis*, namely under a set of values of the oscillation parameters.
The whole study has been based on a *log-likelihood* function:

$$\mathcal{L} = -2\log L = 2\sum_{i,j}[N_{i,j}^{MC}(\bar{p},\bar{\eta}) - N_{i,j}^{Data}\cdot\log N_{i,j}^{MC}] + \sum_{k}\frac{(\eta_k - <\eta_k>)^2}{\sigma_{\eta_k}^2} \tag{6.1}$$

where the first sum runs over the histogram bins of reconstructed energy and zenith angle, $N_{i,j}^{Data}$ is the number of data in bin *(i,j)* and $N_{i,j}^{MC}(\bar{p},\bar{\eta})$ the corresponding number of expected MC events in the same bin; this number depends on the set of oscillation parameters, $\bar{p}$, as well as on the set of systematic parameters, $\bar{\eta}$. The second sum, instead, runs over the number of nuisance parameters taken into account, $<\eta_k>$ being the prior knowledge we assume to have on the parameter *k*, and σ_{η_k} its uncertainty. The *Minuit* package minimizes the $\mathcal{L}$ function defined in Equation 6.1, finding the set of parameters which better represents the data set. This approach is equivalent to the standard χ^2 minimization for bins with high statistics, while it represents a more correct treatment of those bins with a small number of entries.

After finding the global minimum, which will be referred to as $\mathcal{L}_{min}$ in the following discussion, one can construct *confidence limits* in a reduced parameter space. Let us call the set of parameters for which $\mathcal{L}_{min}$ has been found as $\bar{p}_{min}$. In our case, confidence regions will be constructed in the parameter space of the two oscillation parameters we would like to constrain, namely θ_{23} and Δm_{32}^2. Assuming, then, that the total number of fitted parameters is *M*, the region of the parameter space within which $\mathcal{L}_\epsilon - \mathcal{L}_{min}$ is smaller than a pre-defined quantity, $\Delta\mathcal{L}$, represents a confidence region around $\bar{p}_{min}$. $\mathcal{L}_\epsilon$ is the value of the $\mathcal{L}$ function in the $\epsilon = M - 2$ space, obtained by minimizing all the *M* parameters except the two in which we want to build the *confidence region*, which should instead be kept fixed. The pre-defined values of $\Delta\mathcal{L}$ can be found tabulated in literature and they depends on the dimension of the parameter space we want the confidence region to be referred to and the level of confidence we require. Commonly used confidence levels are 68%, 90% and 99%, which, for a two reduced parameter space correspond to the values of $\Delta\mathcal{L}$ listed in Table 6.1.

CL	68%	90%	99%
$\Delta\mathcal{L}$	2.30	4.61	9.21

Table 6.1: Reference values for confidence level contours in a 2 parameter space.

As already discussed, the minimization is performed on 2-dimensional histograms in reconstructed energy and zenith angle. For the MC sensitivity study, which will be presented in detail in Section 6.3, all sets of event selection criteria (see Chapter 5) have been tested. Histograms of 8 bins in $\log_{10} E_{reco}$ have been used. A first *underflow* bin contains all events with $\log_{10} E_{reco} < 1.2$, and 7 more bins, equally spaced, are filled with the events up to $E_{reco} = 100\,\mathrm{GeV}$. This choice is motivated by the fact that very low statistic is available for $\log_{10} E_{reco} < 1.2$. In $\cos\theta_{reco}$, instead, 17 bins from 0.15 to 1 have been considered, for *cut 1,3* and *4*; since *cut 2* does not discard *BBFit* ML events close to the horizon, 20 bins in $\cos\theta_{reco}$ from 0 to 1 have been used in this case. An example of such histogram used in the fit can be seen in Figure 6.1, obtained with all the MC events which pass the selection criteria of *cut 1*, and weighted without assuming any neutrino oscillation.

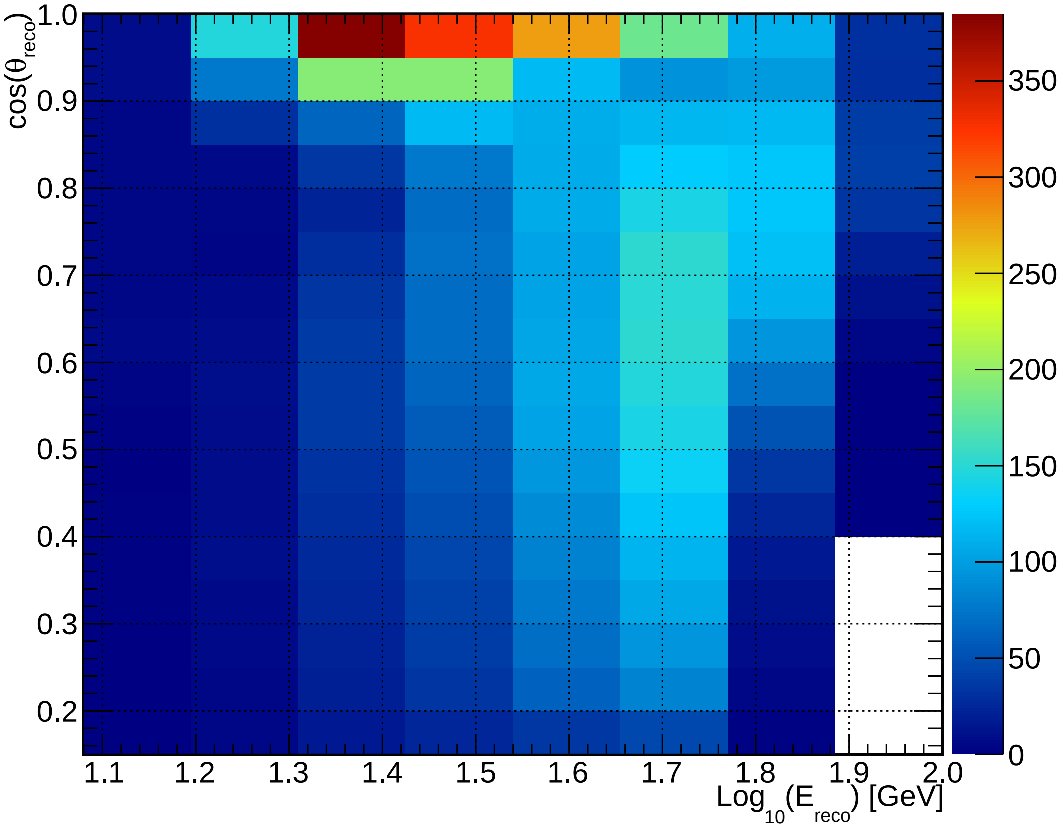

Figure 6.1: Example of reconstructed event histogram. MC events passing the *cut 1* have been used and no neutrino oscillation is assumed.

In order to construct the hypotheses to test, a complete 3-flavour scenario has been considered for the oscillation probabilities. The open source software *OscProb* [134] has been used for the precise computation of atmospheric neutrino oscillation probabilities through the Earth, and the Earth density profile has been parameterized using the *PREM* model [135]. Events have been weighted according to *Honda* atmospheric flux [13], as described in Chapter 1.

6.2 Systematic treatment

In this Section the different sources of systematic effects which have been considered in the analysis will be presented, together with the procedure to include them.

6.2.1 Oscillation related systematic

A part from the oscillation parameters we want to constrain with this analysis, there are other terms which need to be taken into account. In particular, the value of the mixing angle θ_{13} has been fitted as well, but with a prior with mean value and uncertainty equal to the global best fit values reported in 1.4.

The solar neutrino oscillation parameters, namely Δm^2_{21} and θ_{12} mostly affect the electronic channel rather than the muonic one, in which our work is focused; moreover, their effect becomes non negligible only for neutrino energies below 1 GeV, which is well below the ANTARES detectable energy. Thus, these parameters have been kept fixed through all the analysis at their global best fit value. No sensitivity to the CP-violating phase, δ_{CP}, has been encountered through MC studies, thus this parameter has been fixed at zero. Furthermore, a normal mass ordering has been assumed trough all the analysis.

6.2.2 Flux related systematic

As seen in Chapter 1, different sources of error can enter the estimation of the atmospheric neutrino flux, causing both a variation in the total number of expected events, as well as modifications in the energy and angular distributions. In order to account for uncertainties in the neutrino atmospheric flux prediction, different nuisance parameters have been introduced. First, a global normalization factor, N, has been fitted without any priors, in order to account for variations on the yield of the event distribution. The flux model employed in this analysis is the one provided by Honda *et al.* [13] for the Frèjus site, which is equivalent to the one shown in Figure 1.3 for the energy range relevant for our studies. A correction to this value, $\Delta\gamma$, has also been implemented, as a skew to the nominal value and with a prior uncertainty of 0.05. An additional parameter controls the uncertainty $\nu/\bar{\nu}$ on the flux ratio of neutrinos and anti-neutrinos and takes into account also up/horizontal flux asymmetries. Starting from the estimation of such flux ratio uncertainties, performed by Barr *et al.* [14], a parameterization has been developed within the IceCube Collaboration [48]. This parameterization computes the corresponding event weight correction as a function of the neutrino flavour, energy and direction, depending on the value of a nuisance parameter which corresponds to the uncertainty on the flux ratio. The nuisance parameter $\nu/\bar{\nu}$ is measured in number of σ, where 1σ corresponds to the uncertainty given in [14]. In Figure 6.2 and 6.3 the uncertainties on the neutrino-type ratios and on the directional ratios as a function of the neutrino energy are shown, respectively, as computed in [14].

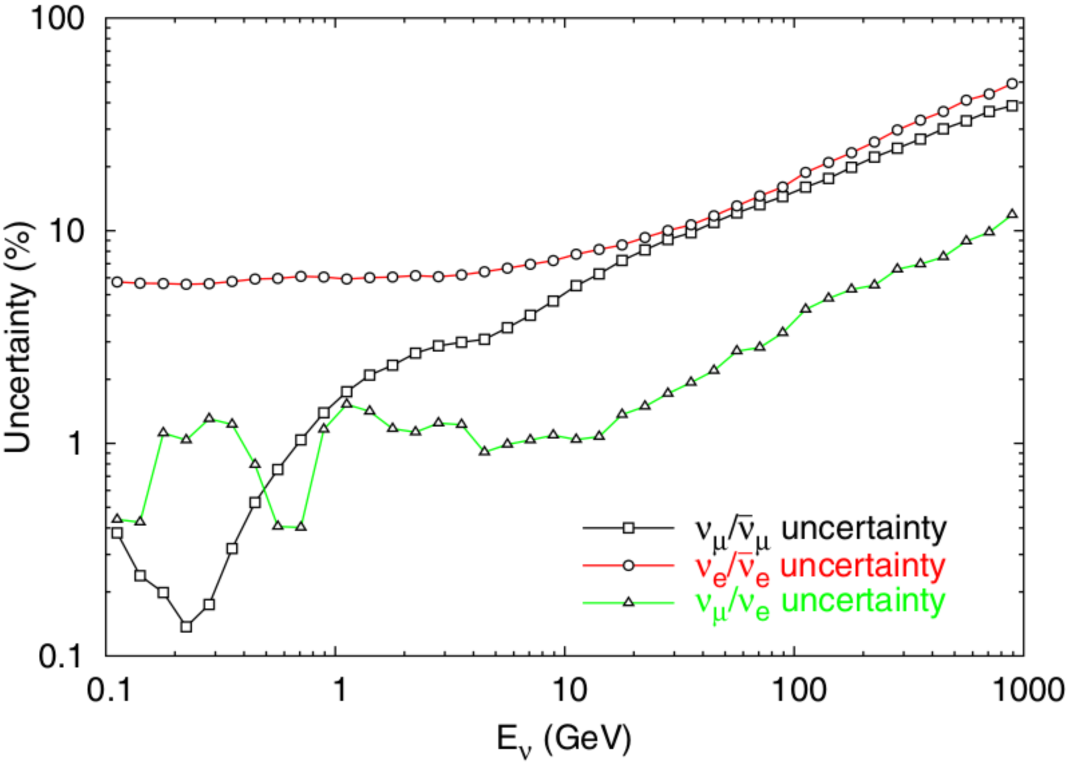

Figure 6.2: Uncertainties in neutrino-type ratios as a function of neutrino energy. $\nu_\mu/\bar{\nu}_\mu$ is shown with black lines with squares, $\nu_e/\bar{\nu}_e$ with red lines with circles and $(\nu_\mu + \bar{\nu}_\mu)/(\nu_e + \bar{\nu}_e)$ with green lines with triangles [14].

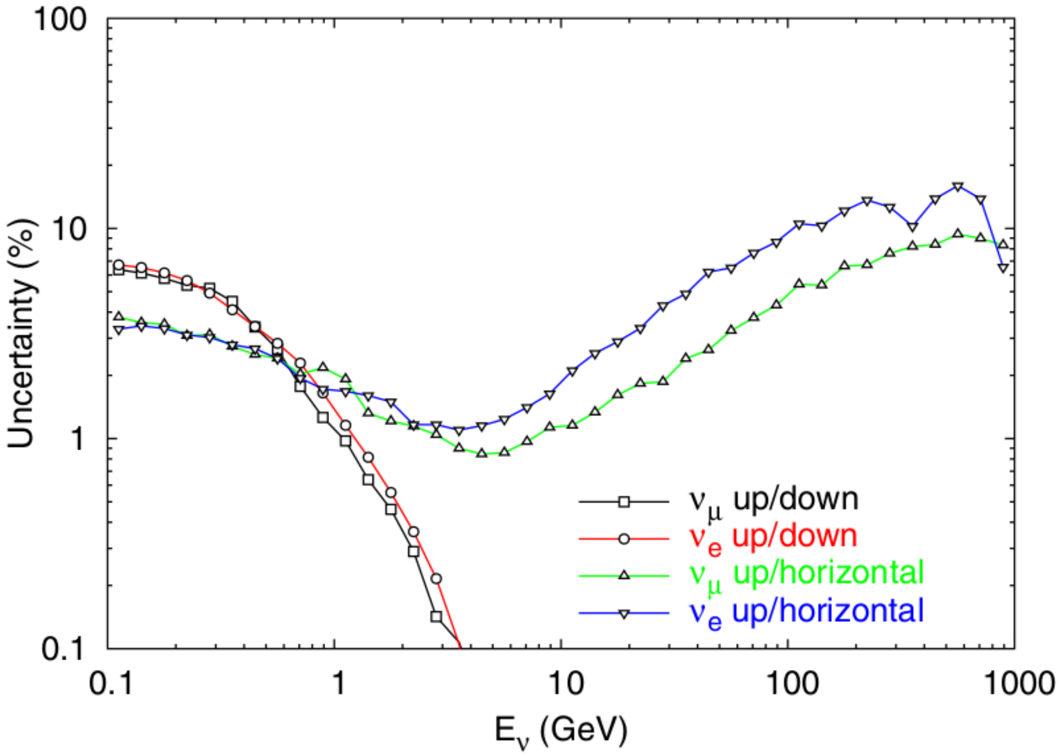

Figure 6.3: Uncertainties in directional ratios as a function of neutrino energy. $\nu_{\mu,up}/\nu_{\mu,down}$ is shown with black lines with squares, $\nu_{e,up}/\nu_{e,down}$ with red lines with circles, $\nu_{\mu,up}/\nu_{\mu,hor}$ with green lines with triangles and $\nu_{e,up}/\nu_{e,hor}$ with blue lines with triangles [14].

6.2.3 Cross section related systematic

As seen in 1.3, at the energy of interest for this study, the neutrino interaction cross section is dominated by *deep inelastic* (DIS) phenomena, with a smaller contribution from *quasi elastic* (QE) and *resonance* (RES) interactions. In *GENHEN* the DIS channel is simulated with *LEPTO* [29], while the other two processes rely on the Rein-Sehgal (RS) model [30].

Uncertainties in the DIS cross section can be incorporated in the global flux normalization factor N, as well as in the correction to the spectral index $\Delta\gamma$.

For what concerns the other processes, uncertainties on the model have been taken into account by a parameterization of the event weight as a function of the true neutrino energy. A special production of ν_μ and $\bar{\nu}_\mu$ CC events has been done with *gSeaGen* [136], which uses *GENIE* [137] to model neutrino interactions, and whose model for non-DIS processes is the same as the one employed in *GENHEN*. The choice of using *GENIE* rather than *GENHEN* is motivated by the fact that the former provides a very intuitive way to propagate neutrino interaction uncertainties, and to correct the event weight accordingly. The dominant systematic, whose effect is not degenerate with the one already taken care by the overall normalization and the spectral index correction, was found to be related to axial mass for CC resonance neutrino production, M_A^{CCRES}. The nominal value for this parameter is 1.12 ± 0.22 GeV. By varying this input parameter by $\pm 1\sigma$, the event weight correction with respect to the nominal one has been computed as a function of the true neutrino energy. The corresponding plots are shown in Figure 6.4 for ν_μ and $\bar{\nu}_\mu$ CC events in the energy range 5-200 GeV.

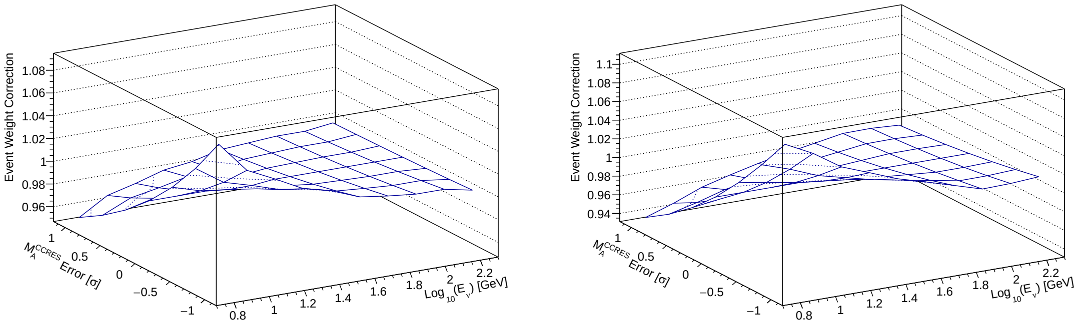

Figure 6.4: Expected event weight corrections as a function of true neutrino energy and of error on M_A^{CCRES}, for ν_μ (left panel) and $\bar{\nu}_\mu$ (right panel) CC events.

A nuisance parameter, X_{sec}, which regulates the uncertainty on M_A^{CCRES}, has been introduced in the analysis. It is measured in number of σ, where 1σ is the nominal uncertainty of 0.22 GeV on this parameter.

6.2.4 Detector related systematic

Two dedicated MC productions have been made with modified optical module photon detection efficiency, accounting for a variation of ±10% from the nominal value. The correction to the event weights has been computed as a function of the neutrino energy for both $\nu_\mu + \bar{\nu}_\mu$ and $\nu_e + \bar{\nu}_e$ CC events, reconstructed as up-going. The resulting distributions have been fitted, in the energy range $10 - 10^3$ GeV, with a function of the form:

$$f(E) = A \cdot E^B \tag{6.2}$$

where E is the true neutrino energy, while A and B the two fitted parameters. Figure 6.5 shows the histograms of the event weight correction as a function of true neutrino energy, together with its parameterization.

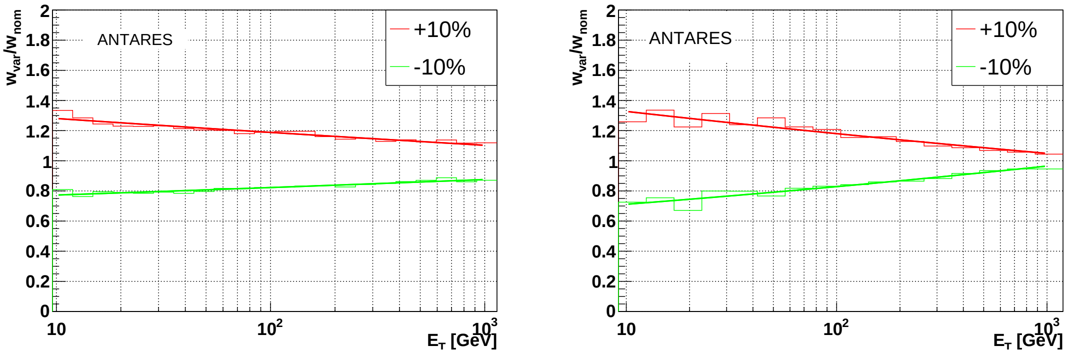

Figure 6.5: Expected event weight corrections as a function of true neutrino energy for a +10% (red) and −10% (green) from the nominal value of the OM photon detection efficiency. Left panel: $\nu_\mu + \bar{\nu}_\mu$ CC events; Left panel: $\nu_e + \bar{\nu}_e$ CC events.

The values of the fitted parameters A and B are listed in Table 6.2.

	$\nu_\mu + \bar{\nu}_\mu$	$\nu_e + \bar{\nu}_e$
+10%	A = 1.34; B = -0.03	A = 1.49; B = -0.05
−10%	A = 0.73; B = 0.03	A = 0.61; B = 0.07

Table 6.2: Fitted values for the parametrization of the event weight correction with a variation of ±10% from the nominal value of the OM photon detection efficiency.

As can be seen from the figures, the distribution is well described by the chosen function. The effects of A and B are taken into account in the minimization procedure by the global normalization factor, N, which is left completely unconstrained, and by the correction to the spectral index, $\Delta\gamma$, respectively.

6.2.5 Water absorption related systematic

In a similar way, in order to account for uncertainties in the water absorption length, two dedicated MC productions have been made, assuming a variation of ±10% from the nominal value of this parameter, keeping the same wavelength dependence. As done for the case of the detector related systematic, the correction to the event weights has been computed as a function of the neutrino energy for both $\nu_\mu + \bar{\nu}_\mu$ and $\nu_e + \bar{\nu}_e$ CC events, reconstructed as up-going, and the resulting distributions have been fitted with the function defined in Equation 6.2. Figure 6.6 shows the histograms of the event weight correction as a function of true neutrino energy, together with its parameterization.

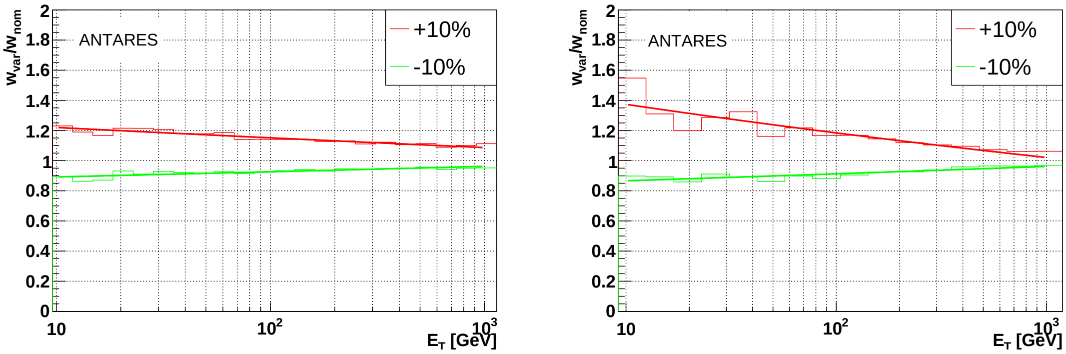

Figure 6.6: Expected event weight corrections as a function of true neutrino energy for a +10% (red) and −10% (green) from the nominal value of the water absorption length. Left panel: $\nu_\mu + \bar{\nu}_\mu$ CC events; Left panel: $\nu_e + \bar{\nu}_e$ CC events.

The values of the fitted parameters A and B are listed in Table 6.3.

	$\nu_\mu + \bar{\nu}_\mu$	$\nu_e + \bar{\nu}_e$
+10%	A = 1.29; B = -0.02	A = 1.59; B = -0.06
−10%	A = 0.86; B = 0.02	A = 0.82; B = 0.02

Table 6.3: Fitted values for the parametrization of the event weight correction with a variation of ±10% from the nominal value of the water absorption length.

Also in this case, the fitted functions well describe the distributions, and the two parameters A and B can be included in the effect of the global normalization factor N and the correction to the spectral index $\Delta\gamma$, which are considered in the minimization procedure.

6.3 Atmospheric muon background

As seen in Chapter 4, only 1/3 of the total expected atmospheric muons is simulated in our MC chain, which yields a rather large statistical uncertainty on the expected contamination, N_μ, due to these events. Whereas the total normalization of N_μ is considered as a systematic uncertainty, the distribution of these atmospheric muon events in energy and zenith angle is derived from simulations. At this purpose, we selected MC misreconstructed events with the same selection criteria discussed in Chapter 5. The surviving events are used to fill a histogram in reconstructed energy and zenith angle, with the same binning as the one used later in the minimization procedure (see Section 6.1). The resulting distribution is converted into a probability density function (PDF), by normalizing and smoothing the histogram through the *ROOT* function `TH::Smooth` [126]. In this way, one can introduce in the fitting procedure an additional nuisance parameter, N_μ, which controls the yield of such distribution, accounting for the background contamination. In Figure 6.7, the resulting PDFs for all the different sets of quality criteria are shown. For all the sets of selection criteria, the major contribution due to misreconstructed atmospheric muons is expected from vertical events, mainly due to the *BBFit* SL contribution. The fourth set of quality cuts is the one which foresees the larger contamination in this region, which is also the one from which we expect the oscillation signal to be stronger.

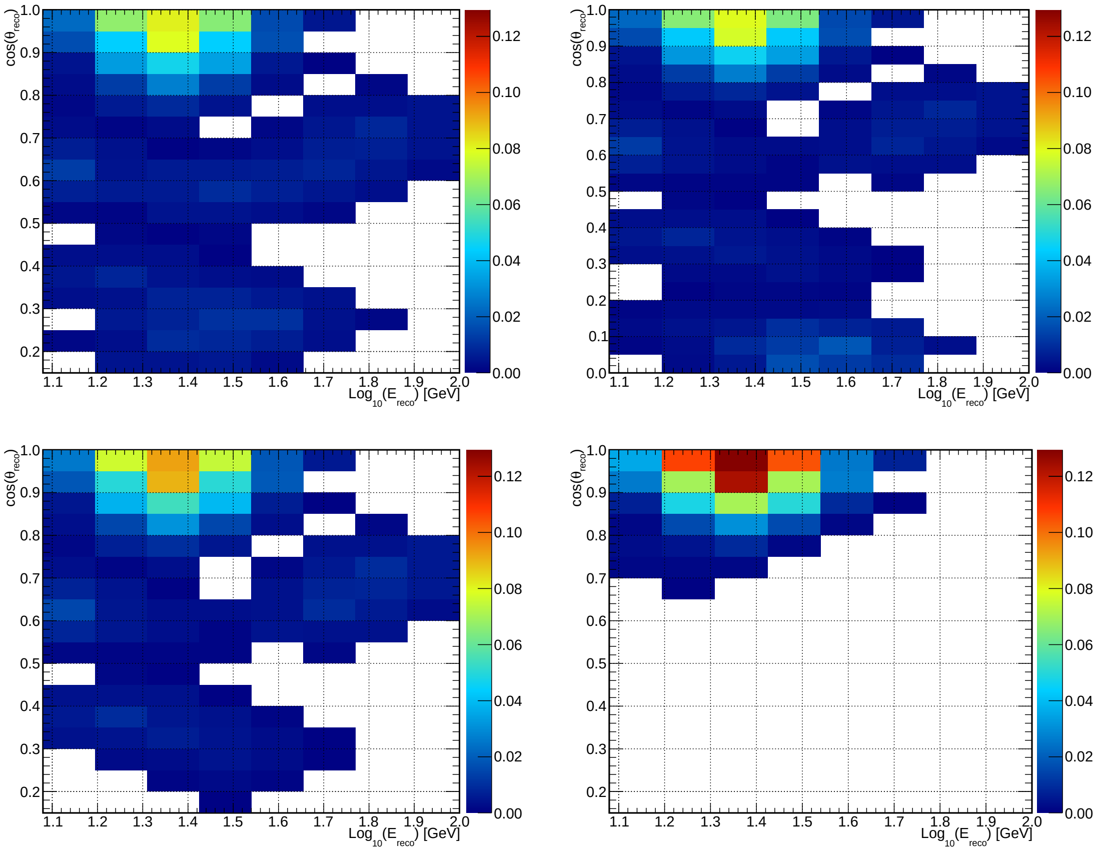

Figure 6.7: Atmospheric muon background PDFs from MC selected events. The distribution is shown for the different sets of quality criteria tested: *cut 1* (upper left), *cut 2* (upper right), *cut 3* (bottom left) and *cut 4* (bottom right).

6.4 Sensitivity study

In this Section a sensitivity study, which has been made before the data unblinding, using only MC, is presented. Confidence regions are obtained, using a pseudo-data sample constructed from MC under a particular test oscillation hypothesis.

6.4.1 Pseudo-data sample

In order to test the whole analysis using only MC, one has to build a pseudo-data sample. This has been made using the so called *Asimov data set*, by weighting the MC events under a certain oscillation hypothesis and a particular set of values for the different systematic sources. No Poisson smearing has been used. The values of the parameters employed to build the pseudo-data sample will be referred to as *test values* in the following discussion. In Table 6.4 a list with all the test values, as well as their eventual prior is given.

Name	Test Value	Prior
N	1.0	FREE
Δm^2_{32} $[10^{-3}\,\mathrm{eV}^2]$	2.46	FREE
θ_{23} [°]	41.38	FREE
θ_{13} [°]	8.41	8.41±0.28
$\Delta\gamma$	0.0	0.00 ± 0.05
X_{sec} $[\sigma]$	0.0	0.0±1.0
$\nu/\bar{\nu}$ $[\sigma]$	0.0	0.0±1.0
N_μ	1.0	FREE

Table 6.4: List of *test values* with eventual prior, for all the parameters fitted in the analysis.

6.4.2 Expected confidence regions

A minimization as described in 6.1 is performed in order to find the set of parameters which best represent our test. By construction, the minimum is found at the test point.

The different event selection criteria have been tested in terms of expected sensitivity to the atmospheric neutrino oscillation parameters.

In Figure 6.8, the 90% CL confidence regions in the parameter space of $\sin^2\theta_{23}$ and Δm^2_{32} are presented. They have been obtained following the procedure described in Section 6.1. It can be seen from the figure that, in terms of expected final sensitivity to the atmospheric neutrino oscillation parameters, the samples selected using as quality criteria the ones from *cut 1* and *cut 2* perform quite similarly and better than the other two, which show a weaker sensitivity, especially in confining θ_{23}. It has been decided to proceed with the un-blinding of the data using the set of *cut 1* as event selection criteria, since, compared to the *cut 2*, it foresees a smaller atmospheric muon contamination.

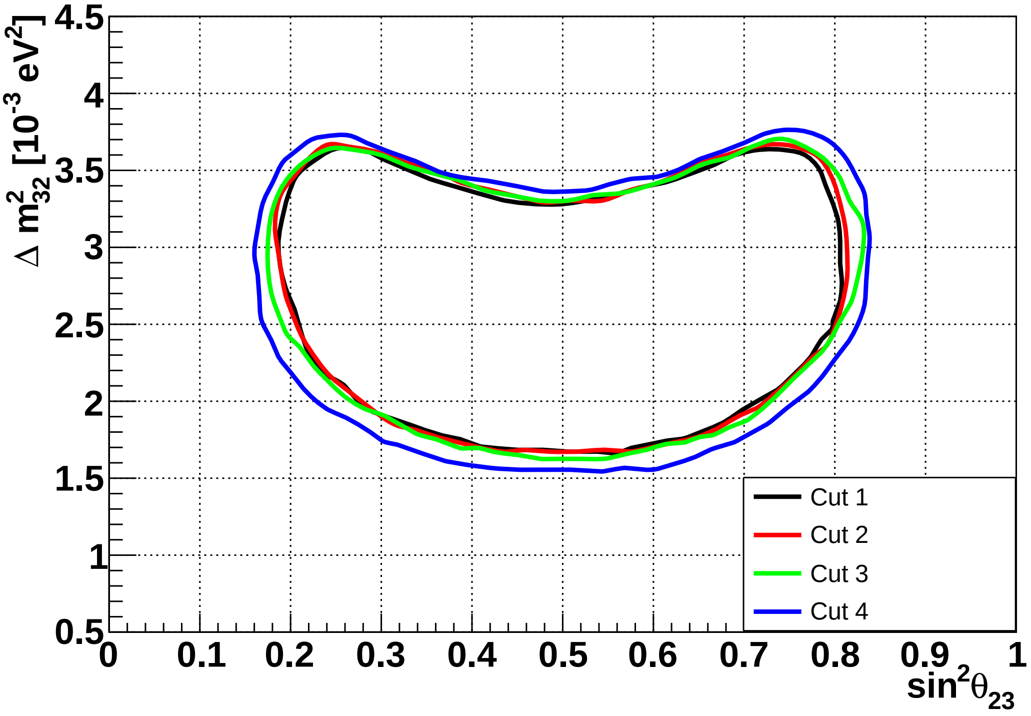

Figure 6.8: Expected 90% CL sensitivity to the atmospheric neutrino oscillation parameters $\sin^2\theta_{23}$ and Δm^2_{32} from the MC study. Results are presented for the different sets of event selection criteria: *cut 1* (black), *cut 2* (red), *cut 3* (green) and *cut 4* (blue).

6.5 Results

In this Section the results obtained after the un-blinding of the data are discussed. After a brief description of the data sample, some data/MC comparison plots are shown, and the final results are presented.

6.5.1 Data sample

ANTARES data collected from 2007 to 2016 have been considered in the analysis. A basic run selection criteria has been applied, in order to exclude from the analysis those runs in which particularly bad environmental conditions could have affect the data acquisition. A total of 2830 days of lifetime has been evaluated, and, after applying the event selection criteria *cut 1* (see Chapter 5), 7710 events were selected. In Figure 6.9 the data distribution is shown in the 2-dimensional histogram used later in the fit.

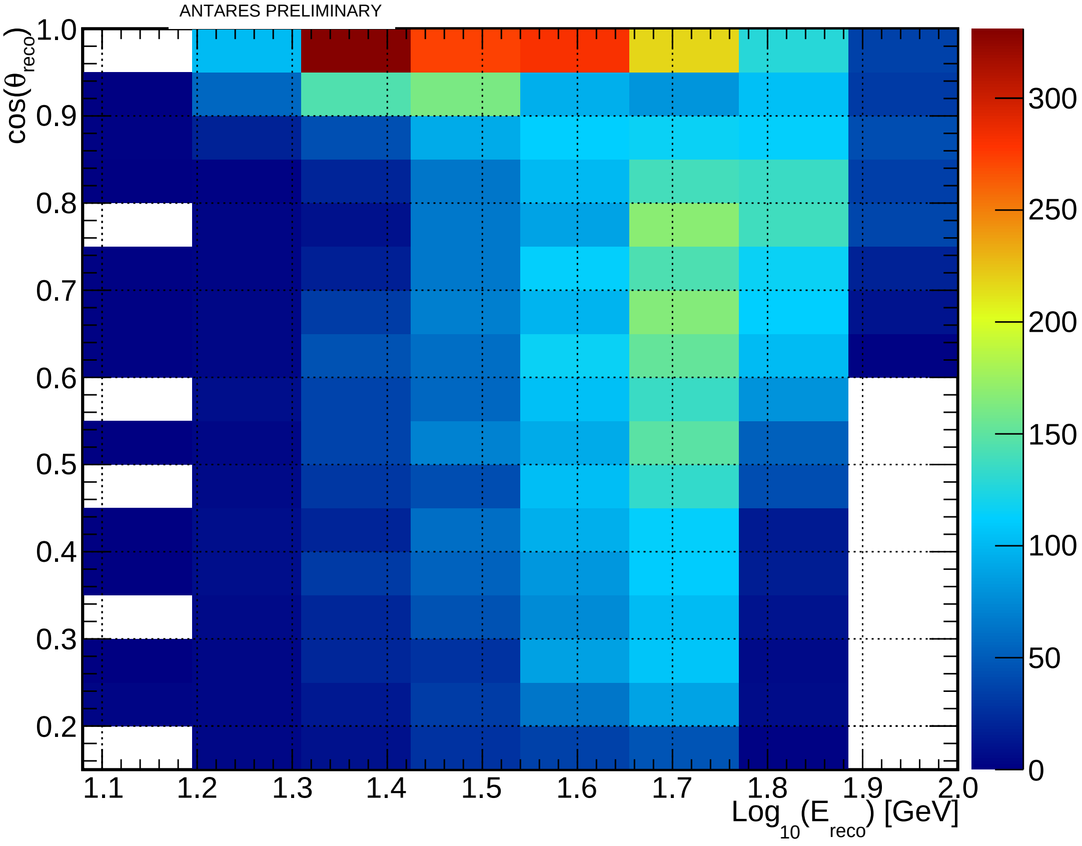

Figure 6.9: Data event distribution in $\log_{10}(E_{reco})$ and $\cos\theta_{reco}$.

6.5.2 Data/MC comparison

In order to check the correct implementation of the event selection criteria, some data/MC comparison plots have been made, in terms of the main variables used in the event selection. In the following figures the results of this comparison are shown. MC events have been weighted both assuming no oscillations, and assuming a simple 2-flavour oscillation scenario, with $\Delta m^2_{32} = 2.46 \times 10^{-3}\,\mathrm{eV}^2$ and $\theta_{23} = 41.38°$.

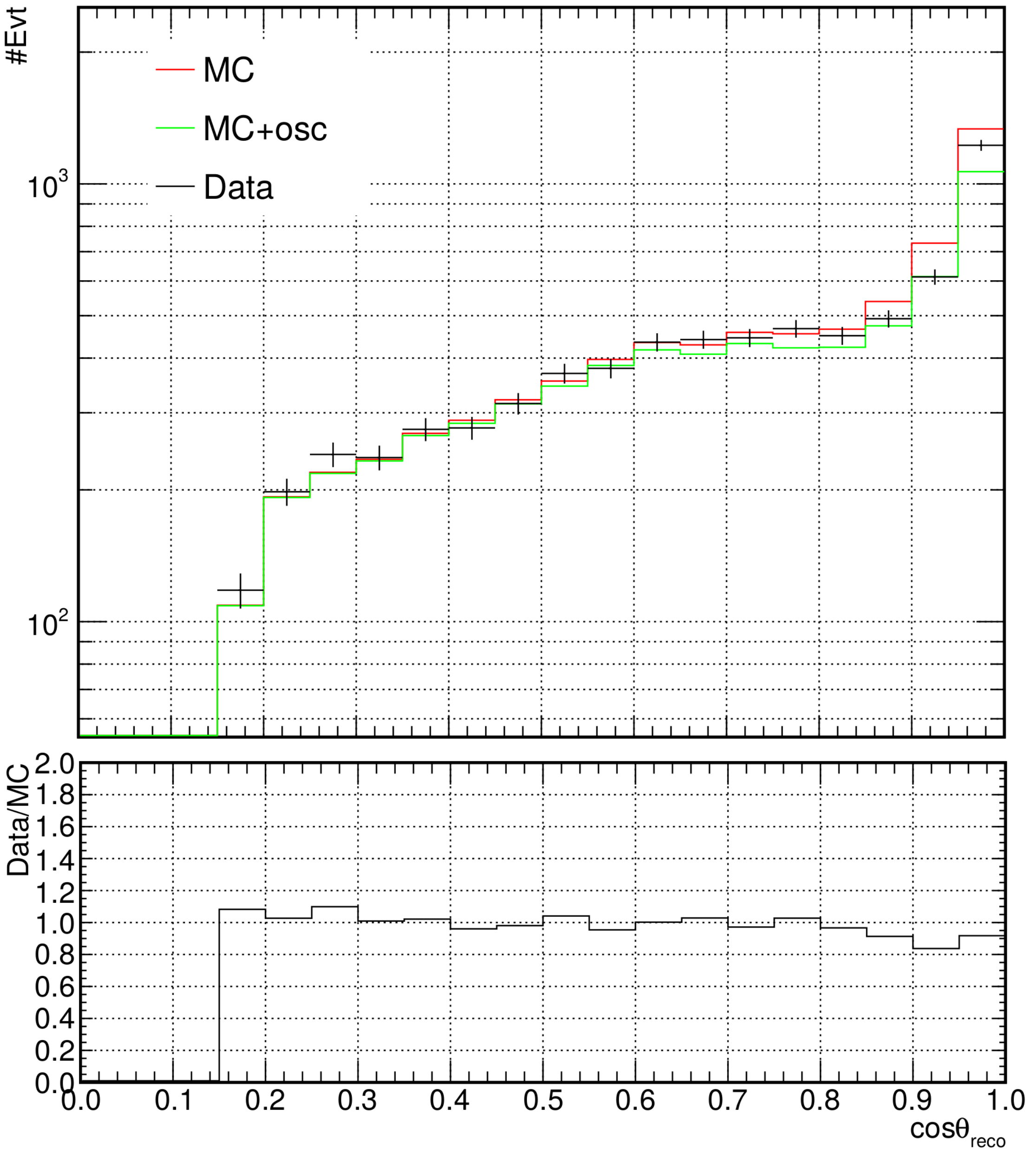

Figure 6.10: Data/MC comparison for reconstructed cosine of zenith. MC events have been weighted both assuming no oscillations (red), and assuming a simple 2-flavour oscillation scenario, with $\Delta m^2_{32} = 2.46 \times 10^{-3}\,\mathrm{eV}^2$ and $\theta_{23} = 41.38°$ (green). The Data/MC ratio is computed using MC without oscillations.

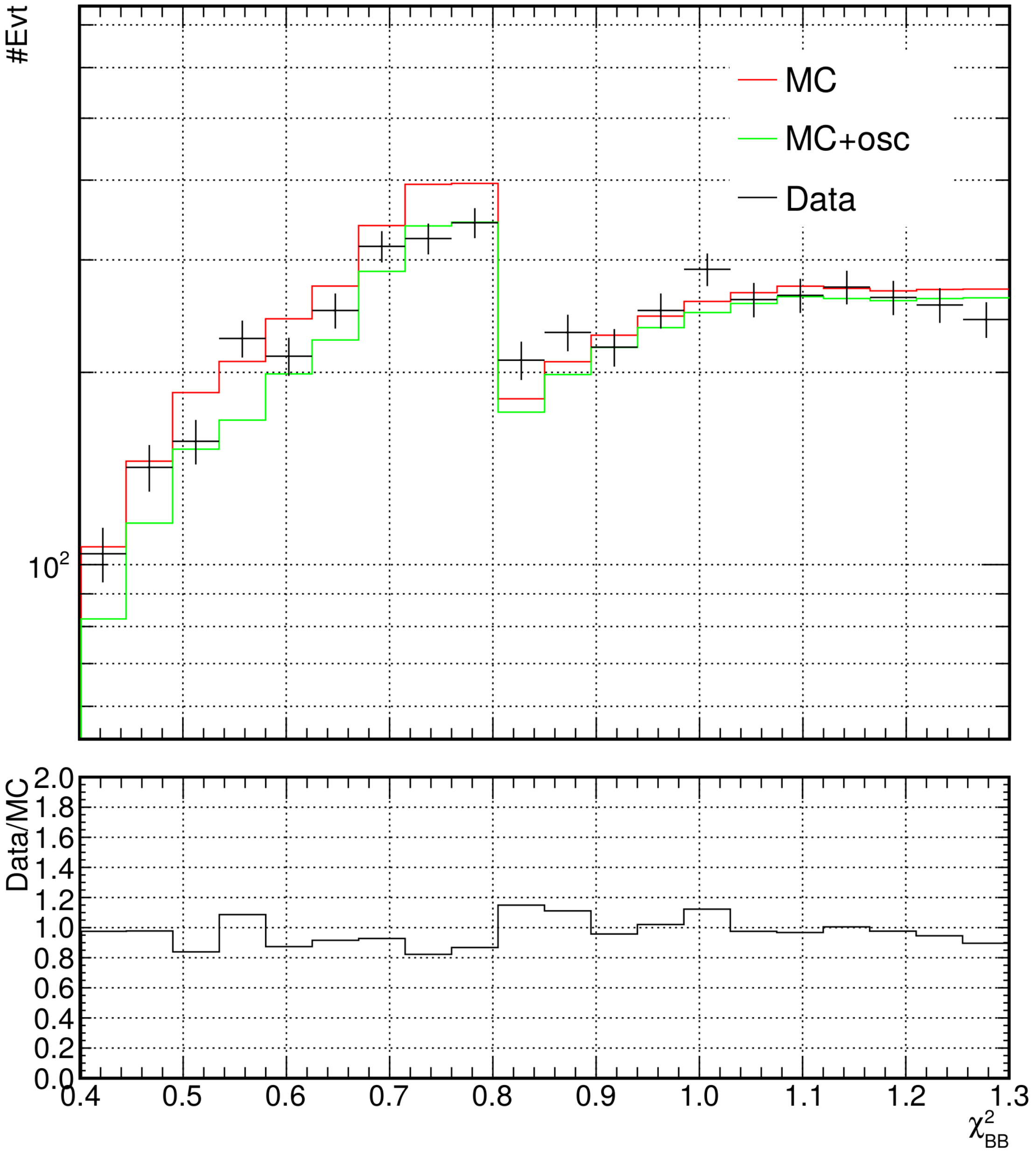

Figure 6.11: Data/MC comparison for $\bar{Q}$ quality parameter of *BBFit* (see Chapter 4). MC events have been weighted both assuming no oscillations (red), and assuming a simple 2-flavour oscillation scenario, with $\Delta m^2_{32} = 2.46 \times 10^{-3}\,\mathrm{eV}^2$ and $\theta_{23} = 41.38°$ (green). The Data/MC ratio is computed using MC without oscillations. The two distinct peaks are due to the different cut in $\bar{Q}$ for SL and ML events.

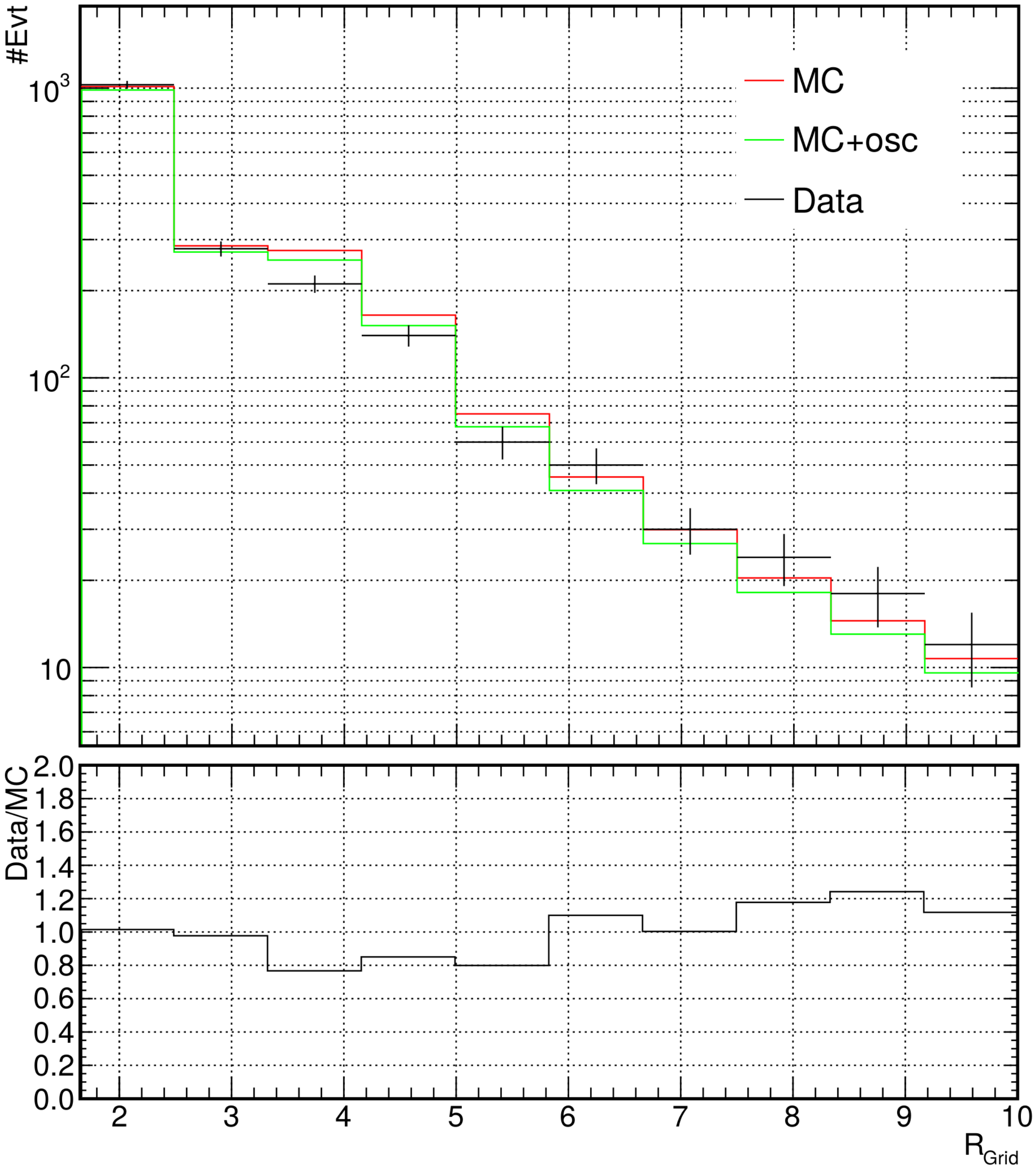

Figure 6.12: Data/MC comparison for R quality parameter of *GridFit* (see Chapter 4). MC events have been weighted both assuming no oscillations (red), and assuming a simple 2-flavour oscillation scenario, with $\Delta m^2_{32} = 2.46 \times 10^{-3}\,\mathrm{eV}^2$ and $\theta_{23} = 41.38°$ (green). The Data/MC ratio is computed using MC without oscillations.

6.5.3 Atmospheric muon contamination

After the un-blinding of the data, it has been decided to estimate the total expected muon contamination and its uncertainty by means of a data-driven technique.

The idea is to apply a softer cut in the quality of the reconstruction, and look in a region which is close to the signal, but, at the same time, where the atmospheric muons constitute the dominant part. By fitting the data in this region and extrapolating them into the signal zone, one can get an estimation of the muon contamination.

Since from the MC study it has been observed that the major contribution to the muon contamination comes from *BBFit* SL events (64% of the total) and from *GridFit* events (30% of the total), it has been decided to focus on these two procedures . After applying a softer cut on $\bar{Q}$ and $r \log L$, respectively, four exponential fits have been performed for each distribution, by varying the first and last bin in which the fit is done. In the following figure the corresponding distributions for data, MC neutrinos and MC atmospheric muons are shown, together with the fitted functions and their extrapolation into the signal region. Two distinct distributions are shown for *GridFit* events, which refer to the two sets of quality selection criteria applied (see Chapter 5 for details).

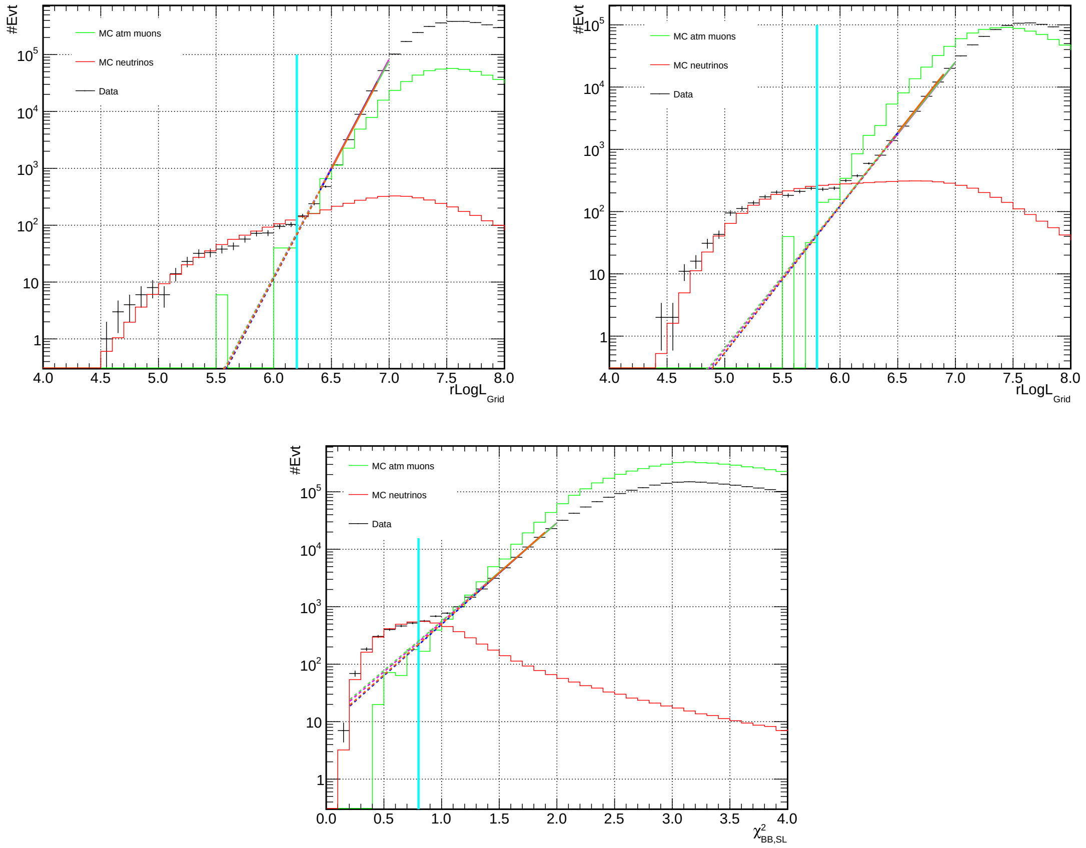

Figure 6.13: Data and MC distribution (red for MC neutrinos, green for MC atmospheric muons) of $r \log L$ quality parameter of *GridFit* events (upper panel) and of $\bar{Q}$ quality parameter of *BBFit* SL events (lower panel). The light-blue line indicates where the event selection is applied. The four different fits (solid lines) are shown together with their extrapolation into the signal region (dashed lines).

The mean value of the fitted parameters has been computed together with their standard deviation. The integral under the resulting curve has been used as prior for the muon contamination. The uncertainty on this estimation has been computed analytically by propagating the error on the fitted parameters to the integral under the fitted curve. A total of 742 misreconstructed atmospheric muons is expected with this extrapolation over the whole considered lifetime, and the corresponding uncertainty is found to be of 16%.
The overall expected muon contamination estimated in this way is larger than the one estimated only from MC; however, the contribution from the different channels, namely *BBFit* SL and *GridFit* events, increases proportionally. This justifies the use of the PDF, derived from MC and described in 6.3, in order to describe the energy and direction distributions for such events.

6.5.4 Fit results

The minimization has followed the *log-likelihood* approach described in Section 6.1. We remind that the solar oscillation parameters have been kept fixed to their global best fit value, δ_{CP} has been fixed at zero, and a normal mass ordering has been assumed.

The best fit value is found for Δm^2_{32} at 2.0×10^{-3} eV^2 and for θ_{23} at 45.4°. The list of all the fitted parameters is shown in Table 6.5, together with the error computed directly by the fit procedure.

Name	Prior	Fit
N	FREE	0.82 ± 0.09
$\Delta m^2_{32}[10^{-3}eV^2]$	FREE	2.0± 0.3
$\theta_{23}[deg]$	FREE	45.4 ± 12.1
$\theta_{13}[deg]$	8.41±0.28	8.41± 0.28
$\Delta\gamma$	0.0± 0.05	-0.003 ± 0.036
$X_{sec}[\sigma]$	0.0±1.0	0.008 ± 0.98
$\nu/\bar{\nu}[\sigma]$	0.0±1.0	1.08 ± 0.60
$N_\mu[\%]$	100% ± 16%	56% ± 3%

Table 6.5: Fitted values obtained from the minimization for all the parameters considered in the analysis.

The global normalization factor for neutrinos, N, is found 20% lower. This value is within the atmospheric neutrino flux uncertainties and it is compatible with what reported by other analyses [48]. No sensitivity is found for θ_{13} nor for X_{sec}, for which the error on the best fit value is close to the prior error we assumed. Concerning the spectral index correction, $\Delta\gamma$, no significant distortion from the nominal value is observed. A stronger pull is found on $\nu/\bar{\nu}$, which regulates the flux asymmetry for neutrino and anti-neutrino and also contains the dependence of the flux on the zenith direction. The fitted value for the atmospheric muon contamination, finally, is found incidentally very close to the MC expectations.

Confidence level contours are computed by looping over a fine grid of values in Δm^2_{32} and θ_{23} and minimizing over all the other parameters. In Figure 6.14 the 90% CL obtained in this study is shown compared to the one resulted from the previous ANTARES oscillation analysis [47]. It is worth mentioning that the previous analysis was done on 3 years of ANTARES data and only accounted for two systematic effects. In order to allow a clearer comparison with the previous analysis, the current data sample has been fitted also letting only 3 parameters completely unconstrained, namely the two atmospheric oscillation parameters, Δm^2_{32} and θ_{23}, and the global normalization factor, N. A clear improvement with respect to the previous analysis can be seen, which is the result of both the increased statistic and the refinements in the analysis chain. Furthermore, despite the addition of other sources of systematic in this new work, the improvement is evident, especially in constraining Δm^2_{32}.

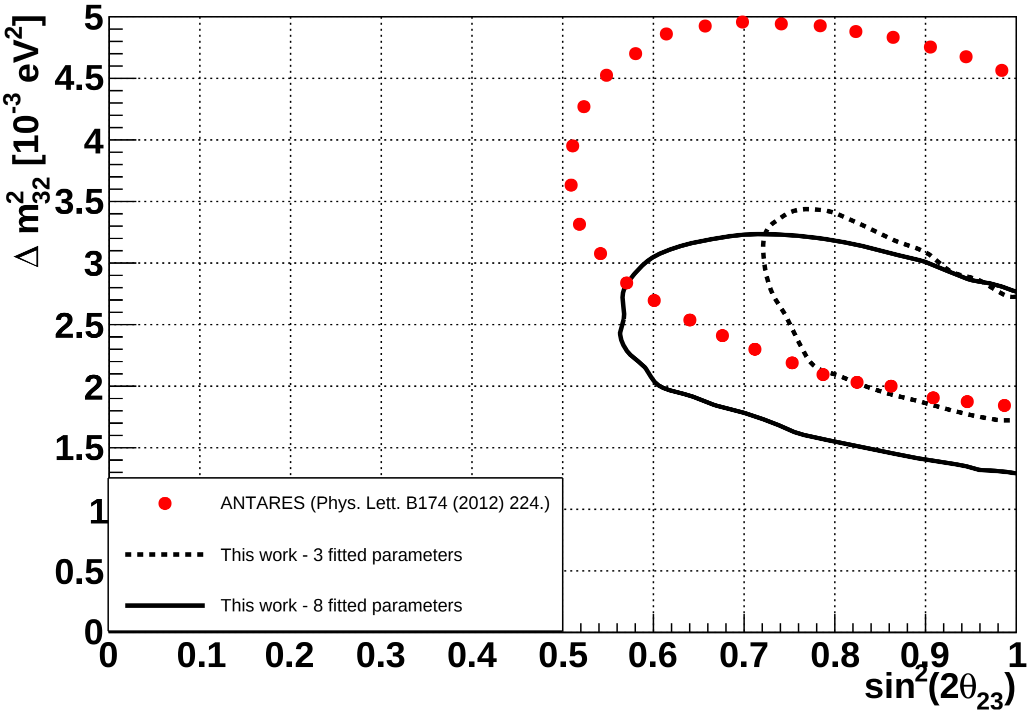

Figure 6.14: 90% CL obtained in this work fitting all the 8 parameters described in Table 6.5 (black solid line) and fitting only 3 parameters (N, Δm^2_{32} and θ_{23}) (dashed line), compared to the results of the previous ANTARES oscillation analysis (red dots) [47].

The distribution of reconstructed energy over reconstructed cosine of zenith of data and MC at the best fit point is shown in Figure 6.15. For comparison, also the distribution of MC assuming no neutrino oscillation, as well as the one at the world best fit is shown. We remind that the actual fit is not done on this kind of histogram, but it is performed on a 2-dimensional one.

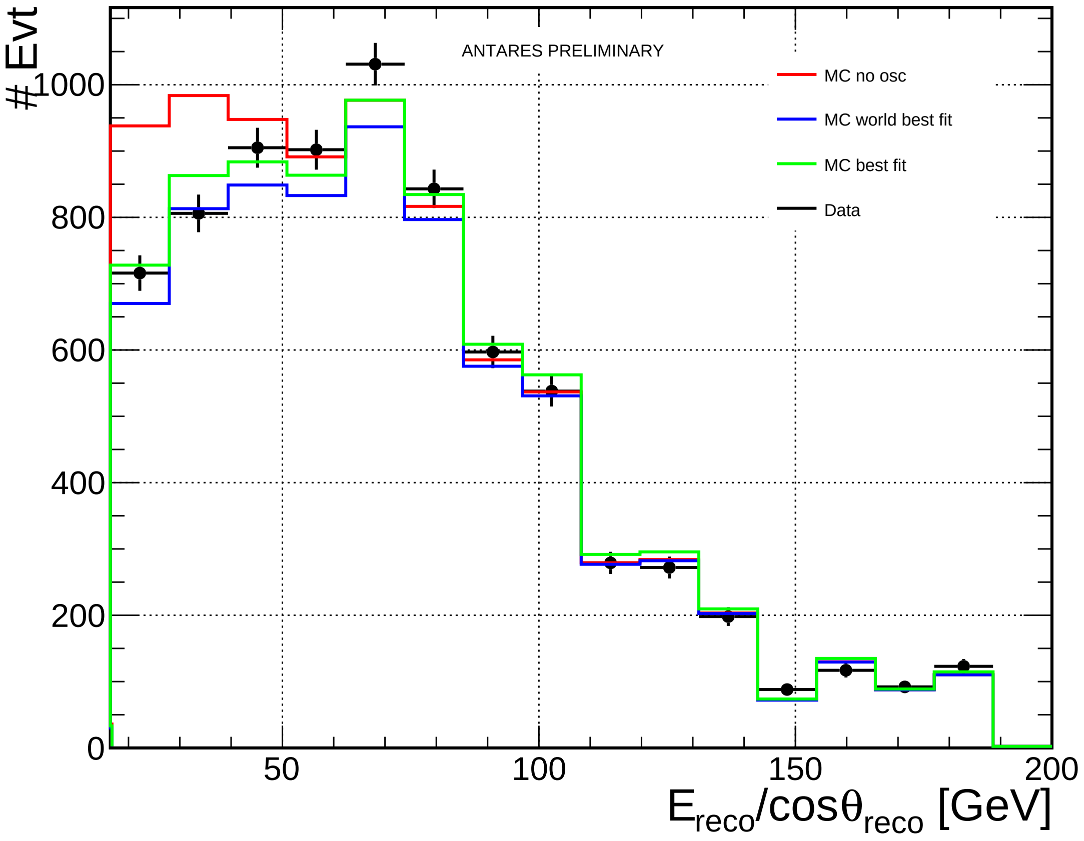

Figure 6.15: $E_{reco}/\cos\theta_{reco}$ distribution for data (black), MC without oscillations (red), MC at world best fit (blue) and MC at best fit point of this analysis (green).

The non-oscillation hypothesis has been tested, and it is discarded with a significance of 4.6σ, to be compared with the 2.3σ obtained in the previous ANTARES analysis [47].

Results of this analysis have also been compared to the ones published by other collaborations. In Figure 6.16 this comparison is illustrated in the plane of $\sin^2\theta_{23}$ and Δm^2_{32}. The 1-dimensional projections are shown as well.

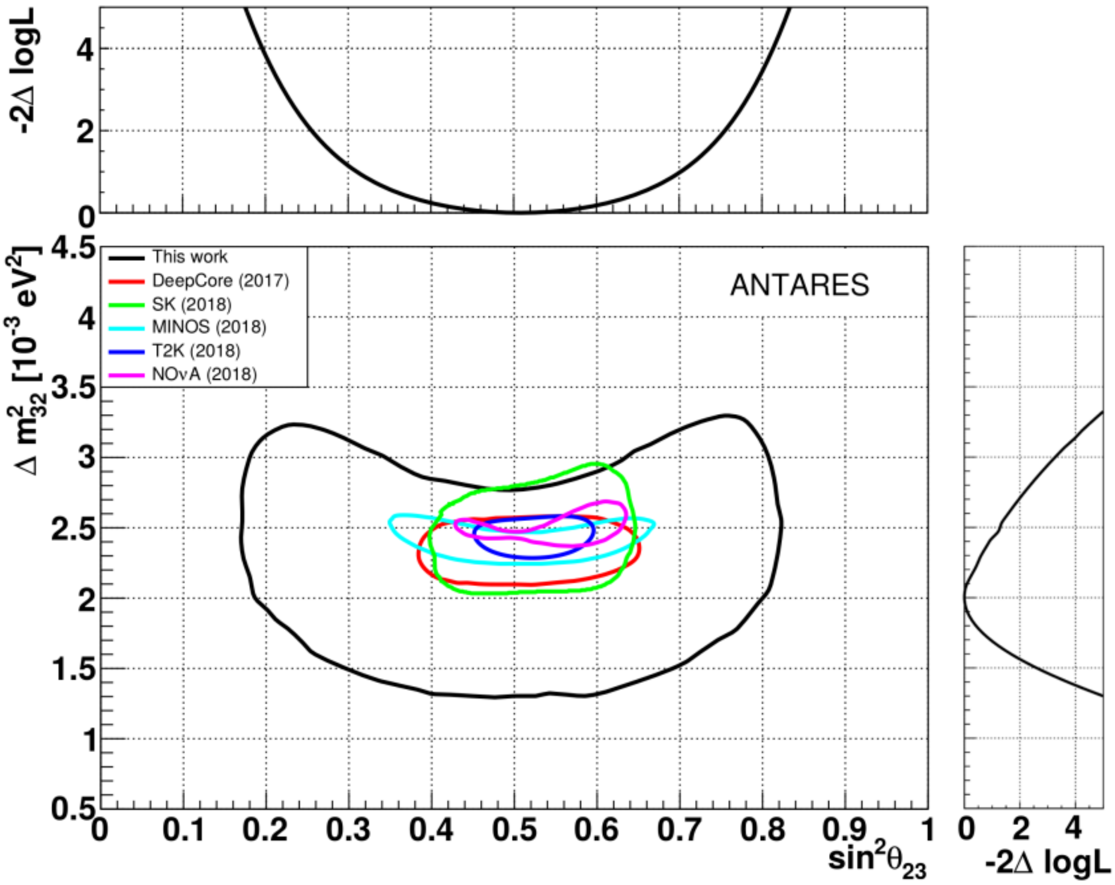

Figure 6.16: 90% CL obtained in this work (black line) and compared to the results by other collaborations: DeepCore (red) [48], Super-Kamiokande (green) [46], NOνA (purple) [49], T2K (blue) [50], and MINOS (light blue) [51].

6.6 Conclusions

ANTARES data collected from 2007 to 2016 have been analyzed in order to measure the atmospheric neutrino oscillation parameters. Several sources of systematics have been considered in the analysis. The atmospheric muon contamination has been extrapolated by means of a data-driven technique.

Results show a good improvement with respect to the previous ANTARES oscillation analysis, and, even if not competitive with the measurements published by other collaborations, they are consistent with them.

Chapter 7

Constraining the 3+1 sterile neutrino parameters with ANTARES

In this Chapter the analysis of the ANTARES data in order to constrain two parameters of the 3+1 sterile neutrino model, namely the mixing angles θ_{24} and θ_{34}, is presented. Since the minimization procedure as well as the treatment of the major sources of systematic are the same as the one presented for the atmospheric neutrino oscillation analysis, we refer to Chapter 6 for the details. In the following, a discussion on some additional parameters which may affect the sensitivity to the 3+1 mixing parameters is presented. A sensitivity study, done with MC only, is introduced before discussing the complete results of the analysis with ANTARES data. A final section is devoted to a MC sensitivity study which has been performed in order to study the potential of ANTARES in constraining the 3+1 model parameter space with more energetic events.

7.1 Motivations

As seen in Chapter 1, recent experimental anomalies could, in principle, be explained in an extended 3+1 scenario, in which, in addition to the standard three *active* neutrino flavours, a *sterile* neutrino is also present. From the point of view of the parameters which describe the mixing between the mass and flavour eigenstates, adding a sterile neutrino means introducing six additional real terms: a new mass splitting, Δm^2_{41}, three new mixing angles, θ_{14}, θ_{24} and θ_{34}, and two new phases, δ_{14}

and δ_{24}.
While θ_{14} and δ_{14} are associated and mostly affects the electronic channel, the other parameters could modify the oscillation pattern of ν_μ and $\bar{\nu}_\mu$ in a detectable way. In particular, in the energy range around 20-100 GeV the effect is dominated by the two mixing angles θ_{24} and θ_{34}.

This is the same region we are interested in for the *standard* oscillation analysis, described in the previous Chapter. For this reason it has been decided to use the same data set as well as the same analysis chain in order to constrain two of the 3+1 additional parameters, θ_{24} and θ_{34}. The other parameters do not play a crucial role in this energy range, and have been treated as systematic or fixed in the analysis.

7.2 Systematic treatment

In this Section a discussion on the impact of the *standard* atmospheric oscillation parameters, θ_{23} and Δm^2_{32}, to the sensitivity of the analysis will be presented. Further comments on the role played by the 3+1 model phases are discussed. All the sources of systematics which will not be treated here have been implemented in the analysis in the same way as described in Chapter 6.

The fast oscillations due to $\Delta m^2_{41} \gtrsim 0.5\,\mathrm{eV}^2$ are unobservable at these energies, making Δm^2_{41} not measurable. Its precise value has no impact on the analysis as long as it is "large" compared to Δm^2_{32}. For this reason, a value of Δm^2_{41} of $0.5\,\mathrm{eV}^2$ has been kept fixed through all the analysis. The mixing angle θ_{14} and its associated phase δ_{14}, which affect mostly the electronic channel, are kept at zero.

7.2.1 *Standard* atmospheric neutrino oscillation parameters

The presence of an additional *sterile* neutrino would modify the oscillation pattern for neutrinos crossing the Earth's core (see Figure 1.13 in Chapter 1). These modifications are similar to the ones regulated by the *standard* atmospheric mixing parameters θ_{23} and Δm^2_{32}. For this reason, they are expected to be one of the major systematic in this analysis.

A study has been made on the possibility to include Δm^2_{32} and θ_{23} with a prior. The results will be discussed in the next section.

7.2.2 CP-violating phases

As previously discussed, in a 3+1 model the unitary mixing matrix which relates flavour to mass eigenstates gains two additional real CP-violating phases, δ_{14} and δ_{24}, with respect to the *standard* case. Since in the analysis a fixed null value of θ_{14} is assumed, and δ_{14} is always related to it, this phase has no impact in this work, and it is let at zero as well. On the other hand, δ_{24} could in principle have an effect on the results and is treated as a free parameter. δ_{CP}, instead, has no significant impact in the analysis, thus, it has been kept fixed at zero.

7.3 Sensitivity study

In this Section a sensitivity study, which has been made before the data unblinding, using only MC, is presented and confidence regions are obtained, using a pseudo-data sample constructed from MC under a test oscillation hypothesis.

7.3.1 Pseudo-data sample

The pseudo-data sample for the 3+1 analysis has been built weighting the MC events under the assumption that no sterile neutrino exists. It constitutes an *Asimov data test.* No Poisson smearing has been assumed.

For this analysis events have been selected directly with *cut 1* (for details, see Chapter 5). They have been binned in a 2D histogram of reconstructed energy and cosine of zenith, as the one used for the standard oscillation analysis presented in the previous chapter. A first *underflow* bin contains all events with $\log_{10} E_{reco} < 1.2$, and 7 more bins, equally spaced, are filled with the events up to $E_{reco} = 100\,\mathrm{GeV}$. This choice is motivated by the fact that very low statistic is available for $\log_{10} E_{reco} < 1.2$. In $\cos\theta_{reco}$, instead, 17 bins from 0.15 to 1 have been considered.

A study was made on the possibility to add the standard atmospheric oscillation parameters with a prior in the analysis. The IceCube Collaboration found through simulations that prior values for the standard mixing parameters can lead to a fake non-zero best fit point with significance up to 1σ [66]. For this reason, a similar test has been done within this work, by investigating the effect of assuming a *wrong* prior on the best fit result. The tests have been performed by constructing a MC pseudo-data sample with different values for the priors of the standard atmospheric oscillation parameters and under the assumption of no sterile neutrino, and performing a minimization on such sample.

The values used to build the pseudo-data sample will be referred to as *test values* in the following discussion. In Table 7.1 a list with all the test values, as well as their eventual prior is given.

Name	Test Values	Prior
N	1.0	FREE
θ_{24} [°]	0.0	FREE
θ_{34} [°]	0.0	FREE
δ_{24} [°]	0.0	FREE
Δm^2_{32} [$10^{-3}\,\mathrm{eV}^2$]	2.46	2.46±0.14
θ_{23} [°]	41.38	$\sin^2(2\theta_{23}) = 1.0 \pm 0.05$ (FREE)
θ_{13} [°]	8.41	8.41±0.28
$\Delta\gamma$	0.00	0.00 ± 0.05
X_{sec} [σ]	0.0	0.0±1.0
$\nu/\overline{\nu}$ [σ]	0.0	0.0±1.0
N_μ	1.0	FREE

Table 7.1: List of *test values* with eventual prior, for all the parameters fitted in the analysis.

In Table 7.2 the list of the different prior values for Δm^2_{32} and $\sin^2(2\theta_{23})$ is presented, together with the corresponding best fit point for the two matrix elements, $|U_{\mu 4}|^2 = \sin^2\theta_{24}$ and $|U_{\tau 4}|^2 = \sin^2\theta_{34}\cos^2\theta_{24}$. These fit points have also been compared to the confidence regions of our sensitivity study.

$\Delta m^2_{32,true}$ eV^2	$\Delta m^2_{32,test}$ eV^2	$\sin^2(2\theta_{23})_{true}$	$\sin^2(2\theta_{23})_{test}$	$\lvert U_{\mu 4}\rvert^2_{BF}$	$\lvert U_{\tau 4}\rvert^2_{BF}$
2.46×10^{-3}	2.46×10^{-3}	1.0	0.97	1.9×10^{-3}	9.2×10^{-3}
2.46×10^{-3}	2.46×10^{-3}	1.0	0.95	2.4×10^{-3}	2.2×10^{-2}
2.46×10^{-3}	2.30×10^{-3}	1.0	0.97	1.2×10^{-2}	2.5×10^{-2}
2.46×10^{-3}	2.65×10^{-3}	1.0	0.97	1.1×10^{-2}	3.1×10^{-2}

Table 7.2: List of different tests made to check the effect of priors on Δm^2_{32} and $\sin^2(2\theta_{23})$. $\Delta m^2_{32,true}$ and $\sin^2(2\theta_{23})_{true}$ list the true values of Δm^2_{32} and $\sin^2(2\theta_{23})$ used to build the pseudo-data sample; $\Delta m^2_{32,test}$ and $\sin^2(2\theta_{23})_{test}$ the "wrong" tested priors on these parameters; $|U_{\mu 4}|^2_{BF}$ and $|U_{\tau 4}|^2_{BF}$ the best fit values found for the two mixing parameters for each test.

7.3.2 Expected confidence regions

After constructing the pseudo-data sample the *log-likelihood* minimization has been performed, following the procedure illustrated in 6.1, in order to find the set of parameters which describes the *test* sample at best, and limits in the parameter space of the two matrix elements $|U_{\mu 4}|^2 = \sin^2\theta_{24}$ and $|U_{\tau 4}|^2 = \sin^2\theta_{34}\cos^2\theta_{24}$ have been built. The results can be seen in Figure 7.1, at the 90% and 99% CL. In the figure also the best fit values for the two sterile matrix elements for the different tests made assuming a wrong prior on the standard atmospheric oscillation parameters are shown.

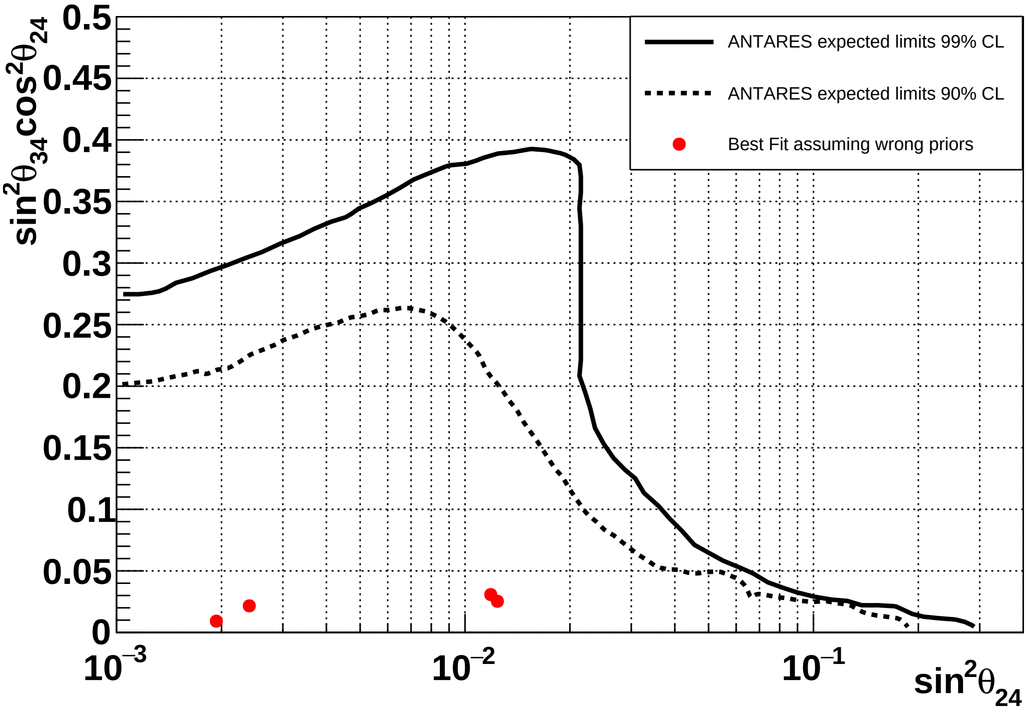

Figure 7.1: Expected 99% CL (solid line) and 90% CL (dashed line) exclusion regions for the 3+1 model parameters $|U_{\mu 4}|^2 = \sin^2\theta_{24}$ and $|U_{\tau 4}|^2 = \sin^2\theta_{34}\cos^2\theta_{24}$. Red dots are the global minima found for each of the performed tests with "wrong" priors on Δm^2_{32} and $\sin^2(2\theta_{23})$. Exclusion regions are on the right-hand side of the curves.

As can be seen from the figure, the use of priors for Δm^2_{32} and $\sin^2(2\theta_{23})$ leads to a non-zero best fit point for the two sterile mixing angles, even if the pseudo-data sample has been constructed assuming no sterile neutrino. However, those minima would all fall in the region where no exclusion can be made. For this reason, it has been decided to keep the above mentioned prior on Δm^2_{32}. On the other hand, it has been found, that, when dealing with the 3+1 scenario, the capability of determining the true value of θ_{23} is strongly degraded [138]. For this reason it has been decided to let θ_{23} unconstrained for all the following presented results. The final MC sensitivity study, to which the contours in Figure 7.1 correspond, has then been performed by constructing the pseudo-data sample with the values reported in Table 7.1 and no prior in $\sin^2(2\theta_{23})$.

7.4 Results

In this Section the un-blinded results of the sterile analysis are presented. Since the used data set is the same as the one employed in the standard oscillation analysis, we refer to Chapter 6 for the details on the data event distribution and for data/MC comparisons.

As for the standard oscillation analysis, a *log-likelihood* approach has been followed. Furthermore, to ensure the stability of the fit procedure, it has been decided to keep the muon contamination fixed at the best fit value found by the standard oscillation analysis. This choice is conservative, in the sense that it does not lead to better constraints with respect to the case of a free muon contamination.

The results of the minimization are summarized in Table 7.3.

Name	Prior	Fit
N	FREE	0.81 ± 0.09
θ_{24} [°]	FREE	0.94 ± 1.84
θ_{34} [°]	FREE	24.14 ± 3.88
δ_{24} [°]	FREE	0 ± 115
Δm^2_{32} [10^{-3} eV^2]	2.46±0.14	2.49 ± 0.13
θ_{23} [°]	FREE	48.77 ± 7.03
θ_{13} [°]	8.41±0.28	8.41 ± 0.28
$\Delta\gamma$	0.00 ± 0.05	-0.001 ± 0.035
X_{sec} [σ]	0.0±1.0	0.11 ± 0.99
$\nu/\overline{\nu}$ [σ]	0.0±1.0	1.09 ± 0.61

Table 7.3: Fitted values obtained from the minimization, for all the parameters considered in the analysis.

The global normalization factor for neutrinos, N, is found 20% lower, which is in agreement with what was found in the standard oscillation analysis, and it is consistent with the flux uncertainties. A large uncertainty is found for δ_{24}, denoting that our analysis is not very sensitive to this parameter. The fitted values of Δm^2_{32} and θ_{23} are different with respect to the ones we found in the standard oscillation analysis. This is due to the fact that here we are applying a prior on Δm^2_{32}, which in turn reflects on the fitted value for the mixing angle. As seen in the previous chapter, no sensitivity is found for θ_{13} nor for X_{sec}; while, no particular deviation from the nominal spectral index is observed. The strongest pull is again the one for $\nu/\overline{\nu}$, revealing that the analysis is sensitive to flux asymmetries. Concerning the two mixing angles we want to constrain, it can be seen from the table that, while θ_{24} is found compatible with zero, the best fit for θ_{34} is found at a larger value. Moreover, the error on this parameter given by the fitting procedure seems to indicate a deviation from zero of 6σ. It is worth mentioning that the errors on the fitted parameters are computed by the minimization procedure assuming a parabolic distribution of the minimizing function around the minimum, which is not always the case. For this reason, the actual error on θ_{34} is larger than the one provided in the table.

Contours have been computed on a fine 2D grid in $|U_{\mu 4}|^2$ and $|U_{\tau 4}|^2$, following the procedure described in 6.1. The results, at the 99% CL, are shown compared to the ones published by IceCube (DeepCore) and Super-Kamiokande in Figure 7.2. The one dimensional projections for our result are also shown. These have been derived by looking at the 2D distribution of $-2\Delta \log L$ and taking its minimum, for each value of $|U_{\mu 4}|^2$ and $|U_{\tau 4}|^2$, respectively.

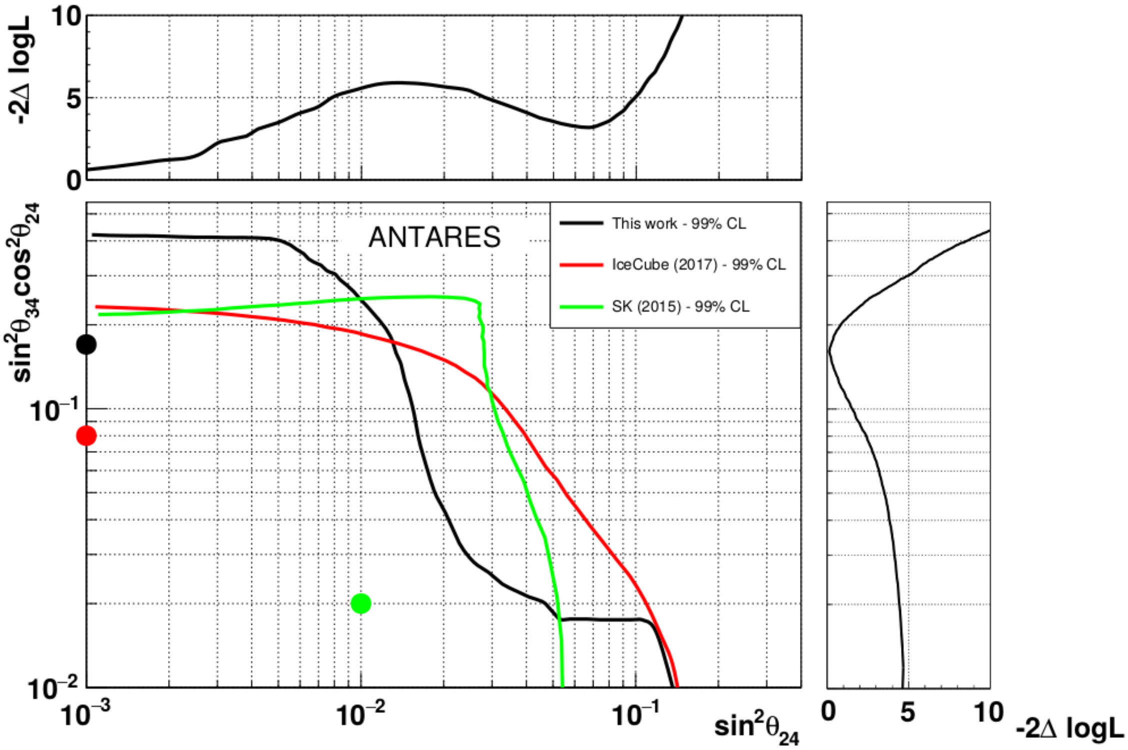

Figure 7.2: 99% CL exclusion regions for the 3+1 model in the parameter space of $|U_{\mu4}|^2 = \sin^2\theta_{24}$ and $|U_{\tau4}|^2 = \sin^2\theta_{34}\cos^2\theta_{24}$ obtained in this work (black, BF at $|U_{\mu4}|^2 = 0.00$ and $|U_{\tau4}|^2 = 0.17$) and compared to the ones published by IceCube [66] (red, BF at $|U_{\mu4}|^2 = 0.00$ and $|U_{\tau4}|^2 = 0.08$) and SK [67] (green, BF at $|U_{\mu4}|^2 = 0.01$ and $|U_{\tau4}|^2 = 0.02$). The 1D projections are also shown for our result.

As can be seen from the figure, results are consistent with the ones presented by the other collaborations. In particular, all three find the best fit for $|U_{\tau4}|^2$ different from zero. In some regions of the plane ANTARES limits are more stringent.

It is worth mentioning that both the energy range and the systematic treatment, in particular for what concerns the standard atmospheric oscillation parameters, are different among the three results illustrated in the figure. The DeepCore analysis [66] has been performed using events with reconstructed energy up to 56 GeV. On the other hand, the distortion on the oscillation pattern produced by the presence of a sterile neutrino is evident also at higher energies. Our analysis includes events with reconstructed energy up to 100 GeV, and this could be the reason of a major sensitivity for some values of the sterile mixing parameters.

Furthermore, in this work a prior on Δm^2_{32} is used; this is not the case for the DeepCore analysis, in which both the standard atmospheric oscillation parameters are left unconstrained. The main degradation on sensitivity due to the removal of such prior has been studied through MC and it has been found to affect only the region of small values of θ_{24}.

The Super-Kamiokande analysis [67] applies priors both on Δm^2_{32} and on $\sin^2(2\theta_{23})$, which could partially explain the more stringent limit they obtain at low values of θ_{24}.

Finally, our analysis let δ_{24} completely unconstrained, while for both the other analyses, this parameter has been kept fixed at zero, together with the standard δ_{CP}.

The non-sterile hypothesis has been tested and it is found to be slightly disfavored (at 2.2σ), similar to what is observed in the other analyses. In Figure 7.3 the 90% and 99% CL exclusion limits obtained in this work with respect to the best fit for the non-sterile hypothesis are given. These limits are still compared to the exclusion regions provided by IceCube and SK with respect to their corresponding best fit. Results show that, even the exclusion limits with respect to the non-sterile hypothesis improve with respect to the current constraints in some regions of the parameter space. The 1D projections are shown as well. These have been obtained by keeping one of the two sterile mixing angles under investigation at zero, looping over a fine grid of values on the other one, and minimizing with respect all the other parameters of the analysis.

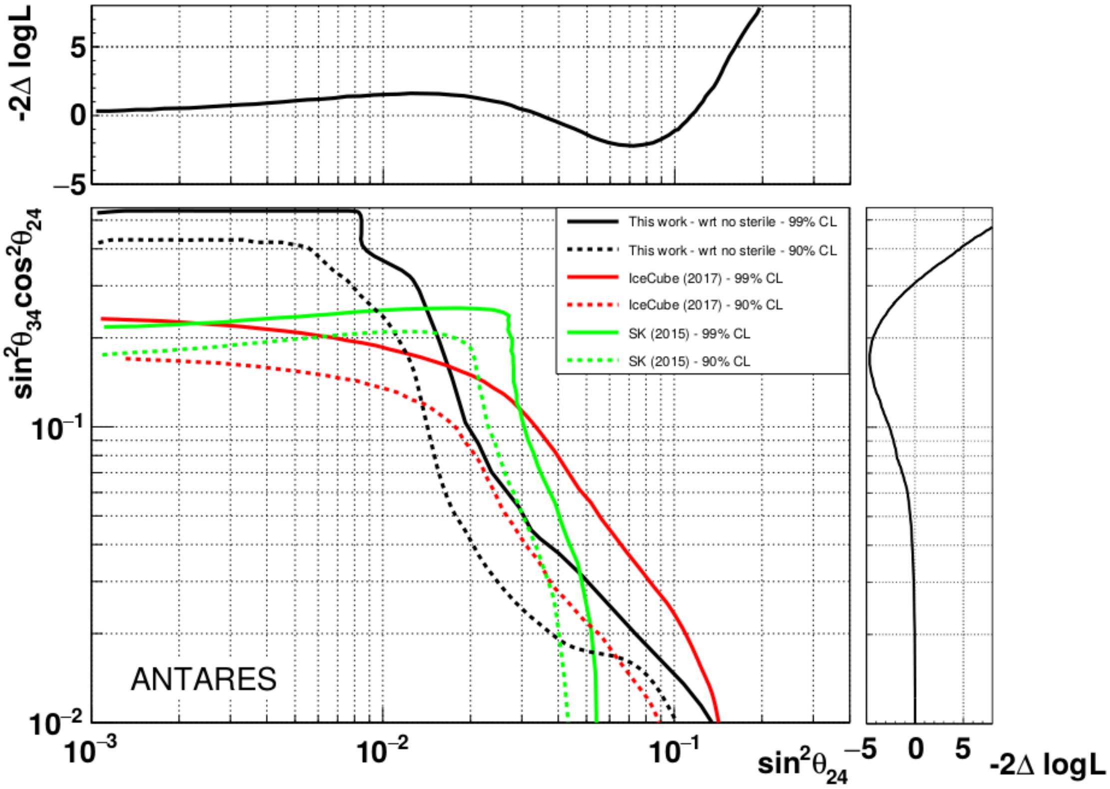

Figure 7.3: 90% (dashed lines) and 99% (solid lines) CL exclusion regions for the 3+1 model in the parameter space of $|U_{\mu4}|^2 = \sin^2\theta_{24}$ and $|U_{\tau4}|^2 = \sin^2\theta_{34}\cos^2\theta_{24}$ with respect to the best fit of the non-sterile hypothesis (balck lines), compared to the limits of IceCube [66] (red lines) and SK [67] (green lines) with respect to best fit point. The 1D projections are also shown for our result.

Looking at the one dimensional projections of Figure 7.3, one can set upper limits for the two matrix elements:

$$|U_{\mu4}|^2 < 0.14\ (0.18) \text{ at } 90\%\ (99\%) \text{ CL} \tag{7.1}$$

$$|U_{\tau4}|^2 < 0.36\ (0.44) \text{ at } 90\%\ (99\%) \text{ CL} \tag{7.2}$$

7.5 MC sensitivity study for constraining the 3+1 neutrino model at higher energies

In this Section a sensitivity study, based on MC only, is presented. The aim of this analysis is to evaluate the ANTARES potential in constraining the 3+1 model with events in the energy range of 10^3-10^4 GeV. At this energy range, the presence of an additional *sterile* neutrino would still modify the standard oscillation pattern for ν_μ and $\overline{\nu}_\mu$ crossing the Earth‘s core. The effect is mostly dependent on the value of the mixing angle θ_{24} and of the mass splitting Δm^2_{41}, as can be seen from Figure 1.15 in Chapter 1, due to the matter resonance in the Earth‘s mantle.

A normal mass hierarchy for the additional sterile neutrino is assumed, namely $m_4 > m_i$, with $i = 1, 2, 3$. In this case the resonance would appear in the anti-neutrino sector.

For this study, a pseudo-data sample based on a total lifetime of 2830 days has been built, using the *Asimov data set* approach. Events have been reconstructed with *AAFit* (see Chapter 5) and the selection has been made accordingly to what is described in 5.4. Only MC neutrinos have been considered for this study, thus the impact of the misreconstructed atmospheric muons which pass the selection has not been taken into account.

Since at these energies standard oscillations do not play an important role, both Δm^2_{32} and θ_{23} have been kept fixed at their world best fit values (see Table 1.1 in Chapter 1). Furthermore, θ_{34} has been fixed at zero.

The other sources of systematics have been considered as in the previous sterile neutrino analysis for the low energy range. No CP-violating phase is considered.

The minimization has been performed on a 2D histogram of 10 bins in logarithmic of the reconstructed energy, $\log_{10}(E_{reco})$, from 2 to 4, and in 20 bins of reconstructed cosine of zenith from 0 to 1. The histogram of the selected MC $\nu_\mu + \bar{\nu}_\mu$ CC events is shown in Figure 7.4.

The complete list of the parameters considered for this study is shown in Table 7.4.

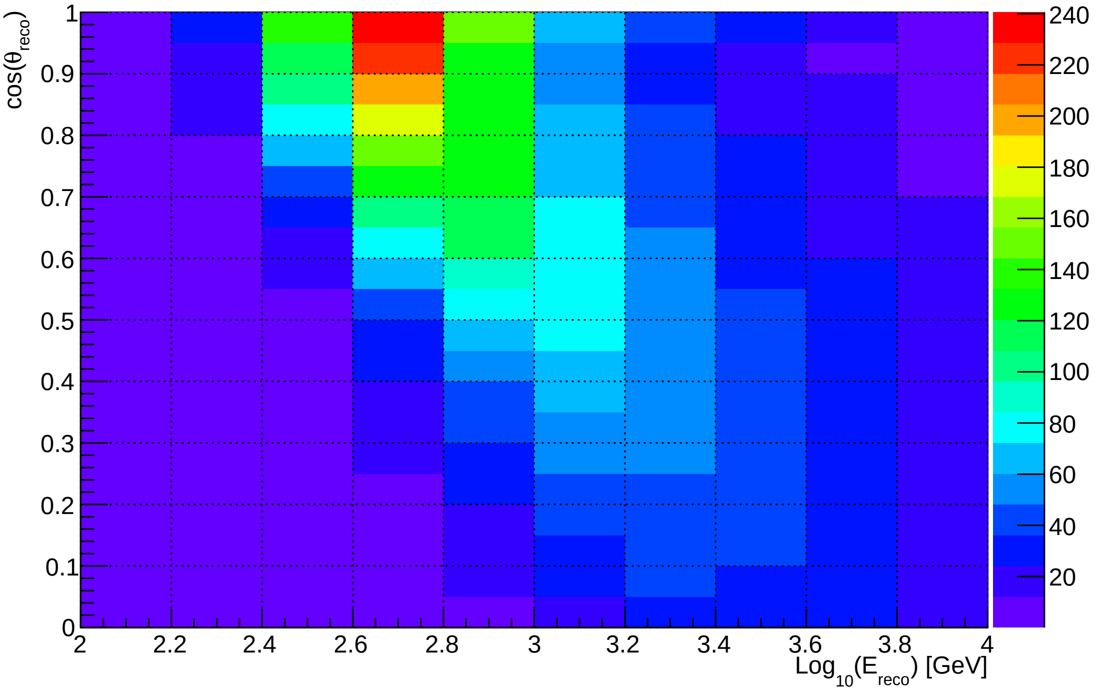

Figure 7.4: Histogram of selected MC $(\nu_\mu + \bar{\nu}_\mu)$ CC events.

Name	Test Values	Prior
N	1.0	FREE
θ_{24} [°]	0.0	FREE
Δm^2_{41} $[10^{-3}\,\mathrm{eV}^2]$	0.0	FREE
θ_{13} [°]	8.41	8.41±0.28
$\Delta\gamma$	0.00	0.00 ± 0.05
X_{sec} $[\sigma]$	0.0	0.0±1.0
$\nu/\overline{\nu}$ $[\sigma]$	0.0	0.0±1.0

Table 7.4: List of *test values* with eventual prior, for all the parameters fitted in the analysis.

Results obtained from this sensitivity study are shown in Figure 7.5, where the 90% CL and 99% CL exclusion limits in the plane of $\sin^2(2\theta_{24})$ and Δm^2_{41} are presented in comparison with the published constraints by IceCube and MINOS.

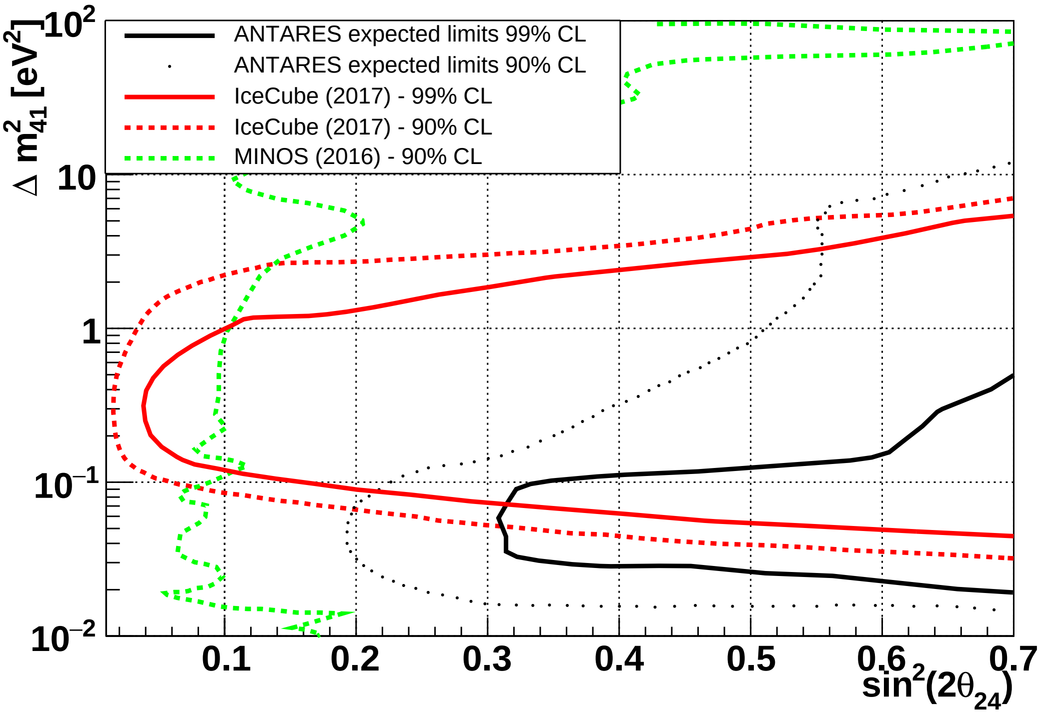

Figure 7.5: 90% CL (dashed black) and 99% CL (solid black) expected ANTARES exclusion limits, in comparison with the published 90% and 99% CL results by IceCube [69] (dashed and solid red) and the 90% CL limits by MINOS [68] (dashed green). Excluded regions are on the right-hand side of the curves.

As can be seen from the figure, the ANTARES limits extend towards lower values of Δm^2_{41} with respect to the ones presented by IceCube. The reason for this shift lays on the energy distribution of the events, which for ANTARES is peaked at lower energies in comparison to IceCube. However, MINOS already excluded the region of the parameter space to which we would be more sensitive. For this reason, this study has not been further pursued.

7.6 Conclusions

The first ANTARES constraints on the 3+1 neutrino model have been presented. Using the same data set as well as the same analysis chain as for the standard oscillation analysis, it has been demonstrated that ANTARES data can help in reducing the allowed parameter space for the existence of an additional sterile neutrino. Limits are consistent with the ones presented by other collaborations, and, in some regions, even more stringent.

A complementary study, based only on MC and without considering the background caused by misreconstructed atmospheric muons, has been presented as well. It reveals the potential for ANTARES to constrain the 3+1 model also looking at higher energy events, in which limits could be inferred also on the mass splitting Δm^2_{41}, whose effect is not dominant in the lower energy range.

Chapter 8

Conclusions and outlook

In this last Chapter the main results obtained during this thesis work are summarized and future prospects in terms of the analyses presented are given.

Ten years of ANTARES data have been analyzed and different studies have been performed as part of this thesis work.

An important part has been devoted to the determination of the ANTARES OMs photon detection efficiency through ^{40}K decays in sea water. The results of this study denotes an average decrease of only 20% in terms of photon detection efficiency, demonstrating that devices of this kind can remain operational in a hard environment, such as the one of deep sea, for a timescale of at least a decade without suffering of major degradation. These results have been published in the *European Physical Journal C* [121], and they are used as input for the most up-to-date ANTARES MC production.

With the aim of updating the official ANTARES MC chain, several tests have been done in order to choose the model which simulates the water properties at the ANTARES site with the best precision. The water model best matching the data is used as input for the most up-to-date ANTARES MC production, as well.

ANTARES has been optimized for the detection of very high energy neutrinos. However, its low energy threshold of around 20 GeV allows to study also the phenomenon of atmospheric neutrino oscillations. A first analysis, using three years of ANTARES data, had been performed in order to provide a measurement of the atmospheric neutrino oscillation parameters, showing that, even if not compatible with other experiments, results were consistent.

In this work a new analysis has been developed, using ANTARES data from 2007 to 2016 and including the treatment of new systematic sources in a detailed way. A different minimization procedure has been applied and the background of atmospheric muons has been extrapolated from data and accounted for in the analysis. Results show a good improvement with respect to the previous ANTARES analysis, and, even if they are still not competitive with the ones presented by other collaborations, they are in agreement with them.

Using the same data set and the same analysis chain, constraints on the 3+1 neutrino model have been inferred as well. This is the first ANTARES sterile neutrino analysis, and results show consistency as well as some improvements with respect to results published by other collaborations.

Both the standard oscillation and the sterile analyses have been preceded by a dedicated MC sensitivity study, in order to optimize the event selection criteria and to test the potential of these studies. A similar sensitivity study has been presented for another analysis, namely the one which looks for constraints in the 3+1 neutrino model using more energetic events. This additional study reveals some potential for ANTARES to extend the limits towards a slightly different portion of the model space with respect to the ones obtained by IceCube. However, since the MINOS Collaboration already excluded the region of maximal sensitivity for ANTARES, the analysis has not been further pursued.

All the studies presented in this thesis work could serve as starting point for the next generation of neutrino telescopes in the Mediterranean Sea, called KM3NeT [53]. KM3NeT will include two main detectors, ARCA in Sicily, devoted to the physics of high-energy astroparticles, and ORCA in France, focused on studies of atmospheric neutrinos with energies of a few GeV. They both use a configuration similar to that of ANTARES, but with 31 PMTs instead of three on each floor. ORCA, in particular, will be constituted, in its final configuration, of 115 detection lines equipped with 18 floors of 31 PMTs each. It will be much denser compared to ANTARES, which will reduce the energy threshold to a few GeV. This low energy threshold makes ORCA a very suitable detector for the study of atmospheric neutrino oscillations.

In addition, the technique employed here for determining the photon detection efficiency of ANTARES OMs using ^{40}K decays in sea-water is also used for KM3NeT. Its new configuration, with 31 PMTs in each floor, moreover, allows to record not only double coincidences, but also higher level ones, improving in such a way both the calibration and the background rejection tools.

Acknowledgements

I would like to thank you my thesis supervisor, Jürgen Brunner, who has been very patient with me during these three years, and thanks to whom I have been able to reach this goal, learning and growing a lot as a physicist.

My thank you goes to the whole CPPM/ANTARES group, in particular to Vincent, who was always kind and available for helping me.

A special thanks to Alex, who has become more like a friend than a colleague in these years; thanks for the support, for the hours spent waiting for my lost luggage at the airport, for the nice words you always had for me.

I would like to thank you the whole ANTARES and KM3NeT collaborations, for the opportunity they gave me to be part of this incredible team of people. It has been a pleasure working with them. In particular, I want to thank you Luigi, Joao, Jannik, Simon and Steffen for the fruitful discussions and the help they provided me.

But I would have never been able to reach this important goal without the support of my family. The biggest thank you goes to Andrea, my fiancé, who has never let me feel alone in these three years of long-distance relationship. Thank you for always being there for me, for the calls, for the hours you spent traveling for me, for the words of support when I thought I could not do it.

A special thank you to my parents, who made a lot of sacrifices for me, and who have never doubt that one day I would have reached this objective. Without their love and support I would not be who I am today.

Bibliography

[1] S. M. Bilenky. Neutrino. History of a unique particle. *European Physical Journal H*, 38:345–404, 2013.

[2] F. Reines and C. L. Cowan. The Neutrino. *Nature*, 178:446–449, 1956.

[3] G. Danby et al. Observation of High-Energy Neutrino Reactions and the Existence of Two Kinds of Neutrinos. *Physical Review Letters*, 9:36–44, 1962.

[4] M. L. Perl et al. Evidence for anomalous lepton production in e^+e^- annihilation. *Physical Review Letters*, 35:1489–1492, 1975.

[5] DONUT Collaboration. Observation of tau neutrino interactions. *Physics Letters B*, 504:218–224, 2001.

[6] K. Nakamura et al. Review of Particle Physics. *Journal of Physics G Nuclear Physics*, 37(7):075021, 2010.

[7] C. Yanagisawa. Looking for Cosmic Neutrino Background. *Frontiers in Physics*, 2:30, 2014.

[8] F. L. Villante. ecCNO solar neutrinos: A challenge for gigantic ultra-pure liquid scintillator detectors. *Physics Letters B*, 742:279–284, 2015.

[9] A. Mirizzi et al. Supernova neutrinos: production, oscillations and detection. *Nuovo Cimento*, 39:1–112, 2016.

[10] G. Bellini et al. Geo-neutrinos. *Progress in Particle and Nuclear Physics*, 73:1–34, 2013.

[11] G. Bellini et al. Measurement of geo-neutrinos from 1353 days of Borexino. *Physics Letters B*, 722:295–300, 2013.

[12] S. Cecchini and M. Spurio. Atmospheric muons: experimental aspects. *Geoscientific Instrumentation, Methods and Data Systems*, 1:185–196, 2012.

[13] M. Honda et al. Atmospheric neutrino flux calculation using the NRLMSISE-00 atmospheric model. *Physical Review D*, 92(2):023004, 2015.

[14] G. D. Barr et al. Uncertainties in atmospheric neutrino fluxes. *Physical Review D*, 74(9):094009, 2006.

[15] C. Patrignani et al. The Review of Particle Physics. *Chinese Physics C*, 40, 2017.

[16] VERITAS Collaboration. Observations of the Crab Nebula with the Whipple 10 m Telescope. *arXiv e-prints*, 2007. arXiv:0709.4300 [astro-ph].

[17] J. Holder et al. The first VERITAS telescope. *Astroparticle Physics*, 25:391–401, 2006.

[18] H.E.S.S. Collaboration. The H.E.S.S. Source Catalog. `https://www.mpi-hd.mpg.de/hfm/HESS/pages/home/sources/`.

[19] Magic Collaboration. Results from the MAGIC gamma-ray telescope. In *Journal of Physics Conference Series*, volume 171, 2009.

[20] Fermi LAT Collaboration. Fundamental physics in space with the Fermi Gamma-ray Space Telescope. In *Journal of Physics Conference Series*, volume 306, 2011.

[21] M. G. Aartsen et al. Evidence for High-Energy Extraterrestrial Neutrinos at the IceCube Detector. *Science*, 342:1242856, 2013.

[22] IceCube and Fermi-LAT and MAGIC and AGILE and ASAS-SN and HAWC and H. E. S. S. and INTEGRAL and Kanata and Kiso and Kapteyn and Liverpool telescope and Subaru and Swift/NuSTAR and VERITAS and VLA/17B-403 teams. Multi-messenger observations of a flaring blazar coincident with high-energy neutrino IceCube-170922A. *arXiv e-prints*, 2018. arXiv:1807.08816 [astro-ph.HE].

[23] T. Lasserre and H. W. Sobel. Reactor neutrinos. *Comptes Rendus Physique*, 6:749–757, 2005.

[24] S. E. Kopp. Accelerator neutrino beams. *Physics Reports*, 439:101–159, 2007.

[25] J. A. Formaggio and G. P. Zeller. From eV to EeV: Neutrino Cross-Sections Across Energy Scales. *arXiv e-prints*, 2013. arXiv:1305.7513v1 [hep-ex].

[26] L. Fields. Neutrino Cross Sections. *arXiv e-prints*, 2012. arXiv:1212.0060v1 [hep-ex].

[27] F. Shök. *Studies on atmospheric neutrino oscillations with the Antares neutrino telescope.* PhD thesis, Der Naturwissenschaftlichen Fakultät der Friedrich-Alexander-Universität Erlangen-Nürnberg, 2011.

[28] D. Bailey. *Monte Carlo tools and analysis methods for understanding the ANTARES experiment and predicting its sensitivity to Dark Matter.* PhD thesis, Oxford University, 2002.

[29] G. Ingelman et al. LEPTO 6.5 - A Monte Carlo generator for deep inelastic lepton-nucleon scattering. *Computer Physics Communications*, 101:108–134, 1997.

[30] D. Rein and L. M. Sehgal. Neutrino-excitation of baryon resonances and single pion production. *Annals of Physics*, 133:79–153, 1981.

[31] R. Davis. Neutrino '72. In A. Frenkel and G. Marx, editors, *Neutrino '72*, 1972.

[32] Super-Kamiokande Collaboration. SK official website. `http://www-sk.icrr.u-tokyo.ac.jp/sk/index-e.html`.

[33] SNO Collaboration. SNO official website. `https://www.sno.phy.queensu.ca/`.

[34] Y. Fukuda et al. Evidence for Oscillation of Atmospheric Neutrinos. *Physical Review Letters*, 81:1562–1567, 1998.

[35] R. L. Helmer et al. First results from the Sudbury Neutrino Observatory. *Nuclear Physics B Proceedings Supplements*, 111:122–127, 2002.

[36] S. P. Mikheev and A. I. Smirnov. Resonant amplification of neutrino oscillations in matter and solar-neutrino spectroscopy. *Nuovo Cimento C*, 9:17–26, 1986.

[37] S. Goswami. Solar Neutrino Experiments: An Overview. *arXiv e-prints*, 2003. arXiv:0303075 [hep-ph].

[38] G. Alimonti et al. The Borexino detector at the Laboratori Nazionali del Gran Sasso. *Nuclear Instruments and Methods in Physics Research A*, 2008.

[39] S. Abe et al. Precision Measurement of Neutrino Oscillation Parameters with KamLAND. *Physical Review Letters*, 100(22):221803, 2008.

[40] G. L. Foglie et al. Solar neutrino oscillations and indications of matter effects in the Sun. *Physical Review D*, 67(7):073001, 2003.

[41] J. Cao and K.-B. Luk. An overview of the Daya Bay reactor neutrino experiment. *Nuclear Physics B*, 908:62–73, 2016.

[42] C. Palomares. Double Chooz neutrino experiment. In F. Giovannelli and G. Mannocchi, editors, *Frontier Objects in Astrophysics and Particle Physics*, 2009.

[43] J. K. Ahn et al. RENO: An Experiment for Neutrino Oscillation Parameter θ_{13} Using Reactor Neutrinos at Yonggwang. *arXiv e-prints*, 2010. arXiv:1003.1391 [hep-ex].

[44] C. Zhang. Recent results from the Daya Bay experiment. In *American Institute of Physics Conference Series*, 2015.

[45] S. Parke. What is Δ m^2_{ee}? *Physical Review D*, 93(5):053008, 2016.

[46] K. Abe et al. Atmospheric neutrino oscillation analysis with external constraints in Super-Kamiokande I-IV. *Physical Review D*, 97:072001, 2018.

[47] S. M. Adrián et al. Measurement of atmospheric neutrino oscillations with the ANTARES neutrino telescope. *Physics Letters B*, 714:224–230, 2012.

[48] M. G. Aartsen et al. Measurement of Atmospheric Neutrino Oscillations at 6-56 GeV with IceCube DeepCore. *arXiv e-prints*, 2017. arXiv:1707.07081 [hep-ex].

[49] M. Sanchez. NOvA Results and Prospects, June 2018. Talk at XXVIII International Conference on Neutrino Physics and Astrophysics, 4-9 June 2018, Heidelberg, Germany.

[50] M. Wascko. T2K Status, Results, and Plans, June 2018. Talk at XXVIII International Conference on Neutrino Physics and Astrophysics, 4-9 June 2018, Heidelberg, Germany.

[51] A. Aurisano. Recent results from minos and minos+, June 2018. Talk at XXVIII International Conference on Neutrino Physics and Astrophysics, 4-9 June 2018, Heidelberg, Germany.

[52] M. G. Aartsen et al. Letter of Intent: The Precision IceCube Next Generation Upgrade (PINGU). *arXiv e-prints*, 2017. arXiv:1401.2046v2 [physics.ins-det].

[53] S. M. Adrián et al. Letter of intent for KM3NeT 2.0. *Journal of Physics G Nuclear Physics*, 43(8):084001, 2016.

[54] N. C. Hastings. The T2K Neutrino Oscillation Experiment and Possible Future Projects. *arXiv e-prints*, 2009. arXiv:0905.1211 [hep-ex].

[55] F. Capozzi et al. Neutrino masses and mixings: Status of known and unknown 3ν parameters. *Nuclear Physics B*, 908:218–234, 2016.

[56] P. F. de Salas et al. Status of neutrino oscillations 2018: 3σ hint for normal mass ordering and improved CP sensitivity. *Physics Letters B*, 782:633–640, 2018.

[57] M. C. Gonzalez-Garcia. Global analyses of neutrino oscillation experiments. *Nuclear Physics B*, 908:199–217, 2016.

[58] M. Cribier. Reactors antineutrino anomalies and searches for sterile neutrinos. In *Journal of Physics Conference Series*, 2015.

[59] T. A. Mueller et al. Improved predictions of reactor antineutrino spectra. *Physical Review C*, 83(5):054615, 2011.

[60] F. P. An et al. Evolution of Reactor Antineutrino Flux and Spectrum at Daya Bay. *Physical Review Letters*, 118(25):251801, 2017.

[61] C. Giunti et al. Reactor fuel fraction information on the antineutrino anomaly. *Journal of High Energy Physics*, 10:143, 2017.

[62] Seon-Hee Seo for the RENO Collaboration. New Results from RENO and The 5 MeV Excess. *arXiv e-prints*, 2014. arXiv:1410.7987 [hep-ex].

[63] Daya Bay Collaboration. Improved measurement of the reactor antineutrino flux and spectrum at Daya Bay. *Chinese Physics C*, 41(1):013002, 2017.

[64] Double-Chooz Collaboration. Latest results from Double Chooz. In *Proceedings of the European Physical Society Conference on High Energy Physics*, July 2017.

[65] M. Dentler et al. Updated global analysis of neutrino oscillations in the presence of eV-scale sterile neutrinos. *arXiv e-prints*, 2018. arXiv:1803.10661 [hep-ph].

[66] M. G. Aartsen et al. Search for sterile neutrino mixing using three years of IceCube DeepCore data. *Physical Review D*, 95(11):112002, 2017.

[67] The Super-Kamiokande Collaboration. Limits on Sterile Neutrino Mixing using Atmospheric Neutrinos in Super-Kamiokande. *Physical Review D*, 91, 2015.

[68] P. Adamson et al. Limits on Active to Sterile Neutrino Oscillations from Disappearance Searches in the MINOS, Daya Bay, and Bugey-3 Experiments. *Physical Review Letters*, 117(15):151801, 2016.

[69] M. G. Aartsen et al. Searches for Sterile Neutrinos with the IceCube Detector. *Physical Review Letters*, 117(7):071801, 2016.

[70] A. Aguilar-Arevalo et al. Evidence for neutrino oscillations from the observation of ν_e appearance in a ν_μ beam. *Physical Review D*, 64(11):112007, 2001.

[71] MiniBooNE Collaboration. Observation of a Significant Excess of Electron-Like Events in the MiniBooNE Short-Baseline Neutrino Experiment. *arXiv e-prints*, May 2018. arXiv:1805.12028 [hep-ex].

[72] W. Winter. Neutrino mass hierarchy: Theory and phenomenology. In *American Institute of Physics Conference Series*, volume 1666 of *American Institute of Physics Conference Series*, 2015.

[73] R. B. Patterson. The NOvA experiment: status and outlook. *Nuclear Physics B Proceedings Supplements*, 235:151–157, 2013.

[74] T2K Collaboration. Measurements of neutrino oscillation in appearance and disappearance channels by the T2K experiment with 6.6×10^{20} protons on target. *Physical Review D*, 91, 2015.

[75] E. Kemp. The Deep Underground Neutrino Experiment: The precision era of neutrino physics. *Astronomische Nachrichten*, 338:993–999, 2017.

[76] Eligio Lisi. Opening talk, June 2018. Talk at XXVIII International Conference on Neutrino Physics and Astrophysics, 4-9 June 2018, Heidelberg, Germany.

[77] S. Bourret and L. Quinn. Sensitivity of ORCA to the neutrino mass ordering and oscillation parameters, June 2018. Poster at XXVIII International Conference on Neutrino Physics and Astrophysics, 4-9 June 2018, Heidelberg, Germany.

[78] P. I. Krastev and S. T. Pontcov. Resonance amplification and T-violation effects in three-neutrino oscillations in the earth. *Physics Letters B*, 205:84–92, 1988.

[79] LBNE Collaboration. The Long-Baseline Neutrino Experiment: Exploring Fundamental Symmetries of the Universe. *arXiv e-prints*, 2013. arXiv:1307.7335 [hep-ex].

[80] K. Abe et al. Measurement of neutrino and antineutrino oscillations by the T2K experiment including a new additional sample of ν_e interactions at the far detector. *Physical Review D*, 96(9):092006, 2017.

[81] P. Ballett et al. Sensitivities and synergies of DUNE and T2HK. *Physical Review D*, 96(3):033003, 2017.

[82] D. Zaborov. The KM3NeT Neutrino Telescope and the potential of a neutrino beam from Russia to the Mediterranean Sea. *arXiv e-prints*, 2018. arXiv:1803.08017 [hep-ex].

[83] A. Garfagnini. Neutrinoless double beta decay experiments. In *International Journal of Modern Physics Conference Series*, 2014.

[84] M. Auger et al. The EXO-200 detector, part I: detector design and construction. *Journal of Instrumentation*, 7:5010, 2012.

[85] S. Abe et al. Production of radioactive isotopes through cosmic muon spallation in KamLAND. *Physical Review C*, 81(2):025807, 2010.

[86] GERDA Collaboration. Measurement of the half-life of the two-neutrino double beta decay of Ge-76 with the Gerda experiment. *arXiv e-prints*, 2012. arXiv:1212.3210 [nucl-ex].

[87] The Majorana Collaboration. White Paper on the Majorana Zero-Neutrino Double-Beta Decay Experiment. *arXiv e-prints*, 2003. arXiv:0311013 [nucl-ex].

[88] J. W. Beeman et al. CUORE: The Cryogenic Underground Observatory for Rare Events. In E. Norman et al., editor, *Nuclear Physics in the 21st Century*, 2002.

[89] A. J. Zsigmond. New results from GERDA Phase II, June 2018. Talk at XXVIII International Conference on Neutrino Physics and Astrophysics, 4-9 June 2018, Heidelberg, Germany.

[90] M. Steidl. Experiments for the absolute neutrino mass measurement. *arXiv e-prints*, 2009. arXiv:0906.0454 [nucl-ex].

[91] T. J. Loredo and D. Q. Lamb. Neutrinos from SN 1987A - Implications for cooling of the nascent neutron star and the mass of the electron antineutrino. *Annals of the New York Academy of Sciences*, 571:601–630, 1989.

[92] D. E. Groom. Searches for massive neutrinos. *European Physical Journal C*, 15:358–359, 2000.

[93] ALEPH Collaboration. An upper limit on the τ neutrino mass from three- and five-prong tau decays. *European Physical Journal C*, 2:395–406, 1998.

[94] KATRIN collaboration. KATRIN: A next generation tritium beta decay experiment with sub-eV sensitivity for the electron neutrino mass. *arXiv High Energy Physics - Experiment e-prints*, 2001.

[95] D. Parno. KATRIN: Toward a High-Precision Neutrino-Mass Determination with Tritium, June 2018. Talk at XXVIII International Conference on Neutrino Physics and Astrophysics, 4-9 June 2018, Heidelberg, Germany.

[96] M. Tegmark et al. Tegmark. Cosmological constraints from the SDSS luminous red galaxies. *Physical Review D*, 74(12):123507, 2006.

[97] J. V. Jelley. Cerenkov radiation and its applications. *British Journal of Applied Physics*, 1967.

[98] Unknown. Introduction to High Energy Astrophysics: Hard X-Ray (10 to 500 keV) Detectors. `http://astronomy.nmsu.edu/tharriso/ast536/ast536week9.html`.

[99] M. Ageron et al. ANTARES: The first undersea neutrino telescope. *Nuclear Instruments and Methods in Physics Research A*, 656:11–38, 2011.

[100] Hammamatsu Photonics. Hammamatsu Photonics official website. `http://www.hamamatsu.com`.

[101] J. A. Aguilar et al. Time calibration of the ANTARES neutrino telescope. *Astroparticle Physics*, 34:539–549, 2011.

[102] B. Bakker. Trigger studies for the Antares and KM3NeT neutrino telescopes. Master's thesis, University of Amsterdam, 2011.

[103] A. Albert et al. New constraints on all flavor Galactic diffuse neutrino emission with the ANTARES telescope. *Physical Review D*, 96(6):062001, 2017.

[104] A. Albert et al. First all-flavor neutrino pointlike source search with the ANTARES neutrino telescope. *Physical Review D*, 96(8):082001, 2017.

[105] L. A. Fusco. *Search for a diffuse neutrino emission in the Southern Sky with the ANTARES telescope.* PhD thesis, Università di Bologna, 2016.

[106] A. Mathieu. *Multi-wavelength follow-up of ANTARES neutrino alerts.* PhD thesis, Aix Marseille Université, CPPM, 2015.

[107] ANTARES Collaboration. The ANTARES Collaboration: Contributions to ICRC 2017 Part II: The multi-messenger program. *arXiv e-print*, 2017. arXiv:1711.01486v1 [astro-ph.HE].

[108] S. M. Adrián et al. Limits on Dark Matter Annihilation in the Sun using the ANTARES Neutrino Telescope. *Physics Letters B*, 759:69–74, 2016.

[109] A. Albert et al. Search for Dark Matter Annihilation in the Earth using the ANTARES Neutrino Telescope. *Physics of the Dark Universe*, 16:41–48, 2017.

[110] A. Albert et al. Search for relativistic magnetic monopoles with five years of the ANTARES detector data. *Journal of High Energy Physics*, 7:54, 2017.

[111] ANTARES Collaboration. ANTARES official webpage. `http::/antares.in2p3.fr`.

[112] J. A. Aguilar et al. Measurement of the atmospheric muon flux with a 4 GeV threshold in the ANTARES neutrino telescope. *Astroparticle Physics*, 33:86–90, 2010.

[113] J. A. Aguilar et al. Transmission of light in deep sea water at the site of the ANTARES neutrino telescope. *Astroparticle Physics*, 23:131–155, 2005.

[114] S. Kim et al. PubChem Substance and Compound databases. *Nucleic Acids Research*, 44:1202–13, 2016.

[115] G. Audi et al. The NUBASE evaluation of nuclear and decay properties. *Nuclear Physics A*, 729:3–128, 2003.

[116] J. F. Anthoni. The chemical composition of seawater. `http://www.seafriends.org.nz/oceano/seawater.htm`.

[117] J. R. De Laeter et al. Atomic Weights of the Elements: Review 2000 (IUPAC Technical Report). *Pure Applied Chemistry*, 75:683–800, 2003.

[118] C. Tamburini et al. Deep-Sea Bioluminescence Blooms after Dense Water Formation at the Ocean Surface. *PLoS ONE 8(7)*, 2013.

[119] M. Ageron et al. The ANTARES optical beacon system. *Nuclear Instruments and Methods in Physics Research A*, 578:498–509, 2007.

[120] S. Adrián-Martínez et al. Time calibration with atmospheric muon tracks in the ANTARES neutrino telescope. *Astroparticle Physics*, 78:43–51, 2016.

[121] A. Alebert et al. Long-term monitoring of the ANTARES optical module efficiencies using ^{40}K decays in sea water. *European Physical Journal C*, 78, 2018.

[122] G. Carminati et al. Atmospheric MUons from PArametric formulas: a fast GEnerator for neutrino telescopes (MUPAGE). *Computer Physics Communications*, 179:915–923, 2008.

[123] Geant Collaboration. Geant official website. `http://geant4.web.cern.ch/geant4/`.

[124] A. Capone et al. Measurements of light transmission in deep sea with the AC9 trasmissometer. *Nuclear Instruments and Methods in Physics Research A*, 487:423–434, 2002.

[125] R. C. Smith and K. S. Baker. Optical properties of the clearest natural waters (200-800 nm). *Applied Optics*, 20:177–184, 1981.

[126] R. Brun and F. Rademakers. ROOT - An object oriented data analysis framework. *Nuclear Instruments and Methods in Physics Research A*, 389:81–86, 1997.

[127] N. D. Gagunashvili. Comparison of weighted and unweighted histograms. *arXiv e-prints*, 2006. arXiv:0605123 [physics.data-an].

[128] J. A. Aguilar et al. A fast algorithm for muon track reconstruction and its application to the ANTARES neutrino telescope. *Astroparticle Physics*, 34:652–662, 2011.

[129] A. J. Heijboer. *Track Reconstruction and Point Source Searches with ANTARES*. PhD thesis, Universiteit van Amsterdam, 2004.

[130] E. Visser. *Neutrinos from the Milky Way*. PhD thesis, Universiteit Leiden, 2015.

[131] H. M. Motz. *Dark Matter Search with ANTARES*. PhD thesis, Friedrich-Alexander-Universität Erlangen-Nürnberg, 2011.

[132] T. L. Astraatmadja. On the detection of TeV γ-rays from GRB with km^3 neutrino telescopes - I. Muon event rate from single GRBs. *Monthly Notices of the Royal Astronomical Society*, 418:1774–1786, 2011.

[133] The ANTARES Collaboration. The Antares Collaboration : Contributions to the 33st International Cosmic Ray Conference (ICRC 2013, Rio de Janeiro). *arXiv e-prints*, 2013. arXiv:1312.4308 [astro-ph.HE].

[134] J. Coelho. OscProb. `https://github.com/joaoabcoelho/OscProb/`.

[135] A. M. Dziewonski and D. L. Anderson. Preliminary reference Earth model. *Physics of the Earth and Planetary Interiors*, 25:297–356, 1981.

[136] C. Distefano. gSeaGen: A GENIE-based code for neutrino telescopes. In *European Physical Journal Web of Conferences*, 2016.

[137] C. Andreopoulos et al. The GENIE Neutrino Monte Carlo Generator: Physics and User Manual. *arXiv e-prints*, 2015. arXiv:1510.05494 [hep-ph].

[138] S. K. Agarwalla et al. Signatures of a Light Sterile Neutrino in T2HK. *arXiv e-prints*, 2018. arXiv:1801.04855v2 [hep-ph].